SDC-91-135

SDC-91-135

Superconducting Super Collider Laboratory

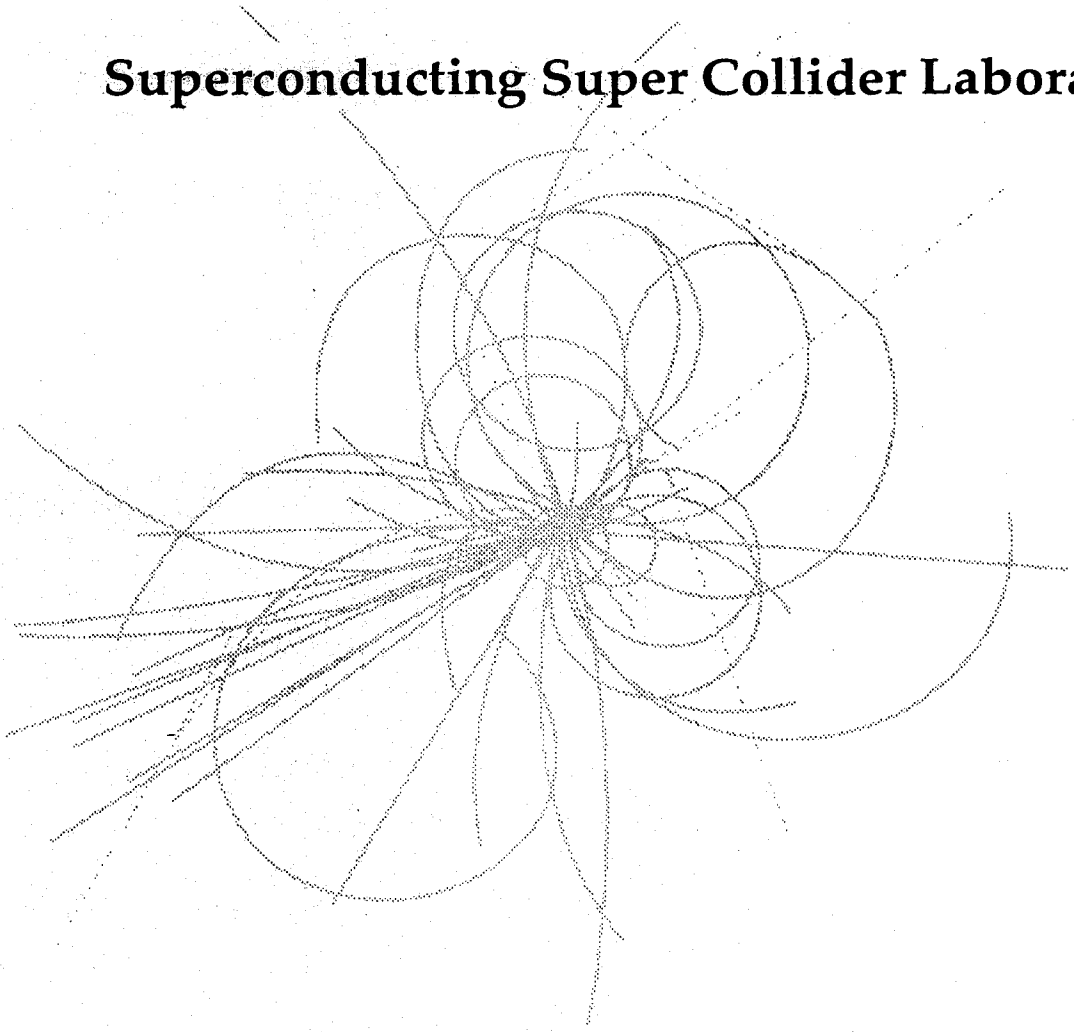

SDC Muon Detector Design
Barrel and Intermediate Chambers
Round Tube Option

University of Washington/SSC Design

January 1992

SDC-91-135

SDC Muon Detector Design
Barrel and Intermediate Chambers
Round Tube Option

K. Bramble[2], U. Bratzler[1], D. Cox[2], C. Daly[3], R. Davisson[1], W. Dougherty[1], P. Draper[4], T. Fukui[2], J. Hersch[1], Z. Jin[1], H. Guldenmann[1], J. Jeffers[3], H. Lubatti[1,2], T. Pal[2], K. Paulson[1], K. Pennnington[2], L. Sawyer[4], J. Thunborg[2], A. White[4], T. Zhao[1]

Physics Research Division
Superconducting Super Collider Laboratory*
2550 Beckleymeade Avenue
Dallas, Texas 75237

January 1992

[1] Department of Physics, University of Washington, Seattle, WA 98195 Washington U., Seattle
[2] Superconducting Super Collider Laboratory, Dallas, TX 75237 SSCL
[3] Department of Mechanical Engineering, University of Washington, Seattle, WA 98195 Washington U. Seattle
[4] Department of Physics, University of Texas at Arlington, TX Texas U., Arlington

* Operated by the Universities Reasearch Association, Inc., for the U.S. Department of Energy under Contract No. DE-AC35-89R40486

CONTENTS

FIGURES vi
TABLES ix
PREFACE xi
1.0. INTRODUCTION 1-1
1.1 Basic Approach 1-1
1.2 Design Philosophy 1-2
1.3 Drift Tubes 1-2
2.0 DESIGN CONCEPT 2-1
2.1 Module Assembly 2-3
2.2 Module Supports 2-3
3.0 STRUCTURAL ANALYSIS OF DETECTOR MODULES 3-1
3.1 Determination of Equivalent Shell Properties 3-1
3.2 FEA Shell Model of a Module 3-2
3.3 Shear Stresses in the Adhesive Joints 3-3
3.4 Discussion 3-4
4.0 DRIFT CELL DESIGNS 4-1
4.1 Simple Drift Tube 4-1
4.1.1 Tube Size and Gas Mixtures 4-1
4.1.2 Wire Sag and Tube Deformation 4-4
4.1.3 Operation Mode 4-4
4.1.4 Double Track Resolution 4-4
4.2 Cylindrical Tube With Simple Field Shaping 4-5
4.2.1 Cell Design 4-5
4.2.2 Gas Mixture and Operating Conditions 4-6
4.2.3 Double Track Resolution 4-6
REFERENCES 4-7
5.0 TRIGGER 5-1
5.1 Level 1 Muon Trigger Simulations 5-1
5.1.1 Basic Trigger Arrangement 5-1
5.1.2 Toroid Thickness 5-1
5.1.3 Interaction Region Size 5-2
5.1.4 θ Dependence 5-2
5.1.5 Trigger Electronics Time Resolution 5-2
5.1.6 Non-linear x-t Correlation 5-3

5.2 Trigger Rate 5-3
5.3 Basic Requirements for the Level 1 Trigger Electronics 5-3
5.3.1 Time Required for Level 1 Trigger Generation 5-3
5.3.2 ΔT Coverage 5-4
5.3.3 Time Resolution 5-4
5.3.4 Programmability 5-4
5.4 Circuit Designs 5-4
5.4.1 Circuit 1 5-4
5.4.2 Circuit 2 5-4
5.4.3 Implementing into XILINX FPGA 5-4
5.4.4 Trigger System Design 5-5
5.4.5 Future Plans 5-5
6.0 CELL CONSTRUCTION 6-1
6.1 Aluminum Extrusions 6-1
6.2 Field Shaping Electrodes 6-1
6.3 End Caps 6-1
6.3.1 End Cap Shells 6-1
6.3.2 Injection Molded Supports 6-2
6.3.3 Contact Springs 6-2
6.3.4 Electrical Components 6-2
6.3.5 CERN Feed Throughs 6-2
6.4 Anode Wire 6-2
6.5 Gas Fitting 6-3
7.0 ALIGNMENT 7-1
7.1 General 7-1
7.2 Wire to Module Alignment 7-1
7.3 Module Alignment 7-2
7.4 The Optical Straight Edge 7-2
7.5 Creating a Space Frame 7-3
7.6 Verification of the NC Milled End Plates 7-3
8.0 MANUFACTURING PLAN 8-1
8.1 Manufacturing Approach/Philosophy 8-1
8.2 Manufacturing Description 8-1
8.2.1 Circuit Boards 8-1
8.2.2 Injection Molded Plastic Supports 8-1
8.2.3 End Cap Shells 8-2

8.2.4 End Cap Assembly 8-2
8.2.5 Electrode Extrusions 8-2
8.2.6 Drift Cell Tubes 8-2
8.2.7 End Plates 8-2
8.2.8 Rails 8-3
8.2.9 Outer Support Plates 8-3
8.2.10 Top and Bottom Panels 8-3
8.2.11 Spacer Sheets 8-3
8.2.12 Drift Tube Assembly 8-3
8.2.13 End Plate Assembly 8-3
8.2.14 Module Assembly 8-4
9.0 PROTOTYPE MODULES 9-1
10.0 BEAM AND COSMIC RAY TEST 10-1
10.1 Fermilab Beam Test 10-1
10.2 Cosmic Ray Test With Short Cells 10-1
10.2.1 Tube Setup 10-1
10.2.2 DAQ 10-1
10.3 Cosmic Ray Tests of Round Tube Design 10-2
ACKNOWLEDGEMENTS 11-1

FIGURES

1.1 Cross section of two adjacent modules 1-3
1.2 SDC detector layout (quadrant view) 1-4
2.1 Projective geometry of BW1 θ tubes 2-4
2.2 Overall view of muon modules showing projective tracks to theta and stereo layers 2-5
2.3 BW1—Showing field shaping electrodes with projective tracks 2-6
2.4 BW1—Projective tracks at module junction 2-7
2.5 BW1—Projective tracks at extreme end of module 2-8
2.6 Module layout 2-9
2.7 Module layers cut in plane perpendicular to z direction 2-11
2.8 IW2—Theta tubes only 2-12
2.9 IW3 module (showing θ, ϕ and stereo tubes) 2-13
2.10 Space between tube end plates and outer plates 2-14
2.11 Internal structure of a typical 4-layer module 2-15
2.12 Cross section of module edge showing the tube end plate, top and bottom rails and outer plate. For this BW3 module, the outer plate continues down to the BW2 module to form a BW2/BW3 tower. 2-16
2.13 Tube end plate. This plate has precision machined locating holes for the drift tube end caps. Clearance holes for gas and electrical connections not shown for clarity 2-17
2.14 Tube end plate. This plate has precision machined dowel holes for the drift tube end caps. Clearance holes for gas and electrical connections not shown for clarity 2-18
2.15 Detail of tube location in end plate 2-19
2.16 Cut away locating hole allows insertion of tube end cap boss at an angle while still providing precise location 2-21
2.17 Assembly of bottom rail to vertical outer and tube end plates 2-22
2.18 Assembly of bottom rail to sloping outer and tube end plates 2-23
2.19 Outer plate connects BW2 and BW3 modules to form a tower 2-24
2.20 BW2/BW3 tower assembly 2-25
2.21 Tube end plate and bottom rail are supported by an assembly jig on the assembly pad while the tubes and plates are installed 2-27
2.22 BW1 mounting structure 2-28
2.23 Lee controls roller bearing 2-29
2.24 BW1 rail mounting 2-30
2.25 3 point kinematic support for BW2/BW3 units 2-31
3.1 Cross-section of a 4-layer prototype. All tubes are 1.59 mm wall thickness and 7.26 mm outside diameter. The top and bottom plates are 6.35 mm thick and the intermediate plates are 1.59 mm thick 3-5
3.2 Finite element analysis of 8-layer beam model 3-6
3.3 Close up of beam model showing elements in tubes, plates and the adhesive joints between the tubes and between the tubes and plates 3-7
3.4 ANSYS model of the 10-layer BW3 structure 3-8

3.5 ANSYS model of 10-layer BW3 structure 3-9
3.6 Finite element model of one quadrant of a BW1 module. The tube and plate assembly is modeled by an equivalent orthotropic shell. 3-10
3.7 Close up of edge of FEA model of BW1 module showing modelling of the peripheral structure elements 3-11
3.8 Deflection results for the BW1 module. The support is 20% of the way along the long edge of the module 3-12
3.9 Deflection results for the BW2/BW3 assembly supported at four points at 20% points on the long edges 3-13
3.10 Deflection results for BW2/BW3 assembly with a web across midpoint 3-14
3.11 Test specimen in tensile testing machine 3-15
4.1 High voltage and signal connections 4-9
4.2 A reconstructed muon track 4-9
4.3 Electric fields as functions of distances to the tube center. Proportional mode operation using gas mixtures with 90% of argon and 10% of quenching gas is assumed ... 4-10
4.4 Electron diffusion for two gas mixtures 4-11
4.5 Electron drift velocity vs electric field 4-12
4.6 x-t correlation plots 4-13
4.7 Trigger efficiency vs transverse momentum computed by assuming a nonlinear x-t correlation given in Figure 4.6b 4-14
4.8 Trigger efficiency vs transverse momentum computed by assuming a linear x-t correlation 4-14
4.9 Temperature dependence of drift velocity for P10 gas 4-15
4.10 Cross-section of a drift tube 4-16
4.11 High voltage and signal connections. Field shaping electrodes and anode are both at +5 kV 4-16
4.12 Drift field lines and equipotential contours. Anode and electrodes are both at +5 kV 4-17
4.13 Drift field uniformity in the drift cell. Anode and electrodes are both at +5 kV 4-18
4.14 x-t correlation curve for Ar-CO_2 (90:10%). The maximum drift time is 780 ns 4-18
4.15 x-t correlation curve for Ar-CF_4-CH_4 (80:10:10.%) The linearity of this curve is very good except for the region of r<0.5 cm. The maximum drift time is only 360 ns 4-19
4.16 x-t correlation curve for Ar-CF_4-CO_2 (90:8:2.%) The linearity of this curve is very good except for the region of r<0.5 cm. The maximum drift time is only 460 ns 4-20
5.1 Trigger efficiency vs P_t for three toroid thickness 5-7
5.2 Different interaction region sizes and a 1.5 m thick toroid 5-7
5.3 Different interaction region sizes and a 1.0 m thick toroid 5-8
5.4 Comparison between a constant 3 mm cut and a 3 mm/$\sin^2\theta$ cut 5-8
5.5 Three different cuts for round tubes 5-9
5.6 ±8 ns error of trigger electronics start and stop time makes no difference 5-9
5.7 Trigger efficiency vs P_t assuming a non-linear x-t correlation 5-10
5.8 Trigger efficiency vs P_t assuming a linear x-t correlation 5-10
5.9 Muon rate calculated by Sakai 5-11
5.10 Block diagram of trigger circuits 5-12

5.11 Logic diagram of circuit 1 5-12
5.12 Logic diagram of circuit 2 5-13
5.13 Logic diagram of the CAMAC trigger module 5-13
6.1 Field shaping electrode option extruded tube 6-5
6.2 Noryl/Aluminum coextrusions 6-7
6.3 Drift cell, boss end exploded view 6-9
6.4 Photograph of boss end end cap 6-11
6.5 Drift cell, flat end exploded view 6-13
6.6 View of flat end of an assembled tube 6-15
6.7 Boss end end cap shell 6-17
6.8a Drift cell installation 6-19
6.8b Boss end installation 6-21
6.8c Flat end installation 6-22
6.9 Flat end end cap shell 6-23
6.10 Flat end injection molding 6-24
6.11 Boss end injection molding 6-25
6.12 Copper beryllium springs 6-26
6.13 G-10 circuit cards 6-27
6.14 CERN feedthrough 6-28
6.15 Shunt connector 6-29
6.16 Gas fitting 6-30
7.1 Photographs showing the BROWN & SHARPE coordinate measuring machine used to determine the location of the holes and the hole diameter on the end plates 7-5
8.1 Manufacturing flow diagram 8-5
9.1 Corner cross section of prototype module section 9-2
9.2 Prototype module end plate 9-3
9.3 End plate details with a tube inserted 9-5
9.3 (Continued) 9-7
10.1 Schematic diagram of the cosmic ray test stand to be used at the SSCL, showing the details of the trigger counters, iron absorber and the position of the tubes for testing 10-3

TABLES

2.1 LAYER CONFIGURATION AND CHANNEL COUNT 2-1
3.1 BW1 AND BW2/3 MODULE DEFLECTIONS 3-4
4.1 DESIGN PARAMETERS – NO FIELD SHAPING 4-1
4.2 MAXIMUM DRIFT FOR DIFFERENT GAS MIXTURES 4-3
4.3 DESIGN PARAMETERS – DRIFT TUBE WITH FIELD SHAPING 4-5
5.1 INTEGRATED TRIGGER RATE FOR DIFFERENT P_T THRESHOLD 5-3

PREFACE

This volume presents a design for the SDC muon detector, based on 75 mm round aluminum drift tubes. It emphasizes the precision location of the anode wire, which is supported only at the tube ends, by CNC machined tube end-caps and locating plates. The innovative but mechanically sound concept is that it makes use of the tubes as structural elements. Electrical isolation is provided by placing the passive electrical components in the end cap. The tube and end cap form a continuous conducting skin. The wire sag is adjusted to be approximately 1.3 mm which is a stable configuration.

The simple 75 mm round tubes with no field shaping will use P10 or Ar-CO_2-CH_4 (90-5-5%) which results in a maximum drift time of approximately 1 μs. With a simple electrode, field shaping can easily be accomplished in a configuration where anode and field shaping voltage are the same (approximately 5 kV). Using Ar-CO_2 (90-10%) results in a maximum drift time of approximately 700 ns. Drift cells with electrical fields similar to those obtained in our field shaping option have been operated for many years and are known to have good position resolution.

1.0 INTRODUCTION

The purpose of the central region muon system, outside the calorimeter, is to identify muon trajectories, to link those trajectories back to tracks in the central tracker, and additionally to form a level-one trigger based on a muon p_t threshold. For $p_t > 500$ Gev/c the precision of the central tracker deteriorates and the outer system enhances the measurements. The drift cell array is optimized to meet these requirements. Key aspects are orienting the drift direction in each cell to be normal to the path of a high momentum muon, and arranging the cells in a projective geometry. Orienting the drift direction will be achieved automatically if simple tubes with circular cross section are used, or by orienting the tubes if field-shaping is employed. The use of a projective geometry regularizes and simplifies the triggers electronics and improves the accuracy of the measurements.

1.1 Basic Approach

The basic approach in this design is to:

1. separate the fabrication of the drift cells from that of the modules;
2. to make use of the drift tubes as structural elements of the modules; and
3. to establish the alignment and orientation of the drift cells within a module by the drift tube end caps and the module end plates.

The drift cells are aluminum drift tubes with circular cross section. Each of the cells of a module is a complete and independent, fully functional drift tube with all of the necessary passive interface components built into the end caps. The drift tubes are to be made and tested at various institutions and then shipped to the SSC Lab for assembly into modules.

Field shaping electrodes are easily incorporated as discussed in Section 4. In round tubes without field shaping electrodes the drift direction is optimized automatically. If shaping electrodes are used the proper orientation of each tube is imposed during the assembly of the module by mechanical constraints (pins) which are built into the endcap support structure.

The use of round tubes in this design avoids the need for midspan supports for the anode and so also avoids the complications which such supports incur. It also allows the drift direction to be optimized for each individual tube location (necessary for the field shaping option) without affecting in any way the external configuration of the body of the tube. The homogeneity of the exteriors of the tubes makes it practical to bond all of the parts of the module together. The tubes then become the structural elements of the module. This makes the module rigid without the added weight of stiffening members (see Section 3).

The largest modules are envisaged to be approximately 9 meters by 9 meters and to contain the necessary mixture of θ, ϕ, and stereo views. The cross-sectional view of the corners of two adjacent modules which contain four θ, two ϕ, and 2 stereo tubes is shown in Figure 1.1 as an illustration. This design is based on the 11-25-91 SDC detector dimensions (Figure 1.2) with the tube arrangement agreed to at the November 1991 SDC meeting: BW1 – 4 θ, 4 ϕ; BW2 and IW2 – 4 θ; BW3 and IW3 4 θ, 4 ϕ, 2 stereo. The gas manifold and gas connections as well as any electrical leads are channeled in the space between the locating end plate and protective cover. The anode wire is fixed by the end cap of the tube and located by the CNC milled endplates. See Section 2 for details. Finite element analysis shows that the eight layer BW1 module supported at four points will deflect no more than 0.46 mm when supported at four points (see Section 3 for details).

1.2 Design Philosophy

The design separates the construction of the drift cells from the module construction so the cells can be fabricated at university and national laboratories, where there is considerable accumulated experience in drift tube construction and operation. The mounting of the individual cells into the modules will take place at the SSCL or nearby. This allows for quality control and assurance of the alignment of the modules and location of each anode with respect to reference points on the module.

The precision inherent in this design is determined by the accuracy of a CNC mill and our ability to maintain the alignment of the modules. The position of the locating holes for one wire is related to the corresponding holes for neighboring wires and to nearby survey holes through common construction on a numerical mill. The modules are designed to be supported at four points with minimum deflection under their own weight, but yet sufficiently compliant to accomodate distortions in the toroid on which they are mounted. Our overall precision is determined by the accuracy of a CNC mill which is in the 12 μm range. This includes the relation of the feed through hole in the end cap to reference surfaces on the end caps and the relation of these to the mating surfaces in the end plates as well as the relation of these to local survey targets in the endplates. Thus our alignment will exceed the intrinsic measurement accuracy from the drift time measurements (150–200 μm), as it should.

1.3 Drift Tubes

We have designed and built two prototype module sections of round drift tubes. One contains drift tubes with no field shaping and the other contains tubes with field shaping (see Section 4 for details). The voltage on the field shaping electrodes is the same as the voltage on the anode (approximately 5 kV). For the field shaping cells we propose to use Ar-CO_2 (90-10%) while for the non- field shaping cells we will use either P-10 or Ar-CO_2-CH_4(90-5-5%).

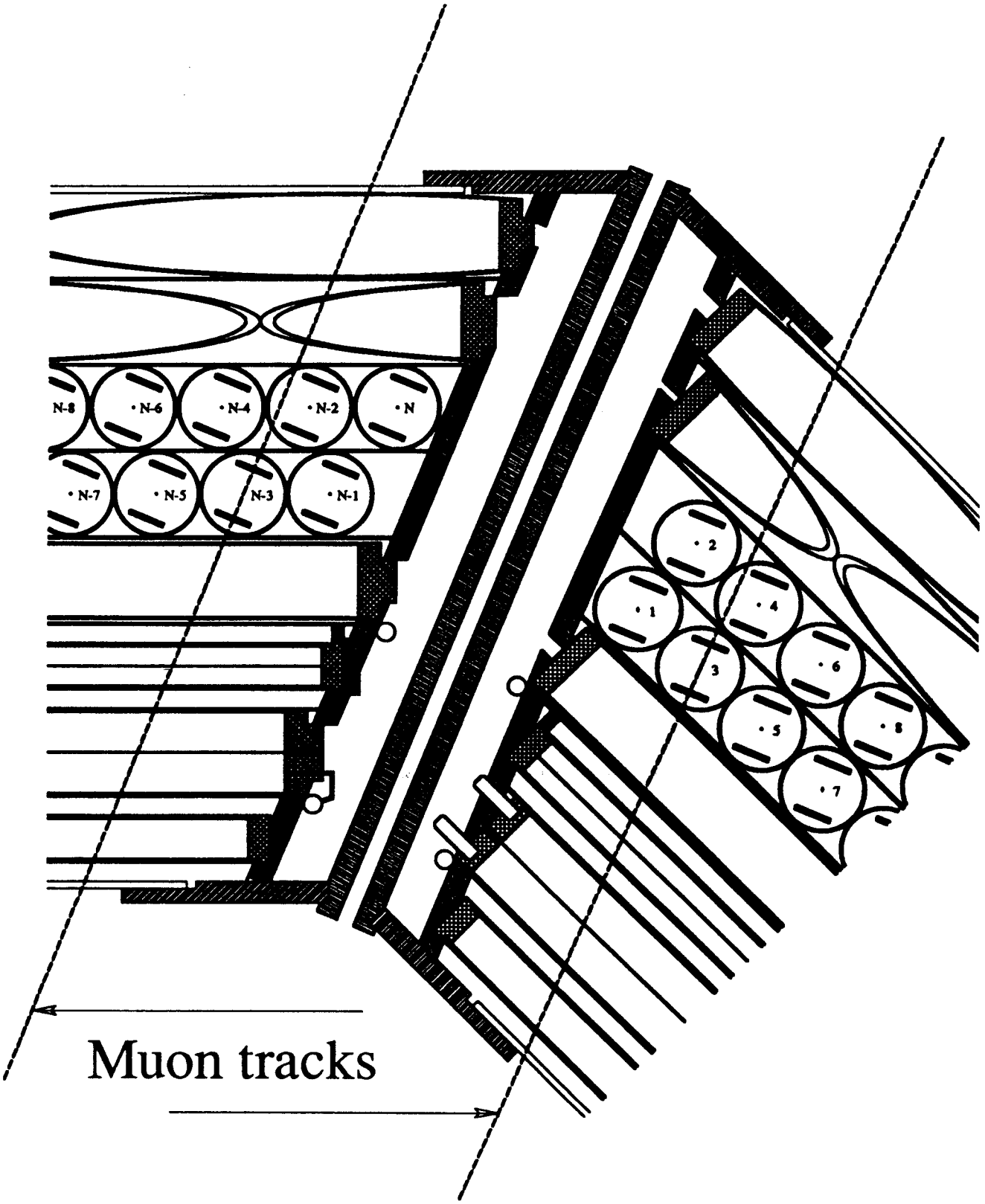

Figure 1.1. Cross section of two adjacent modules.

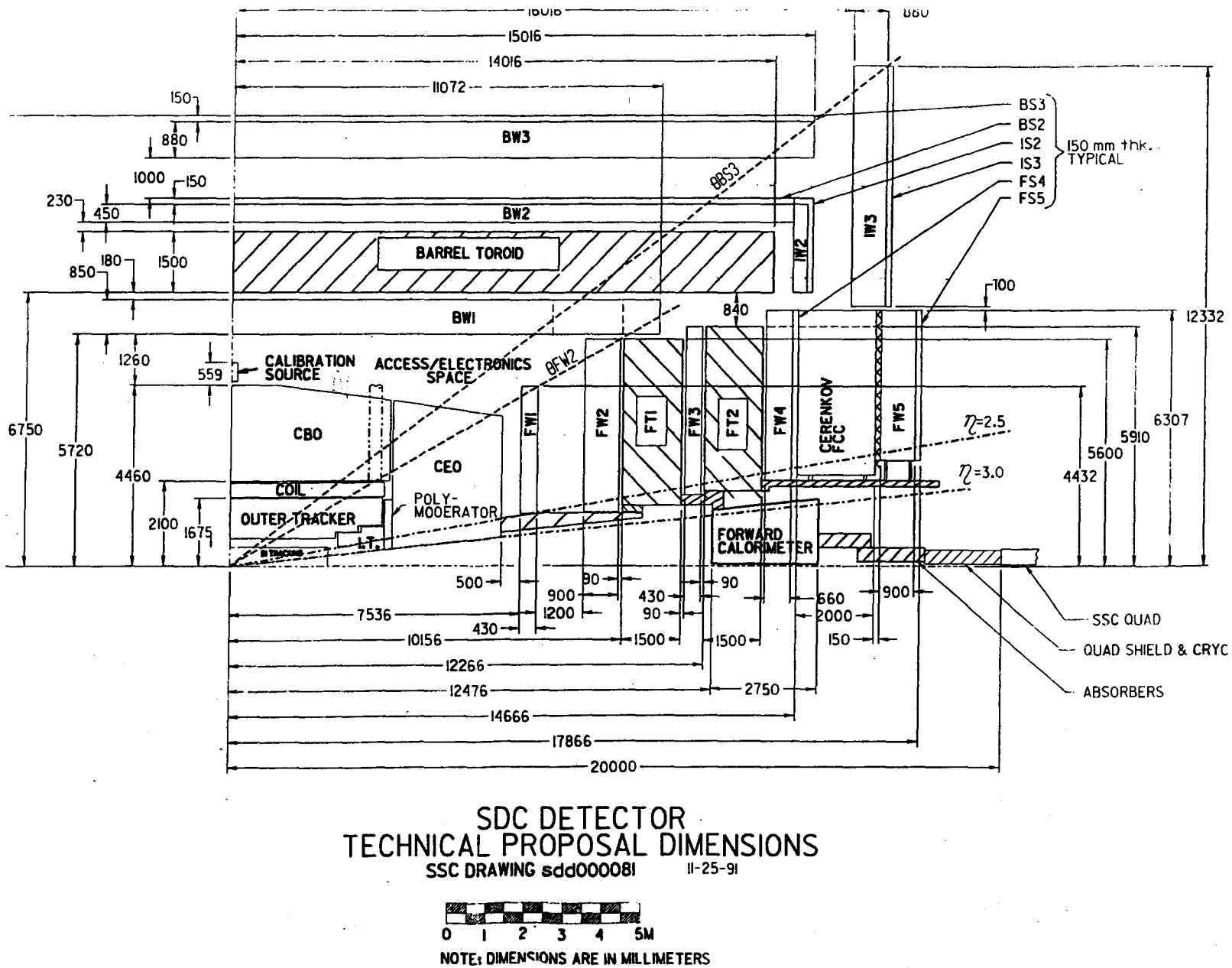

SDC DETECTOR
TECHNICAL PROPOSAL DIMENSIONS
SSC DRAWING sdd000081 11-25-91

0 1 2 3 4 5M

NOTE: DIMENSIONS ARE IN MILLIMETERS

Figure 1.2. SDC ɔr layout (quadrant view).

2.0 DESIGN CONCEPT

In this concept the basic sensing element is a 75 mm OD aluminum drift tube with 1.6 mm wall thickness. These tubes may contain field shaping electrodes (see Section 4) which must be oriented normal to the direction to the beam interaction point. These tubes are also spaced such that a particle path from the interaction point is projective through multiple tube layers. Figure 2.1 shows this geometry for the BW1 theta tubes. The projective tube layers 2 and 4 shown in Figure 2.1 are offset from the 1 and 3 tube layers such that a particle track does not travel through the tube walls in one projective layer and the tube centers in the other. The tube spacing must increase from layer to layer to maintain this projective geometry. However, to maintain structural integrity the tubes must be glued together at their tangent points. This is accomplished by gluing spacers between the tubes. Figures 2.2–2.5 give an overall view of the muon modules projective geometry for the theta and stereo layers.

The sense wires within the drift tubes have no support points within the tubes. They are located at their ends by crimped "feed throughs" which are located by CNC machined holes in the end caps. In order to know the position of all points along the wires, the wire tension must, therefore, be accurately controlled at assembly and the positions of the endcaps must be precisely controlled by the chamber structure. All drift tubes are identical except for length. The drift tubes are assembled into modules for each of the detector layers and on each face of the toroid.

The chamber layout proposed is shown in Figure 2.6 and consists of 3 'towers' per face of the octagonal toroid magnet. Each tower consists of a BW1 module mounted on rails on the inner surface of the toroid and a BW2/BW3 assembly mounted on rails on the outer surface as shown in Figure 2.7.

The tube layers are arranged as shown in Table 2.1:

TABLE 2.1. LAYER CONFIGURATION AND CHANNEL COUNT.

MODULES	LAYER CONFIGURATION	TOTAL TUBE (CHANNEL) COUNT	MAXIMUM WEIGHT (klb)
BW1	4θ, 4ϕ	15188	11100
BW2	4θ	12048	7760
BW3	4θ, 4ϕ, 2 stereo	28992	24000
IW2	4θ	1600	1000
IW3	4θ, 4ϕ, 2 stereo	15456	11000
Total		73284	

Figures 2.8 and 2.9 show the drift tube layout for the IW2 and IW3 modules, respectively. Note that the ends of the modules are cut at 22.5 degrees to match the octagonal shape of the toroid and maximize the detector coverage. The breaks between the towers are in planes dividing the BW3 layer into 3 equal parts. The middle modules on all layers are thus of the same length (9480 mm). The end modules have different lengths as shown in Figure 2.10. The weight of the heaviest module of the layer is given in Table 2.1.

The internal structure of a typical module section is shown in Figure 2.11. The basic principle is that the drift tubes are used as structural members. The outer skins of the modules are made from 6 mm aluminum plate. The first layer of tubes is layed on this plate and fastened to it with a structural epoxy adhesive. The tubes are also glued together at their tangent points. A 1.6 mm aluminum plate is then glued on top of the layer of tubes. Additional layers of tubes are then added as needed for a given

module and the final 6 mm outer skin is then glued in place. The result is a very strong, light, stiff sandwich structure which can meet the requirement for minimal deflection of these chambers.

The structure around the perimeter of each module has to provide the precision locations for the end caps of the drift tubes, allow for electrical and gas connections and transfer loads from the support points to the module structure. A typical cross section of this structure is shown in Figure 2.12. The core of this structure is the tube end plate (see Figures 2.13 and 2.14). This has CNC machined locations for each endcap plus a number of access holes for electrical and gas connections. At one end of the drift tube, the location is a precision round hole which mates with the precise boss on the end cap. Because this end is inserted first at assembly, it has to enter at a small angle. The hole is cut away on each side of the end plate to allow this but still give precise location when the tube is finally oriented (see Figures 2.15, 2.16a and 2.16b for details). The tube is free to rotate in this hole. At the far end, the tube is located by two dowel pins which are pushed in after the tube is dropped into place. The dowel holes are CNC machined in the end plates and, as they control the orientation of the tubes, they provide the correct orientation of the field shaping electrodes. The precise location of the locating and dowel holes is vital to the precision of the whole module. Rather than rely on holding the needed tolerances along the whole length (up to 9.5 m) of the end plate, fiducials will be provided at 2 m intervals. Hole locations will be known with respect to these and the fiducial locations can be determined on the alignment stand after module assembly. All machined locating holes and fiducials will be known to CNC mill accuracy (12 μm).Machining will be done in a temperature controlled environment.

The rest of the peripheral structure of each module consists of top and bottom rails which connect the end plates to the top and bottom 6 mm plates discussed above and to a set of outer plates. The whole arrangement forms a very strong, stiff periphery to the module. The end plates and outer plates are 19 mm thick and the top and bottom rails are 25 mm thick. The top and bottom rails have CNC machined locations for the tube end plates and also locate precisely into the outer plates as shown in Figures 2.17 and 2.18. This edge structure provides the strength and rigidity needed for the module attachment points and for module handling during transport and mounting on the detector. The space shown between the end plates and the outer plates allows room for the electrical and gas connections to the tubes. For the BW2 modules this space is reduced to 10 mm on the module sides which have no tube connections as shown in Figure 2.10. These modules contain only θ tubes. For the BW1 modules, the outer plates terminate at the top and bottom surfaces of the rails and the whole module is attached to the inner surface of the toroid at points on the top rails.

The BW2/BW3 assembly follows the idea of making full use of the materials in the structure. The two modules must be precisely and rigidly connected together as a unit which is then installed on the toroid. This is achieved by extending the outer plates of the peripheral structure to connect the modules as shown in Figure 2.19. Note that the top and bottom rims of the modules connect to precise slots which are CNC milled in the outer plates. As these plates are very stiff in shear and extend completely around the modules as shown in Figure 2.20, the result is a very stiff structure which automatically gives accurate alignment between BW2 and BW3. The plates are made in 2 m sections and do not have to be continuous 9 m lengths. Access holes can be readily left to provide ventilation and allow work on electronic packages etc. which may be mounted between the modules. (Note: the very large holes shown in Figure 2.20 are for illustrative purposes only. In practice, a smaller number of access ports would be used.).

2.1 Module Assembly

Each module is to be assembled on site at the SSC using a precision, flat assembly pad. First the end plate and bottom rails for each side of the module are bolted together. Support jigs are mounted on the work pad and accurately surveyed in. The end plate/rail assemblies are then mounted on these jigs (Figure 2.21) and the corners are bolted together. A set of 19 mm spacers is placed on the work pad to support the sections of 6 mm bottom plate which are then laid down and glued in place and allowed to set up. The 6 mm top and bottom plates are laid down as a set of large 'tiles' and have overlapping, 100 mm × 6 mm doublers along the joints. These doublers are bonded to two adjacent edges of each tile prior to shipping. The 1.6 mm plates are also laid down as tiles, but without doublers. The basic structure is now defined. The layers of tubes and 1.6 mm plates are now installed. The support jigs can now be removed and the top 6 mm plate sections and top rails installed. For BW1 modules, assembly is completed by bolting the outer plates in place. For the BW2/BW3 assembly, outer plates for the two sloping sides and one vertical side are installed on the BW2 module (still on its assembly pad). The completed BW3 module is lowered into place and the final outer plate installed. The whole assembly is then finally bolted together and is ready for survey.

The scintillators are easily mounted in the design, since the space between BW2 and BW3 is not occupied by a truss structure. Upon completion of the BW2 module, before BW3 is mated to it, BS2 is attached to the flat, top panels with simple mounting brackets. After BW3 is attached to BW2 the BS3 scintillators are attached to the top panels of BW3.

2.2 Module Supports

The support conditions required for BW1 are:

In the plane of the octant face – purely kinematic.

Normal to the octant face – displacement restrained at 4 points. Each support point is placed 2 m in from the corners along the long edges (Figure 2.22).

It is assumed that Lee Controls roller bearing double pillow blocks are used, (see Figure 2.23). Considering the module on octant 1, the top face of the detector, this represents the worst load case as Lee specifies that the load rating should be reduced by 50% for load in this direction. However, we can increase the load rating by 100% as we have an essentially static load. Given the module weight of 23800 lb, it is necessary to use a 3-in. diameter rail system. Figure 2.24 shows a detailed view of the BW1 rail mounting. Notice that the load is transferred to the very strong and stiff peripheral structure of the module. The small part of the bearing which extends over the tube/plate assembly is supported by a large (200 × 400 mm) spreader plate which is screwed and epoxy bonded to the structure. The pillow block is located accurately to the module top edge member using two shear pins and is attached with four 0.625-in. UNF bolts. Figure 2.24 shows both the 0.625 in. UNF bolt and a shear pin. Only two of the bearings need be located in this way. To make the supports kinematic in the plane of the module, the bearings on the other edge will use the "floating" mounts provided by Lee Controls.

Although, when supported as described, the deflection of the module is minimal, the module can easily accommodate a deflection of several millimeters of one of the support points out of the plane of the other three supports. Note also that this would only occur if the magnet iron face was to twist. Bending of the magnet would not produce any loads on the module.

The BW2/BW3 units can be separated in the same fashion as BW1 discussed above. In this case we may need 4-in. rails and bearings. It is also very likely that we could use a pure 3-point kinematic support as shown in Figure 2.25. The essential point is that BW2/BW3 form a single unit connected by side plates as detailed in Section 2.1.

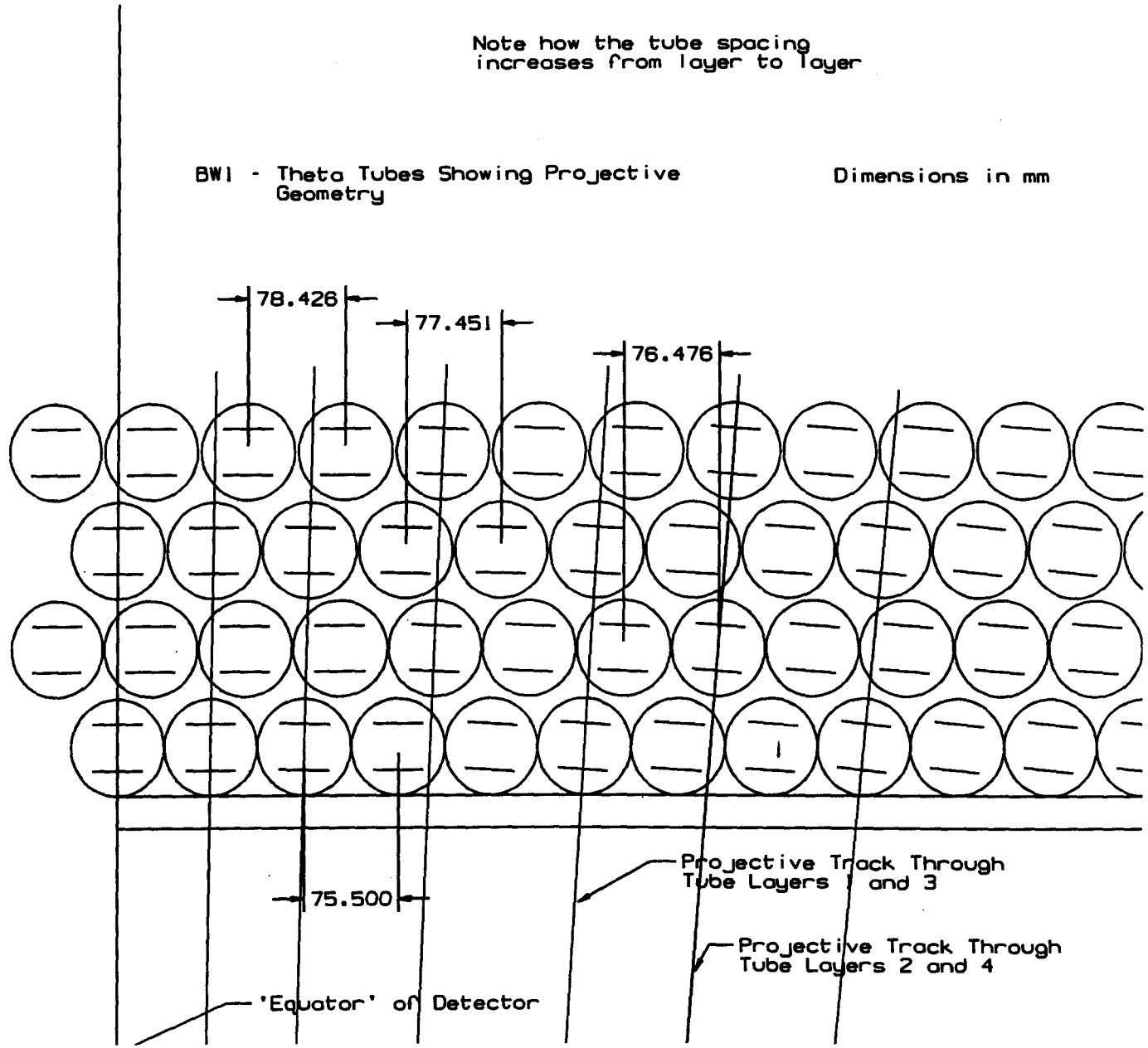

Figure 2.1. Projective geometry of BW1 θ tubes.

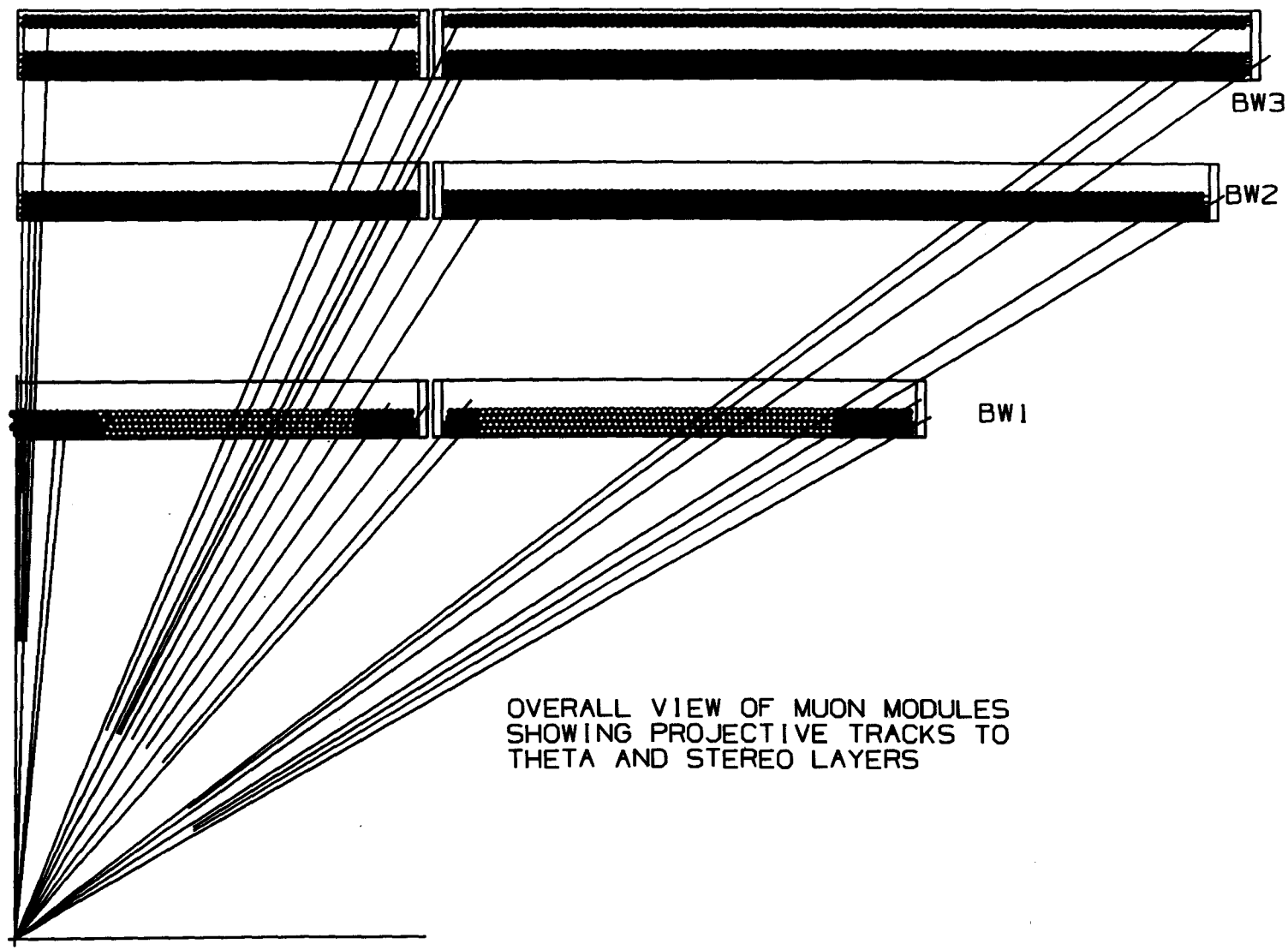

Figure 2.2. Overall view of muon modules showing projective tracks to theta and stereo layers.

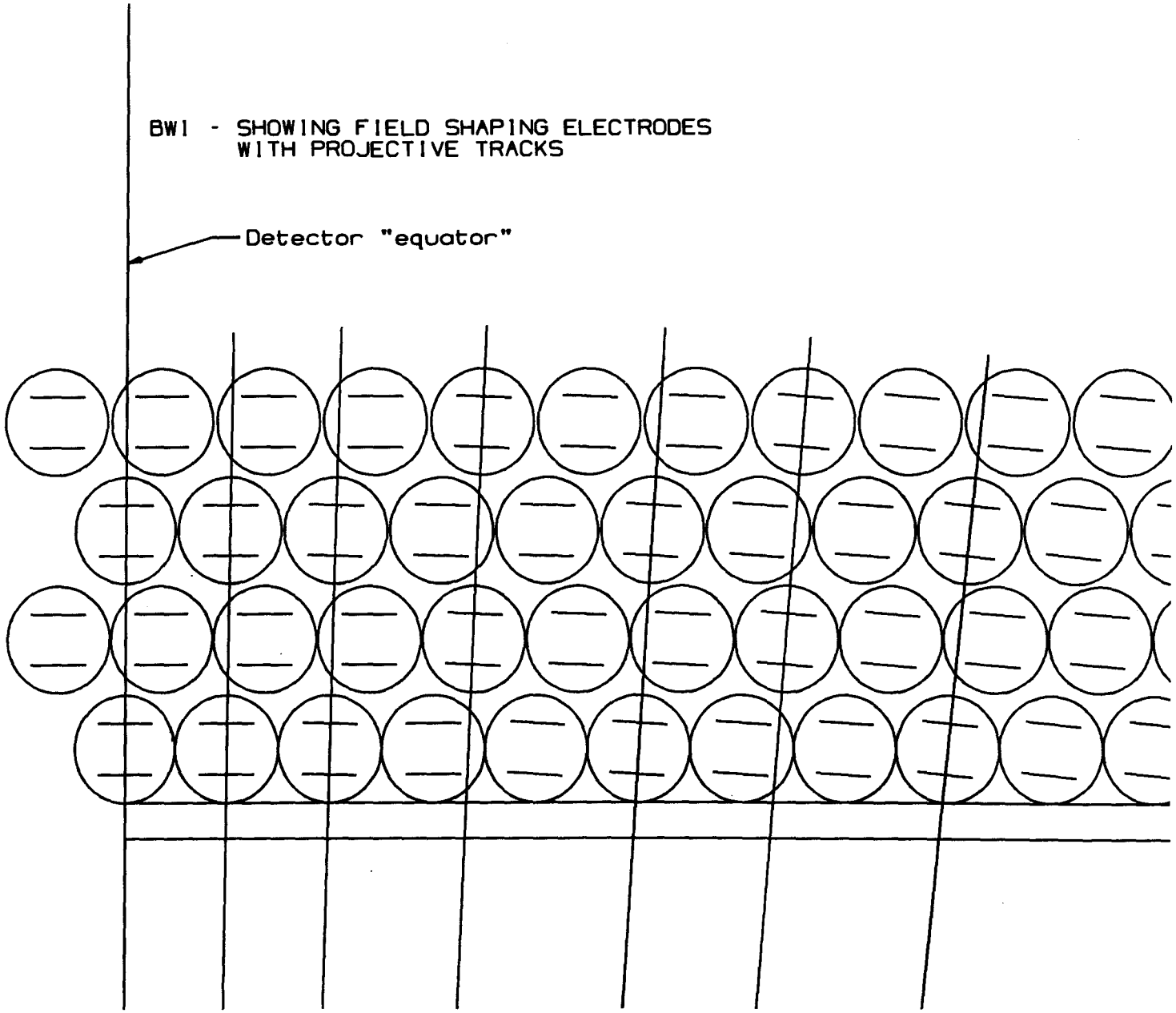

Figure 2.3. BW1—Showing field shaping electrodes with projective tracks.

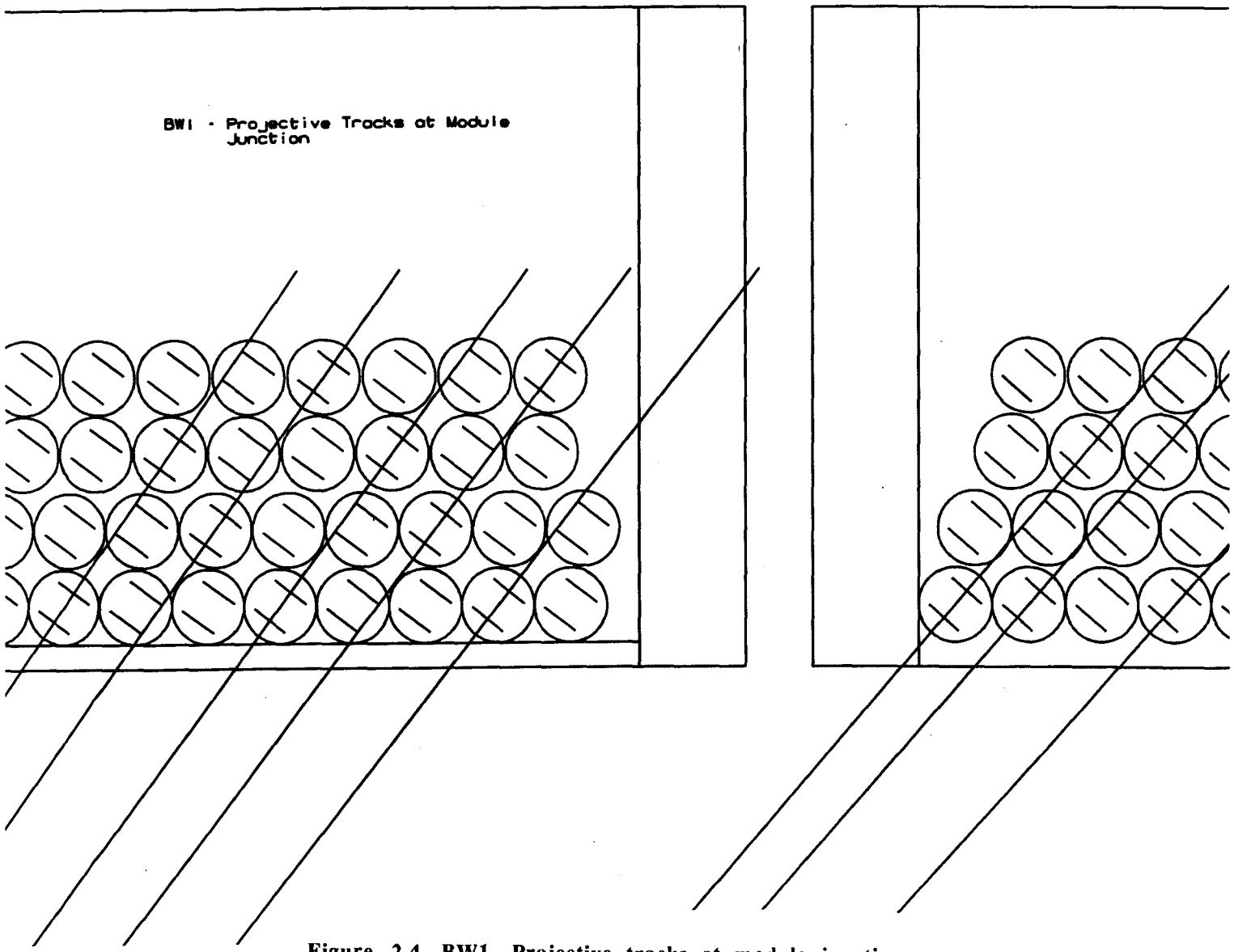

Figure 2.4. BW1—Projective tracks at module junction.

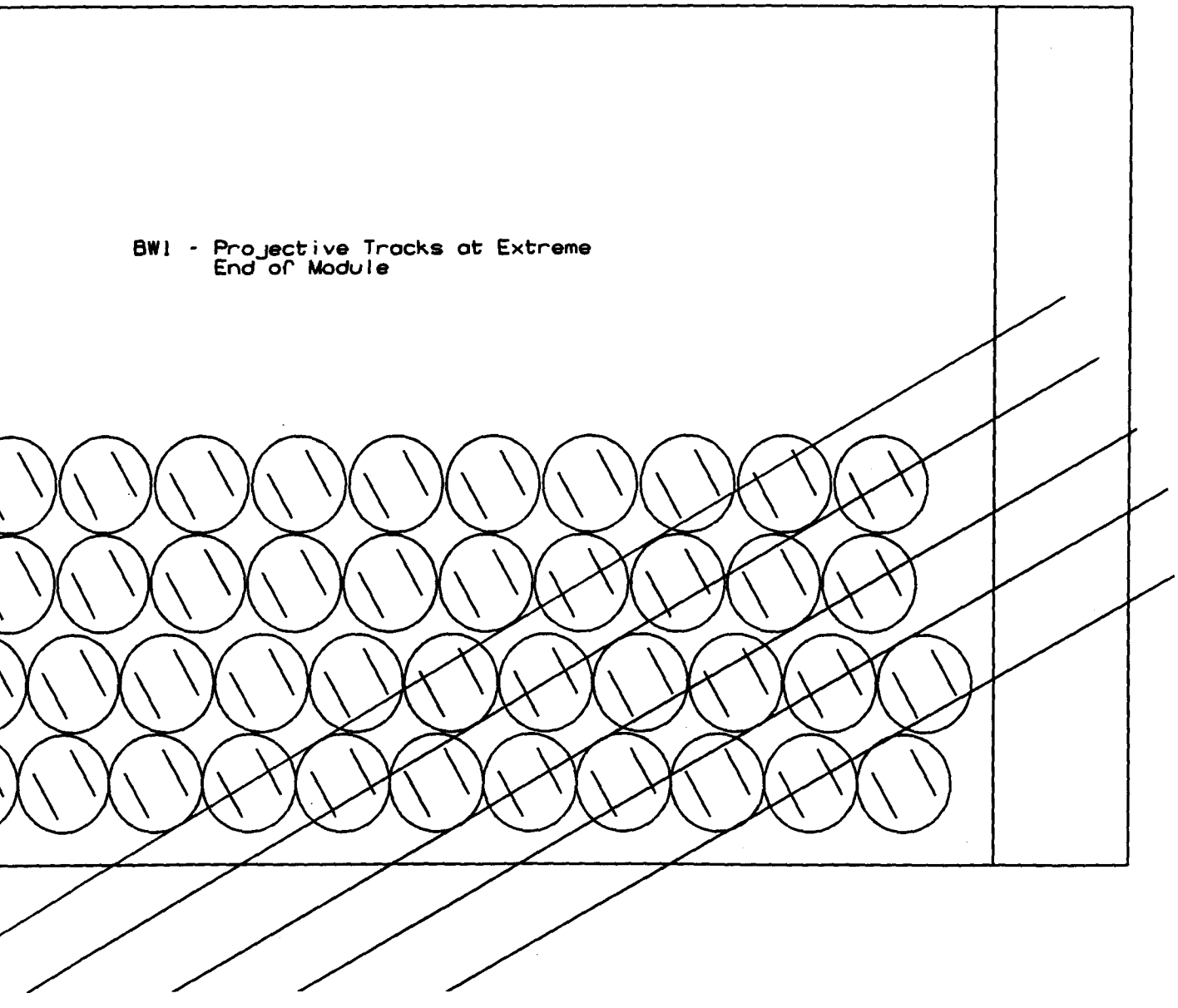

Figure 2.5. BW1—Projective tracks at extreme end of module.

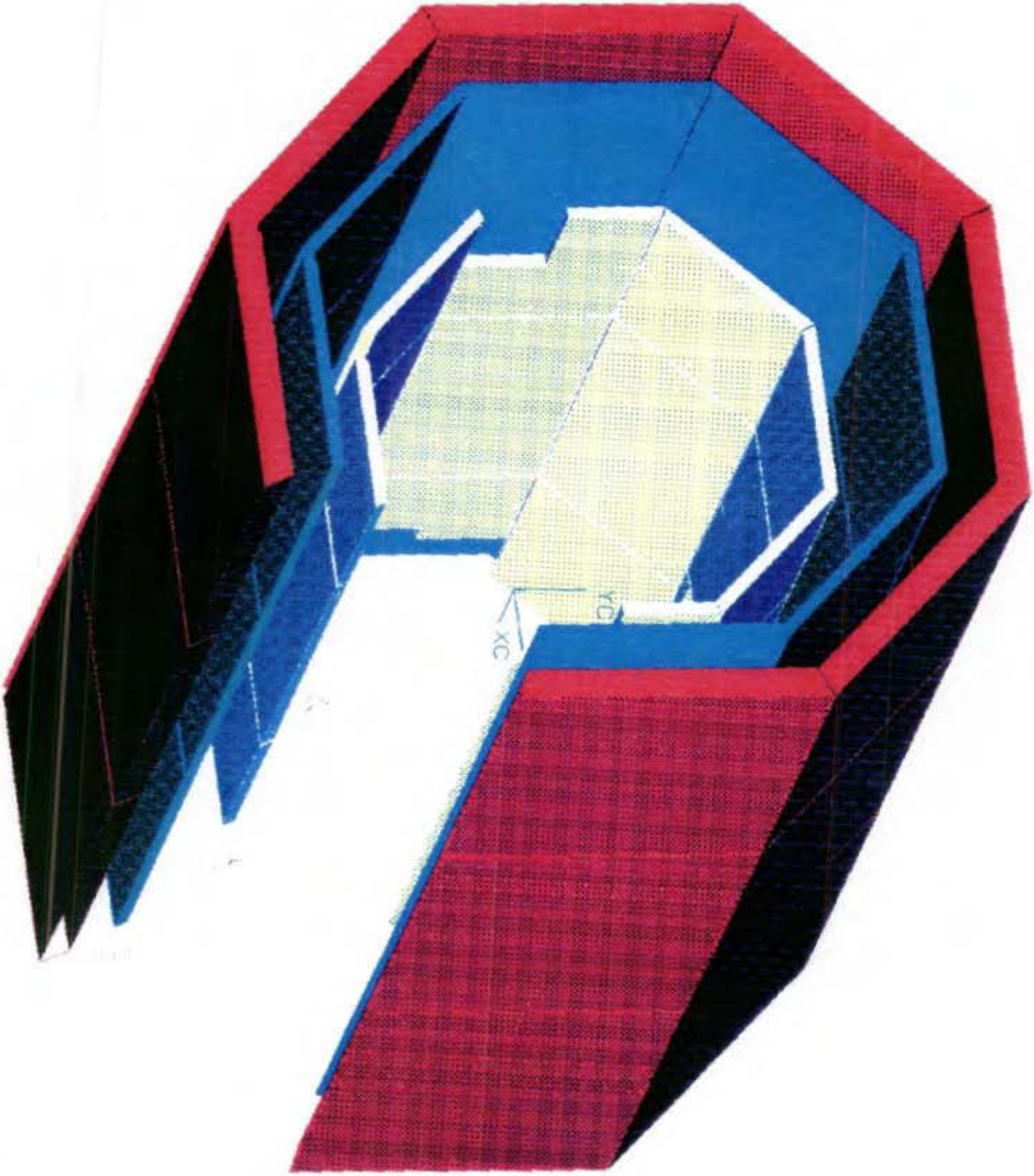

Figure 2.6. Module layout.

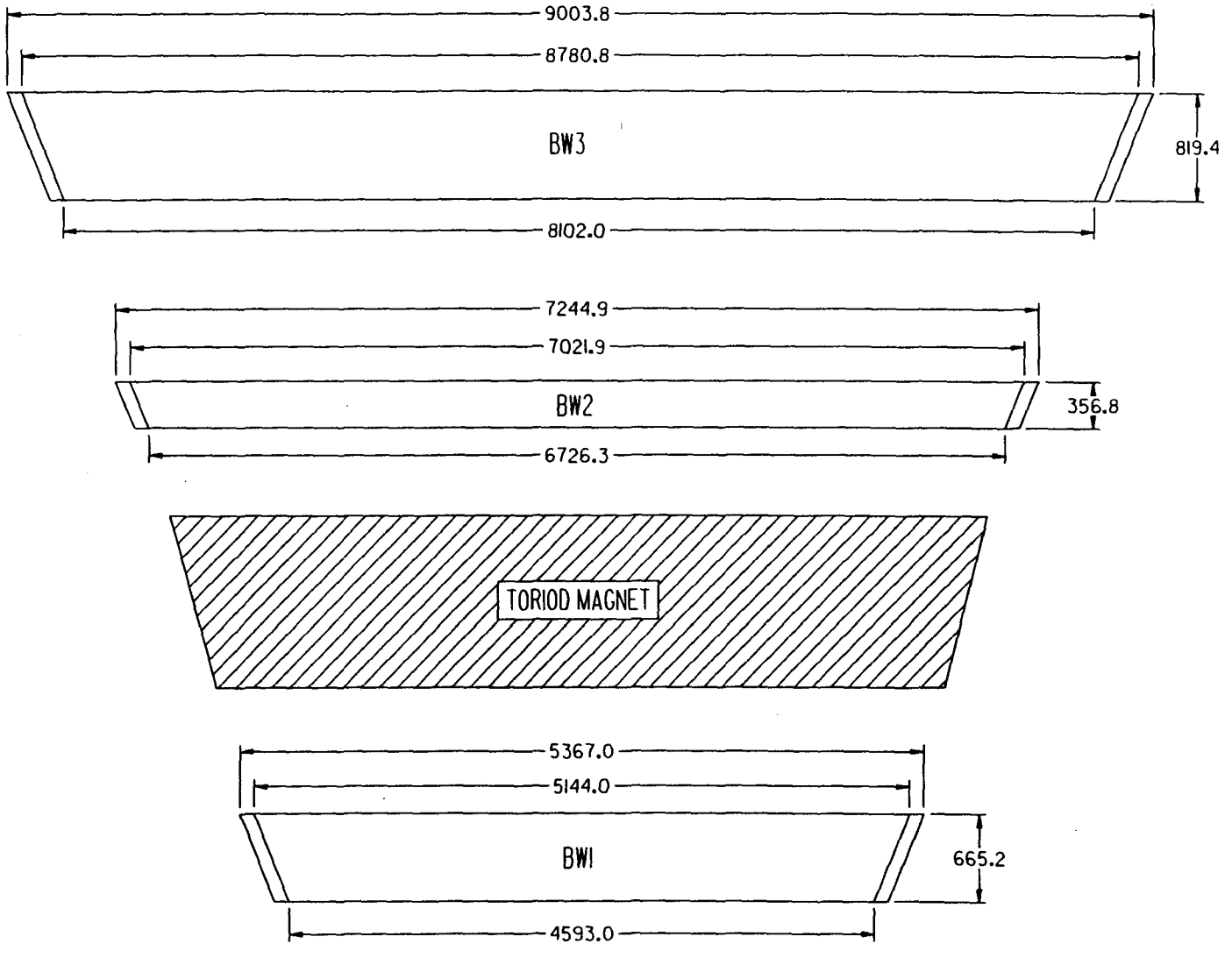

Figure 2.7. Module layers cut in plane perpendicular to z direction.

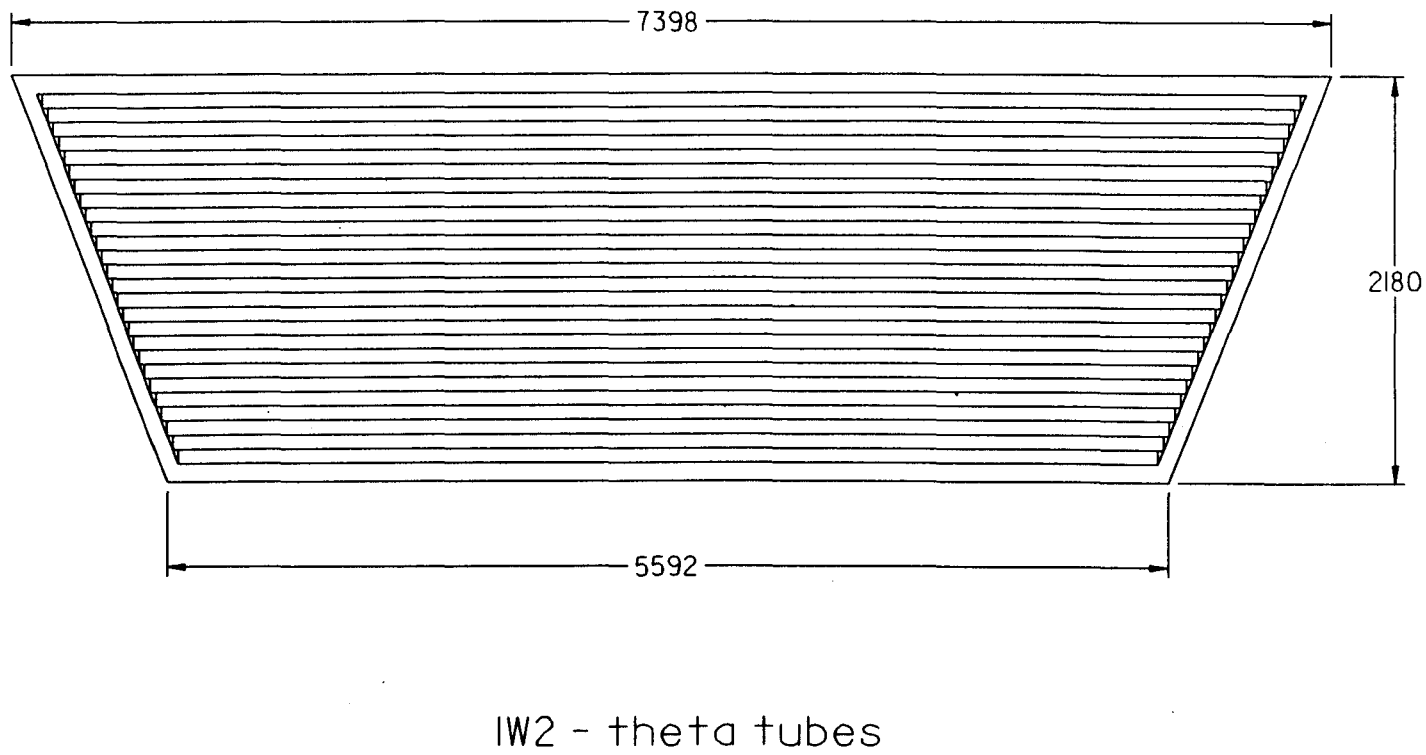

Figure 2.8. IW2—Theta tubes only.

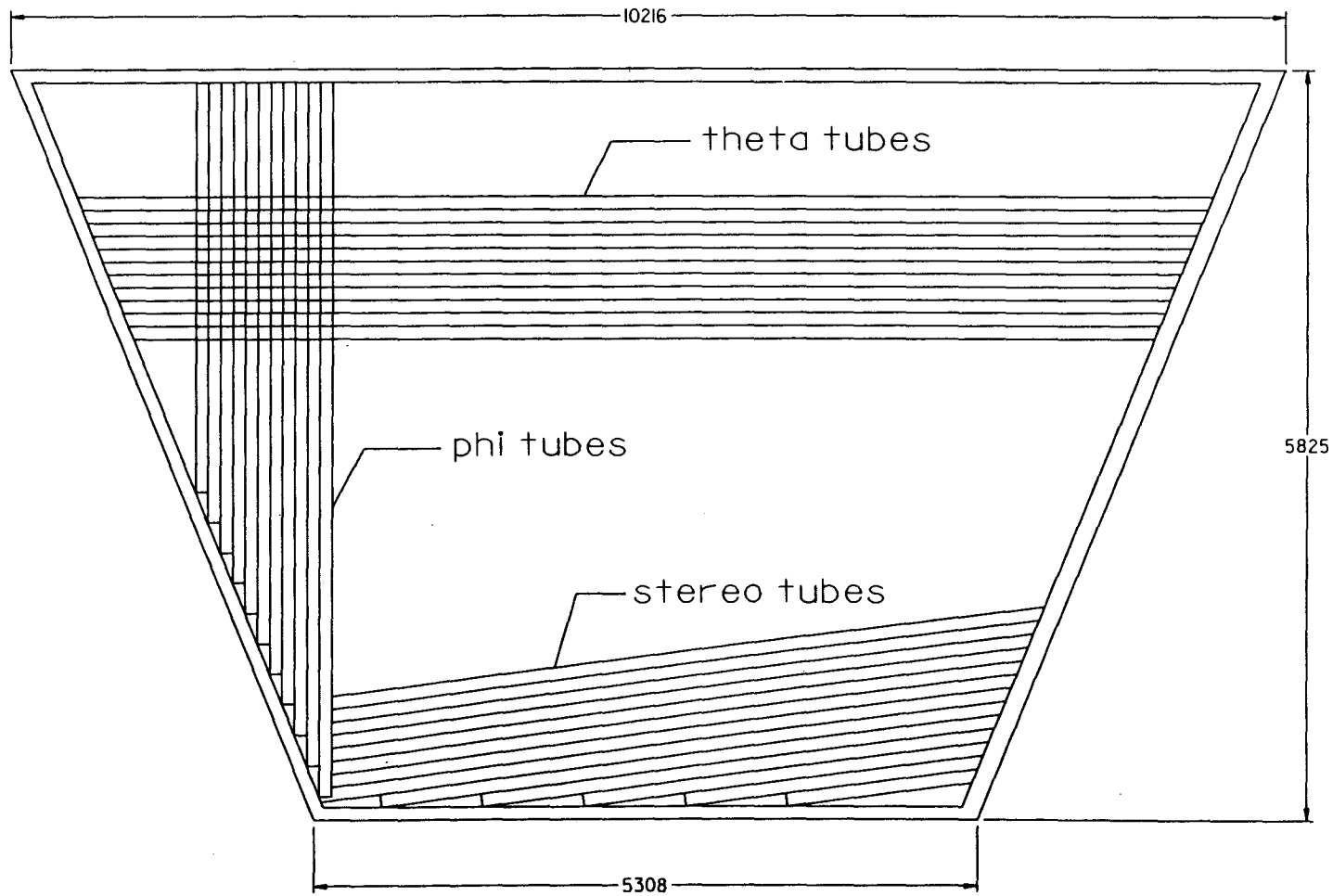

IW3 MODULE

Figure 2.9. IW3 module (showing θ, ϕ and stereo tubes).

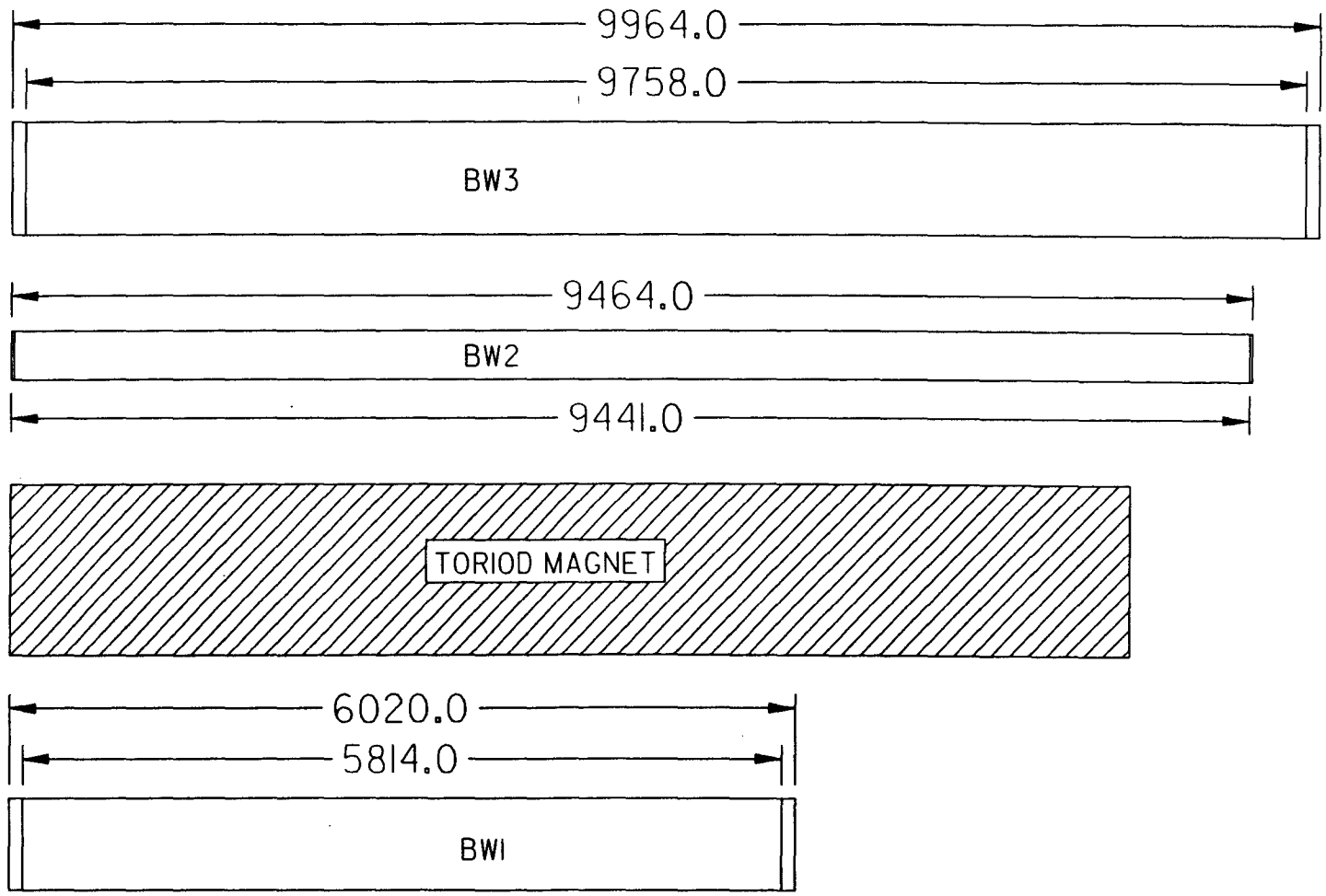

Figure 2.10. Space between tube end plates and outer plates.

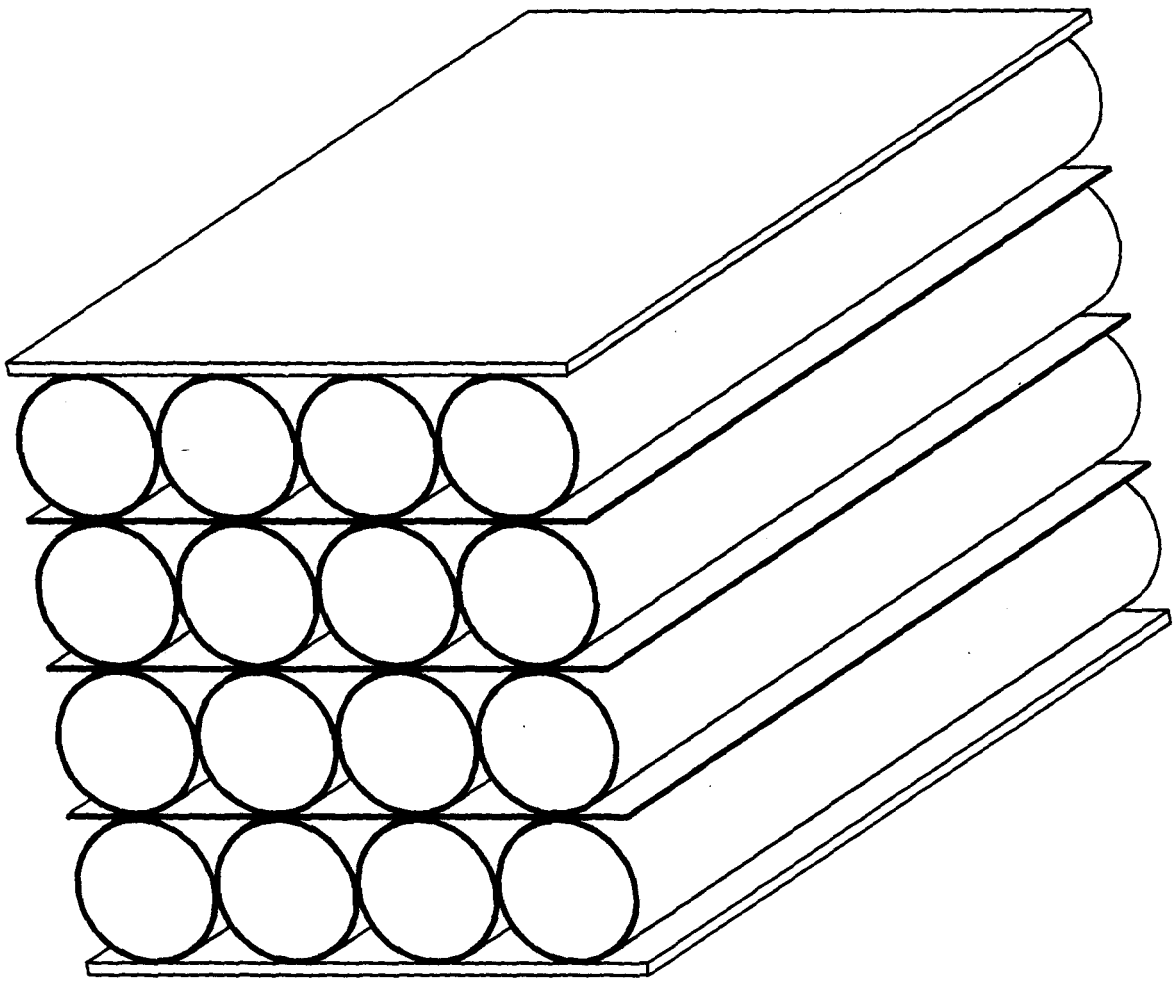

Figure 2.11. Internal structure of a typical 4-layer module.

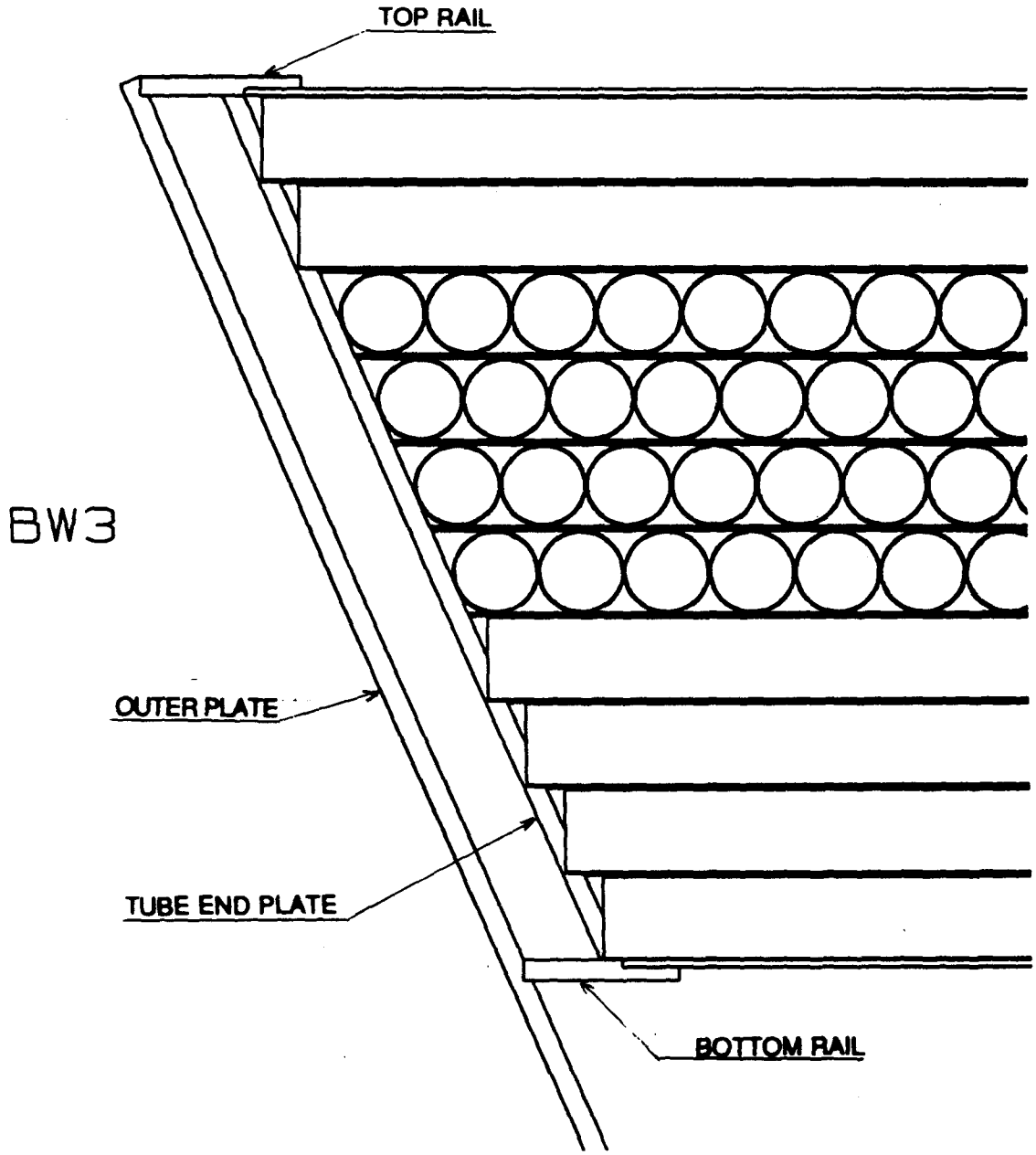

Figure 2.12. Cross section of module edge showing the tube end plate, top and bottom rails and outer plate. For this BW3 module, the outer plate continues down to the BW2 module to form a BW2/BW3 tower.

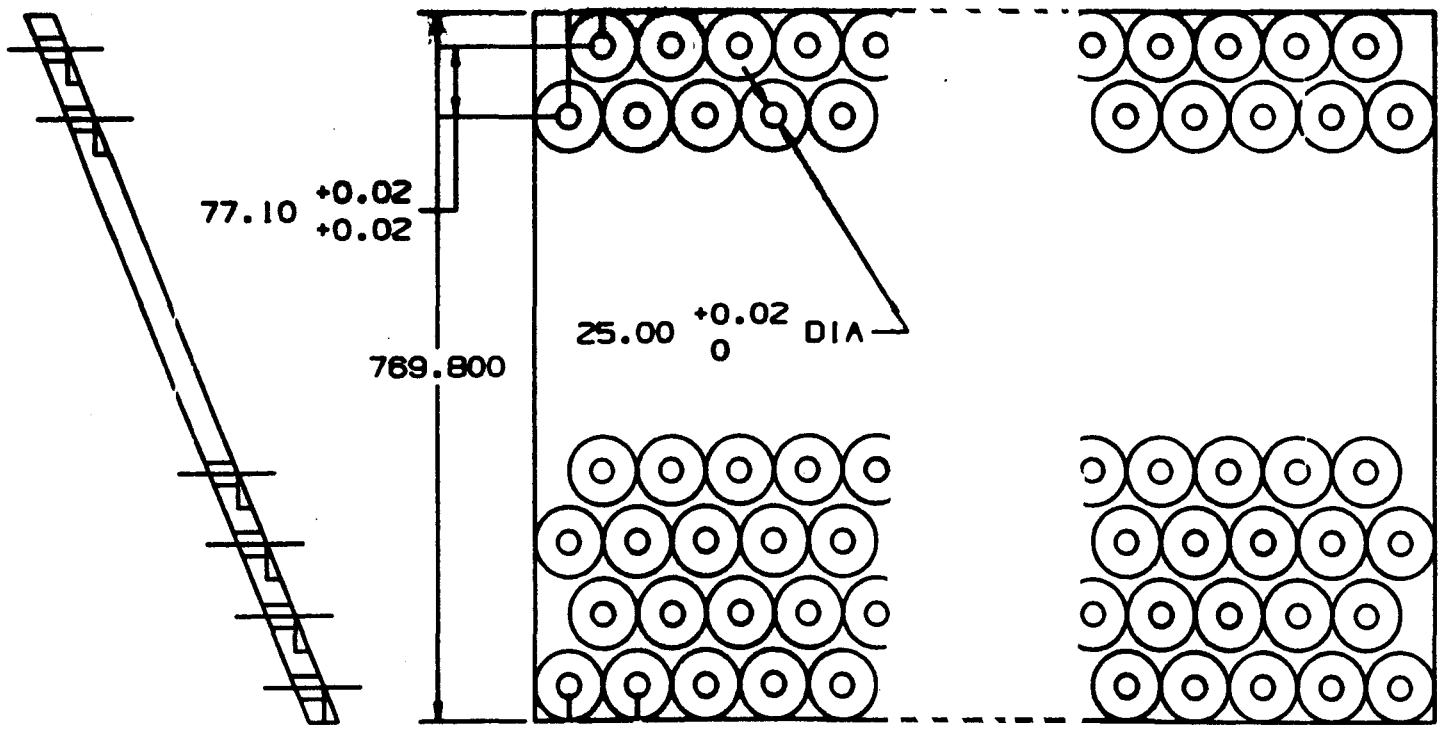

Figure 2.13. Tube end plate. This plate has precision machined locating holes for the drift tube end caps. Clearance holes for gas and electrical connections not shown for clarity.

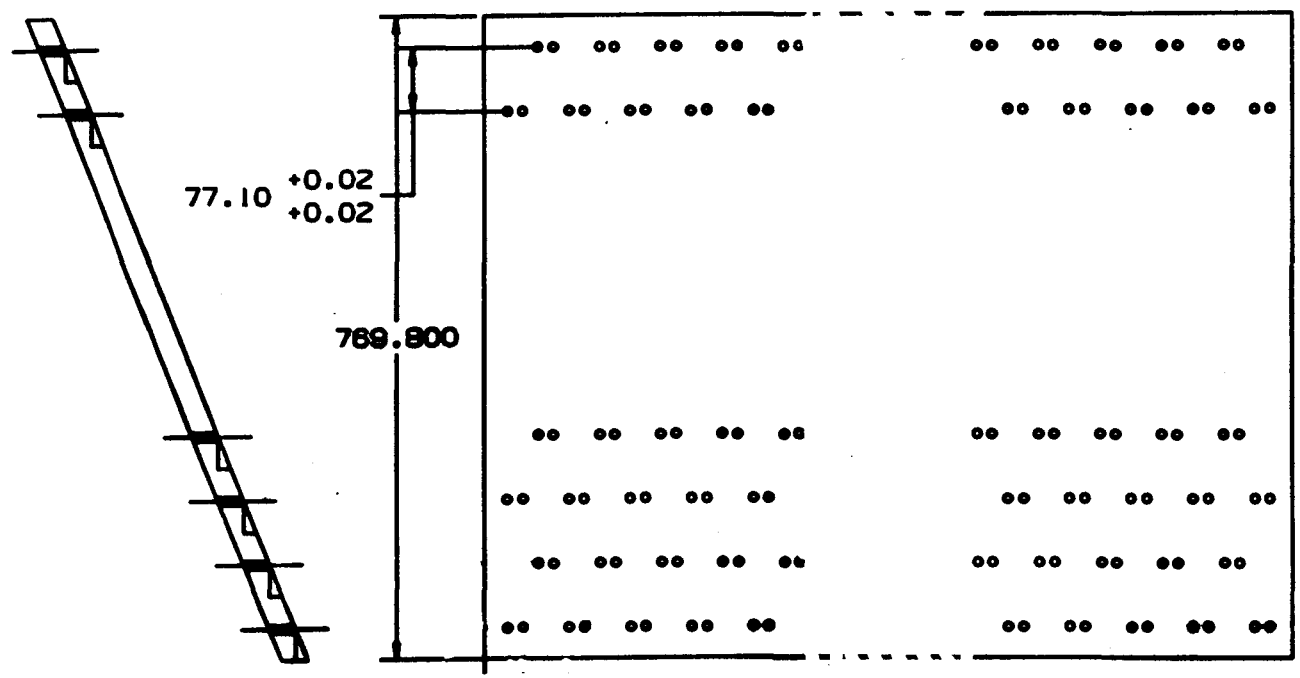

Figure 2.14. Tube end plate. This plate has precision machined dowel holes for the drift tube end caps. Clearance holes for gas and electrical connections not shown for clarity.

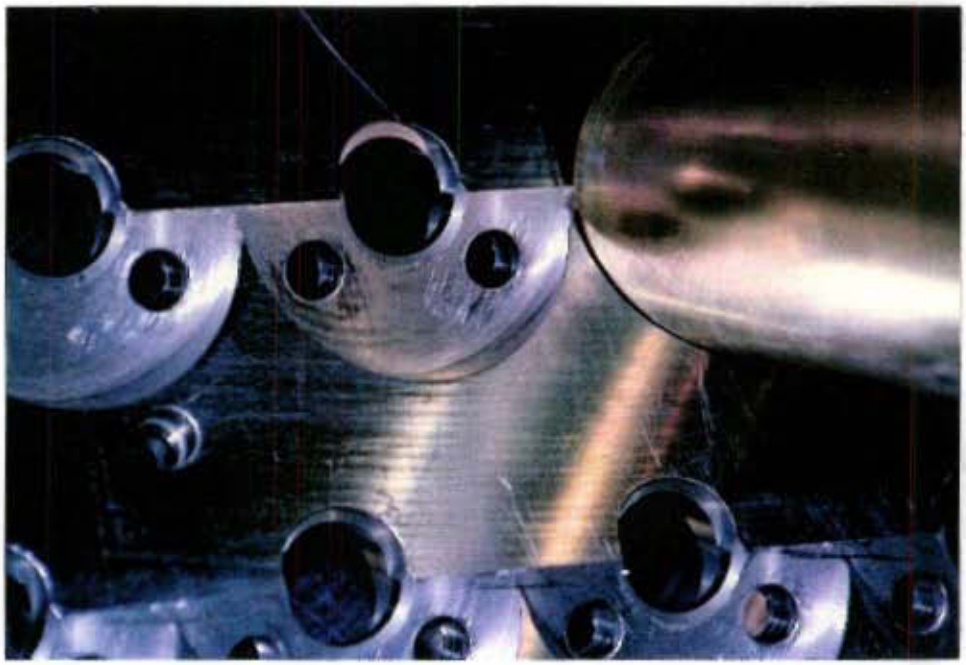

Figure 2.15. Detail of tube location in end plate.

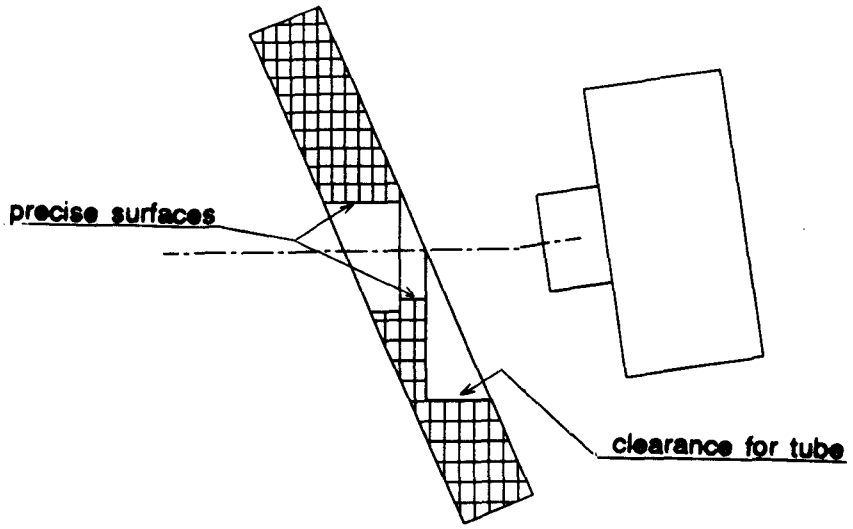

a) end cap approaching locating hole.

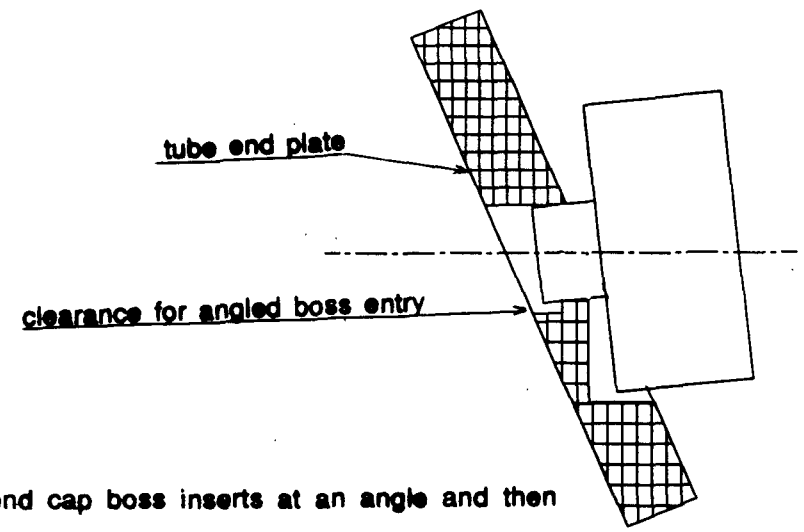

b) end cap boss inserts at an angle and then is rotated into horizontal location.

Figure 2.16. Cut away locating hole allows insertion of tube end cap boss at an angle while still providing precise location.

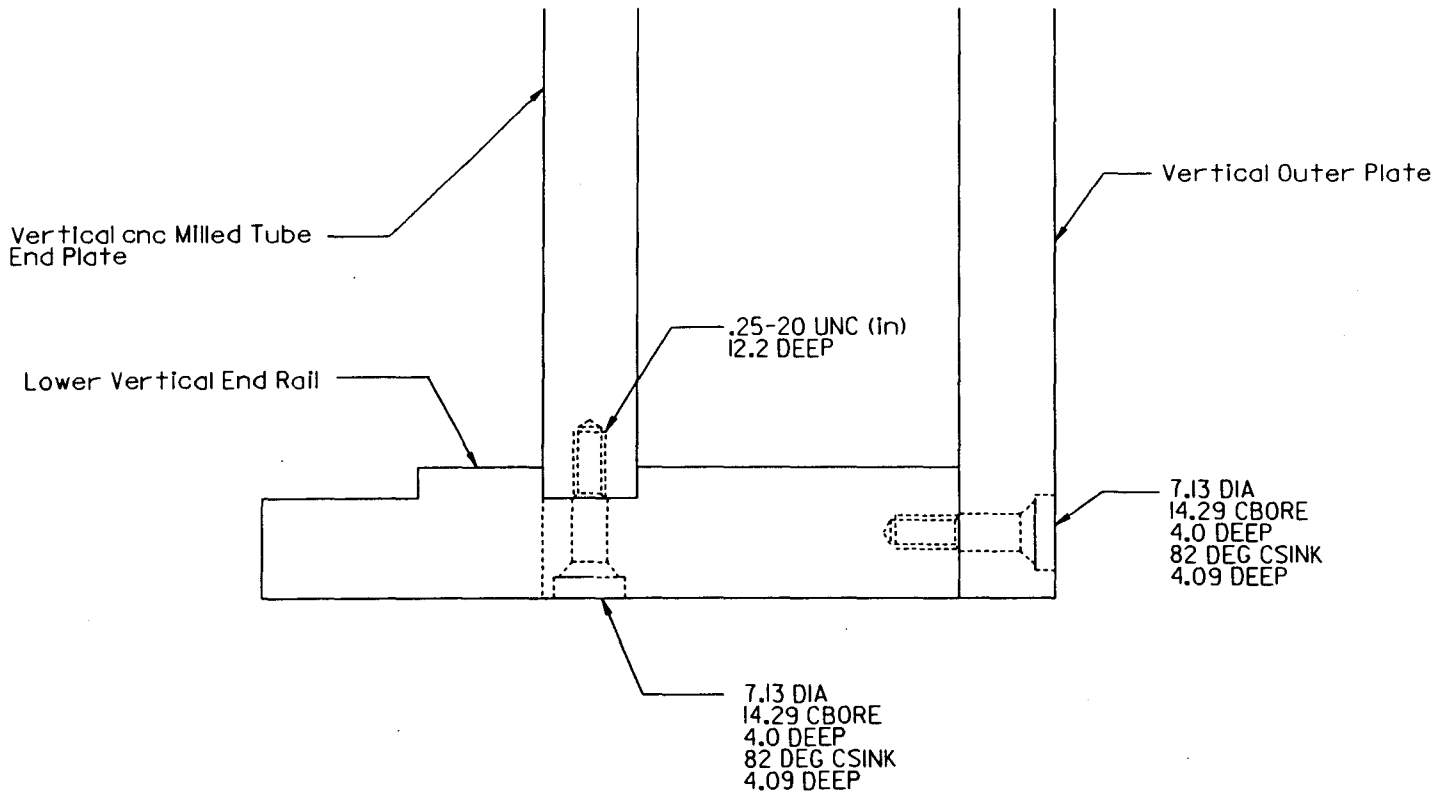

Figure 2.17. Assembly of bottom rail to vertical outer and tube end plates.

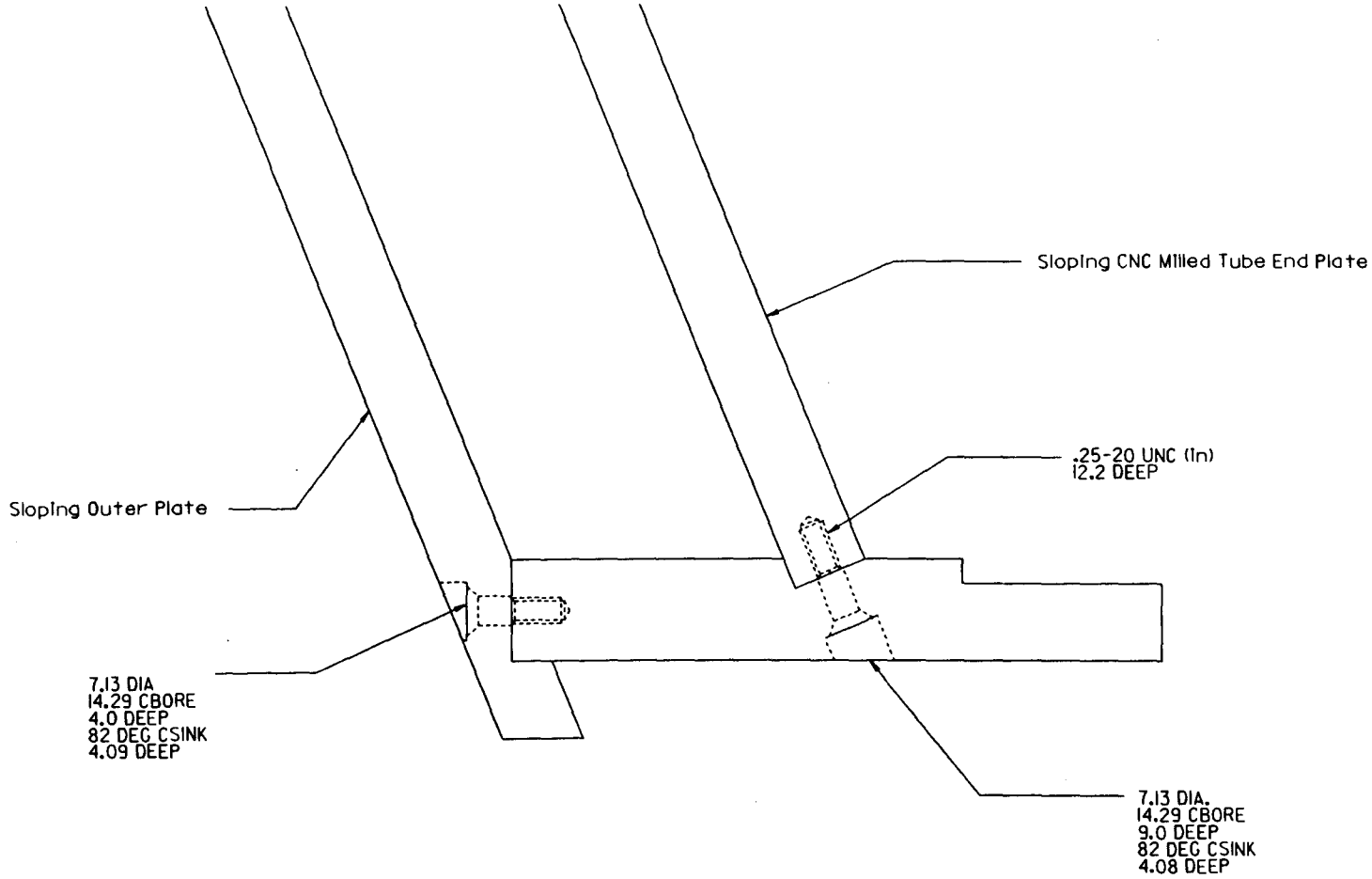

Figure 2.18. Assembly of bottom rail to sloping outer and tube end plates.

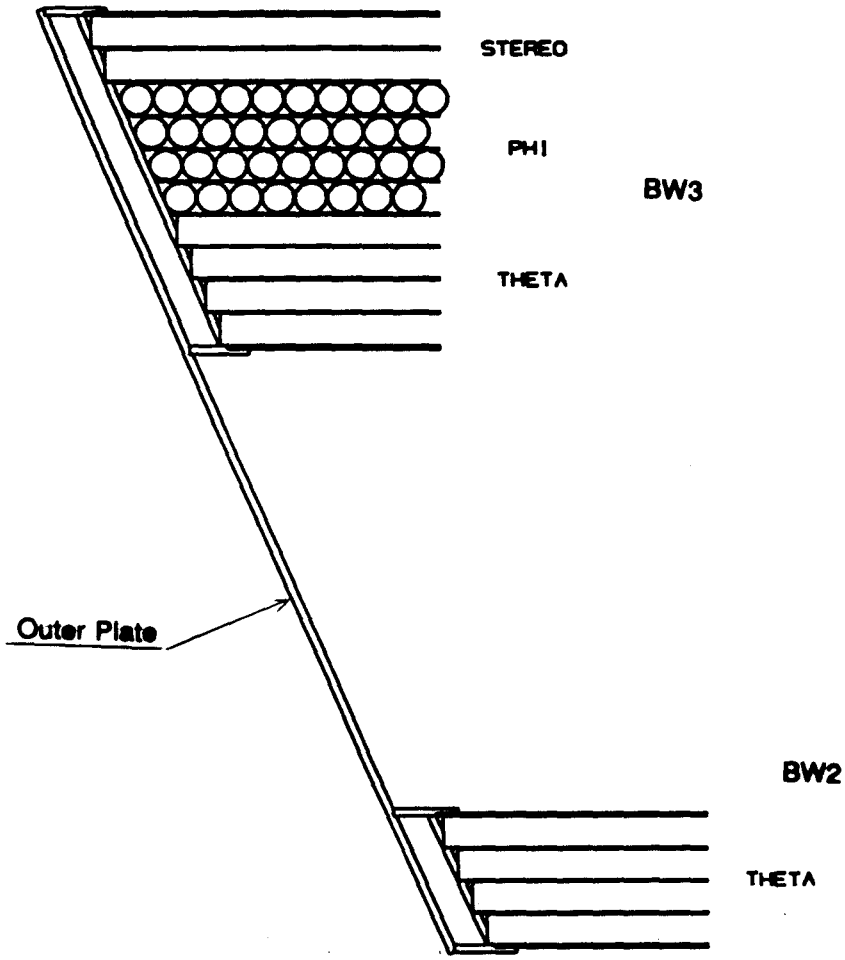

Figure 2.19. Outer plate connects BW2 and BW3 modules to form a tower.

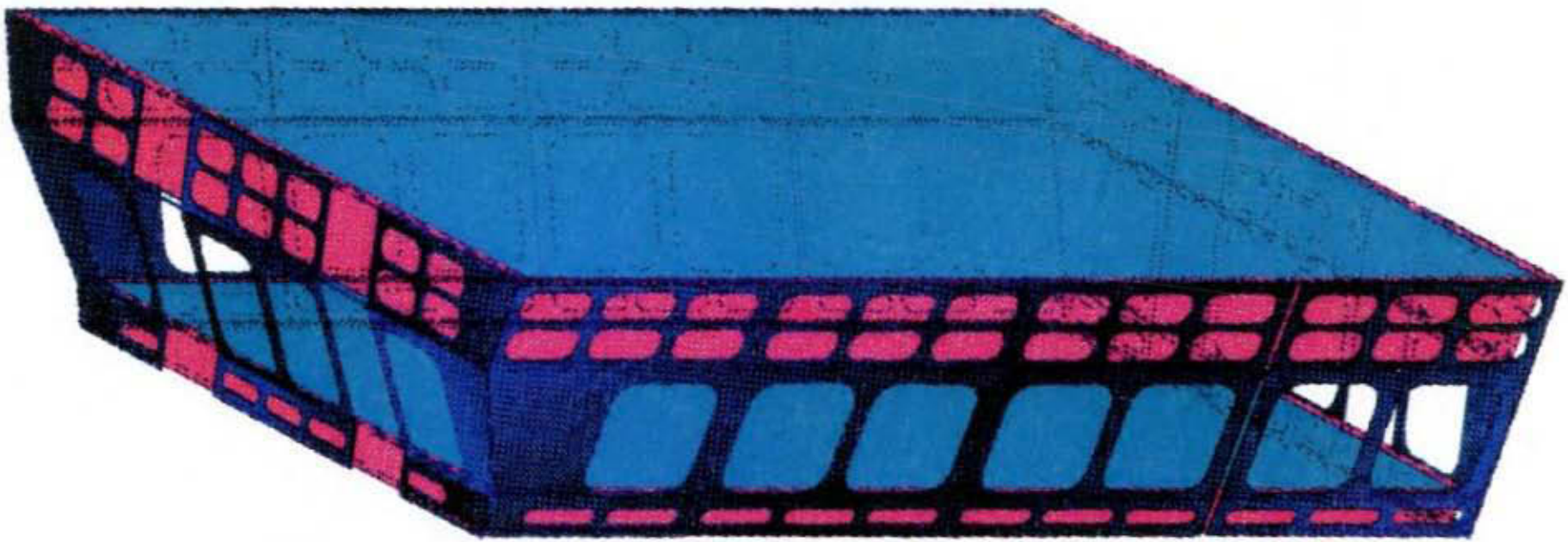

Figure 2.20. BW2/BW3 tower assembly.

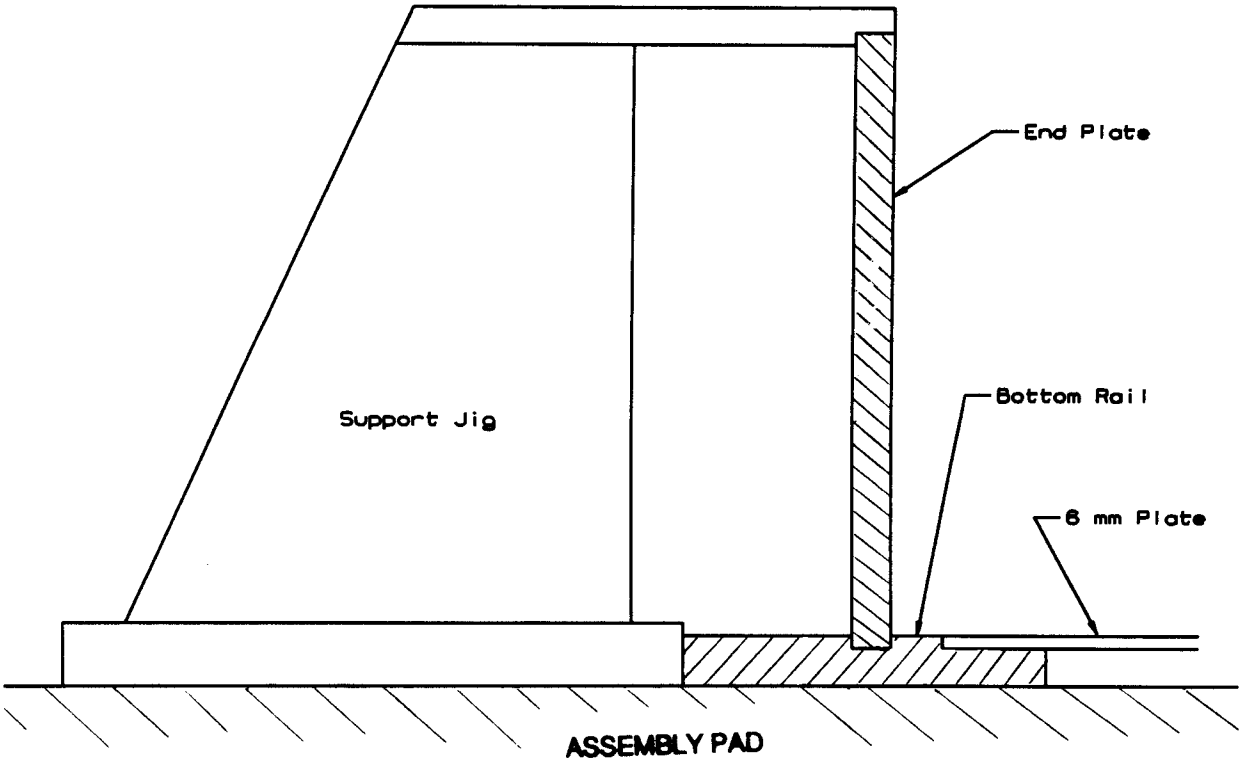

Figure 2.21. Tube end plate and bottom rail are supported by an assembly jig on the assembly pad while the tubes and plates are installed.

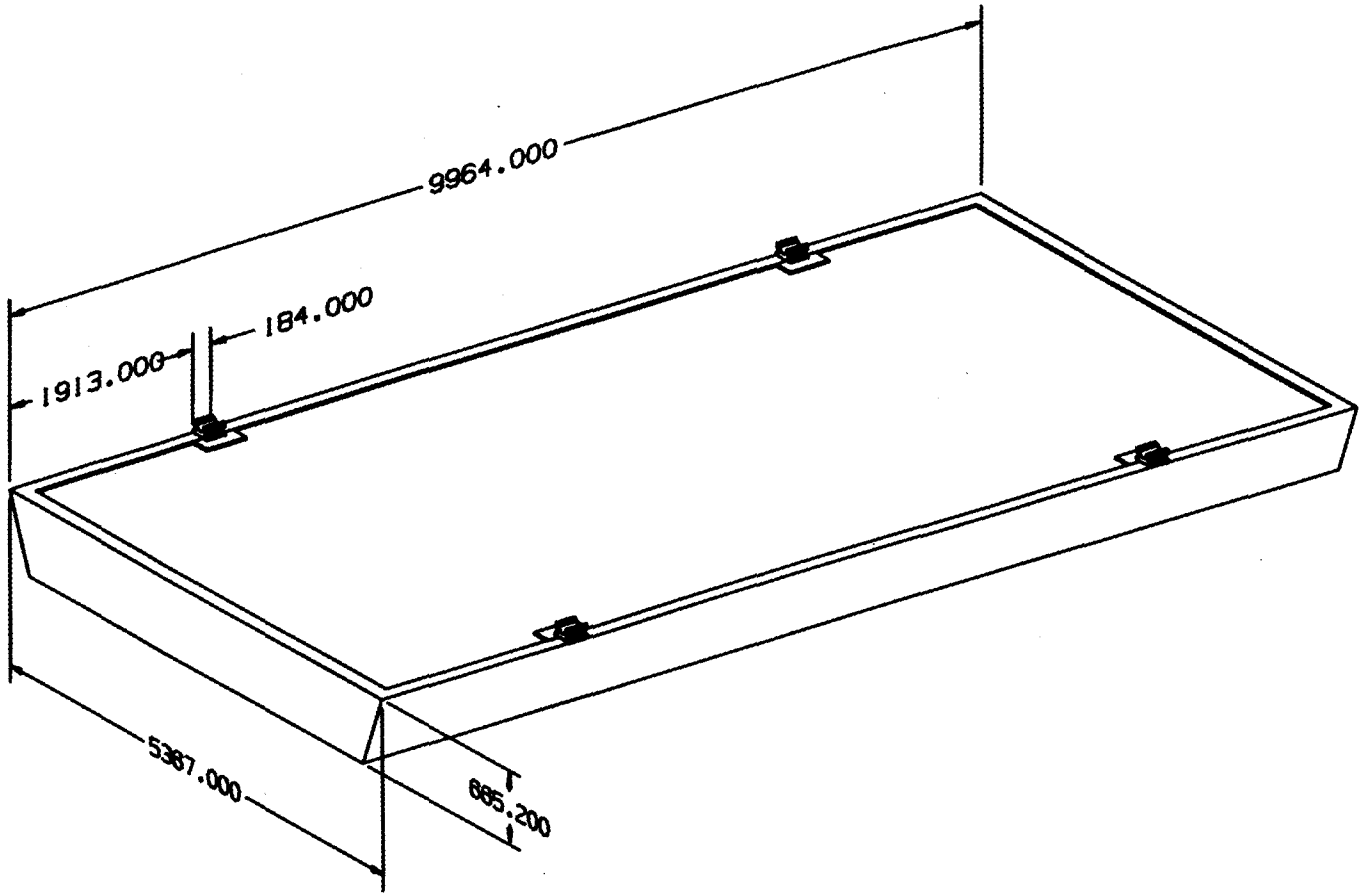

Figure 2.22. BW1 mounting structure.

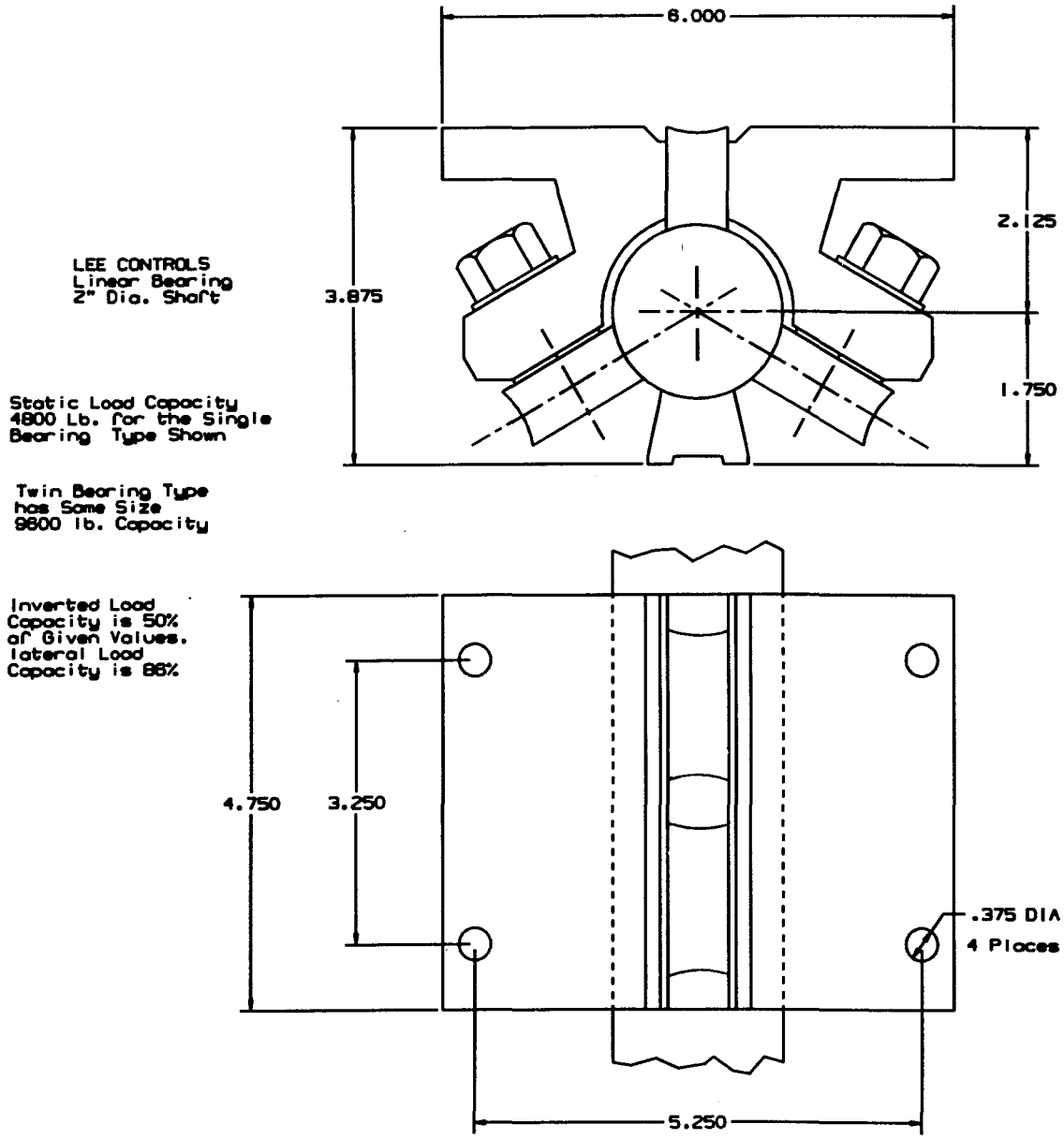

Figure 2.23. Lee controls roller bearing.

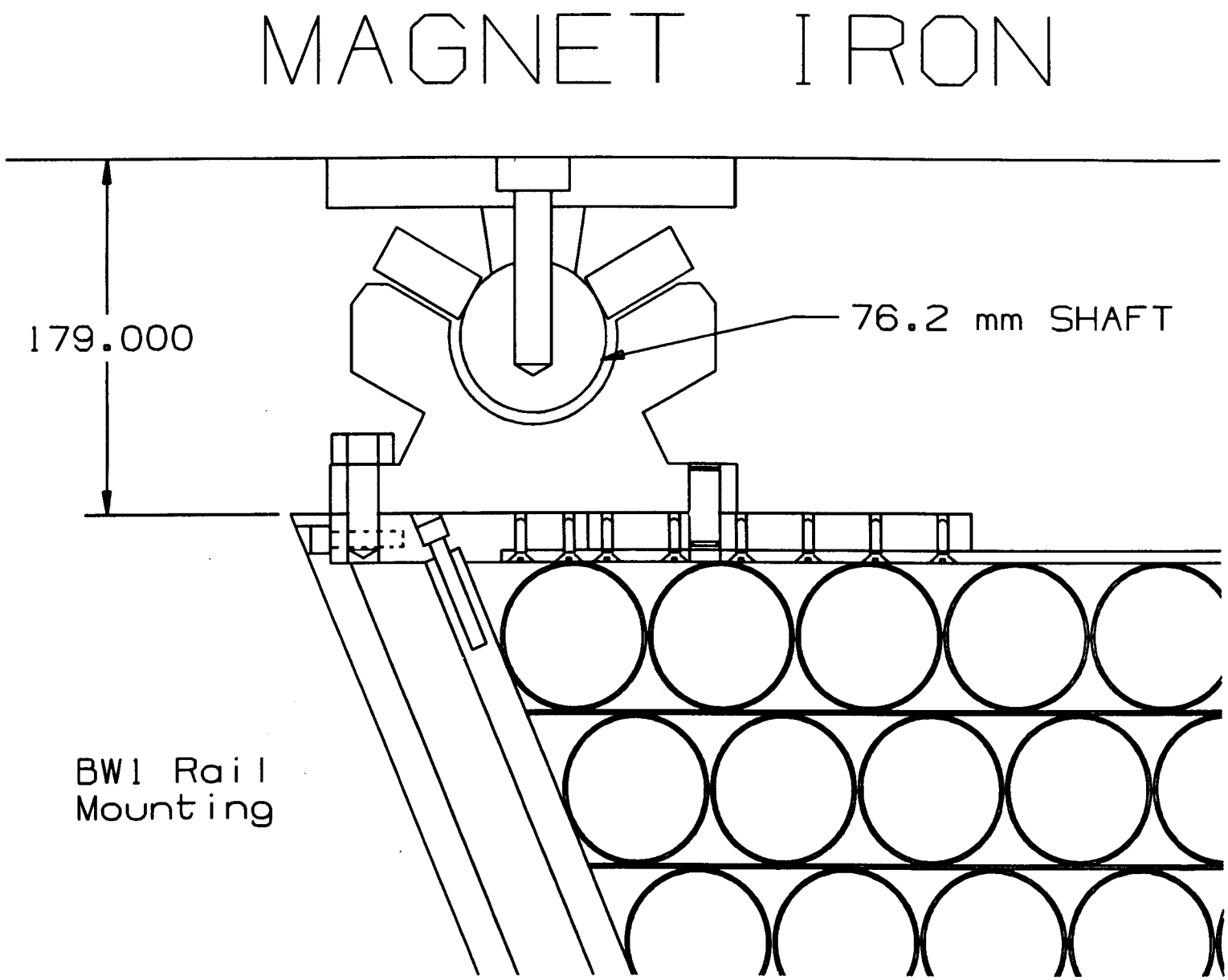

Figure 2.24. BW1 rail mounting.

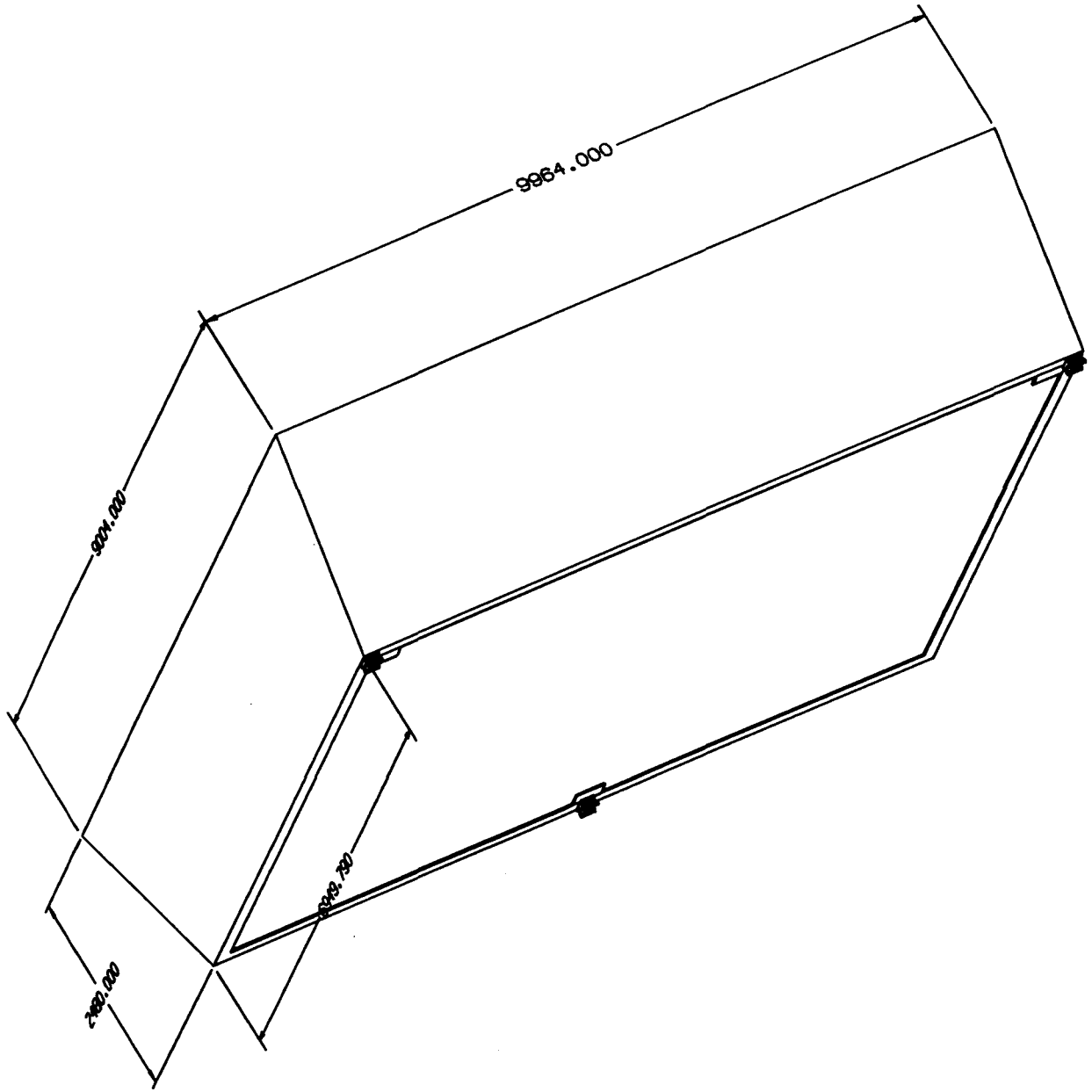

Figure 2.25. 3 point kinematic support for BW2/BW3 units.

3.0 STRUCTURAL ANALYSIS OF DETECTOR MODULES

The major questions to be answered by Finite Element Analysis (FEA) of this module design are:

1. What magnitude of overall module deflection is seen for each of the modules in the three layers of the detector (BW1, BW2 and BW3)? How is this affected by support locations and the number of layers of tubes in the modules?
2. What values of shear stress are encountered in the adhesive bonding between the tubes and the plates?

The second of these questions requires a detailed model of the tube and plate structure. It is not realistic to use such a detailed model of the whole module to find overall deflections. As each module is a very large flat plate in overall shape, it is reasonable to model a module as a flat shell with the rim of the module modeled separately. One first has to come up with equivalent properties for this shell so it models the real structure of tubes and plates. This process is described below for BW1 (4 θ layers, 4 ϕ layers), BW2 (4 θ layers) and BW3 (4 θ layers, 4 ϕ layers and 2 stereo layers). The FEA modelling techniques used here also will be used in conjunction with a mechanical prototype. This will consist of a 9 m long section of tube and plate structure with a cross section as shown in Figure 3.1. The tubes are all 76.2 mm diameter with a wall thickness of 1.59 mm. The intermediate plates are 1.59 mm thick and the top and bottom plates are 6.35 mm thick. All tubes are completely functional and are mounted to sections of precision end plate as described in Section 2 above. Aluminum is used throughout. Deflections and strain gauge measurements made on the prototype will be compared with a detailed FEA model.

3.1 Determination of Equivalent Shell Properties

The tube/plate structure in each of the modules is modelled using an 8-noded, quadrilateral shell element (STIF 93) in Ansys® The element properties needed are the elastic moduli (EX, EY) and shear moduli (GXZ, GYZ) in two orthogonal directions, the shell thickness and the material density. These properties must be selected so the equivalent shell has the same bending and shear stiffness in these two directions as the real structure. The weight/unit area also must match. The first step in this process is to analyze the end deflection of a cantilever beam consisting of a slice taken from the real structure in either the θ or ϕ direction. Because the layers of tubes lying normal to this slice do not transmit shear stress well, we must include the deflection due to shear in the analysis. The end deflection v_{max} of a cantilever is then given by:

$$v_{max} = \frac{wL4}{8EI} + \frac{wL2}{2GA}$$

w is the load/unit length and in this case is the weight/unit length.

First, a 2-dimensional analysis of the 8-layer beam model is done using Ansys®. A typical result is shown in Figure 3.2. The top 4 layers consist of tubes perpendicular to the beam axis. The tubes are connected to the interleaved plates and to each other at the tangent points. The connections between the tubes and the plates are modelled with adhesive elements as shown in Figure 3.3. The bottom 4 layers consist of elements of varying thickness to model the plates and the tubes. Those elements modeling each longitudinal tube have the same total cross sectional area as the tube and approximately the same moment of inertia. The overall effect is to model the actual longitudinal tube/plate structure within 1% (confirmed by separate analysis). In classical beam deflection analysis, shear deflection is usually ignored as it is always much smaller than the bending deflection. However, for this 8-layer structure, the layers of transverse tubes have a limited capacity to transmit shear stress as can readily be seen in Figure 3.2 by examining the deflected shapes of the circular tubes. Values of v_{max} are found for 2

values of the length L of the cantilever. As w is known, the values of EI and GA can then be found. For unit thickness of a solid equivalent shell of depth t, the values of EI and GA are:

$$(EI)_x = (EX)t^3/12 \quad \text{and} \quad (GA)_x = (GXZ)t$$

$$(EI)_y = (EY)t^3/12 \quad \text{and} \quad (GA)_y = (GYZ)t$$

where x and y are the two orthogonal directions. Values of EX, EY, GXZ, GYZ and t are then chosen to satisfy these equations. A value of density is then chosen to give the same weight/unit area. Note that for the 8 layer structure used in BW1, the moduli in the X and Y direction have the same values. This process is repeated for the tube/plate structures in BW2 and BW3. In both cases we have different properties in the X and Y directions. For example, Figures 3.4 and 3.5 show Ansys models of the 10 layer BW3 structure. Figure 3.4 shows a cross section normal to the f tubes. For analysis purposes, the stereo tubes are assumed to be parallel to the q tubes (they are actually at a 7.5° angle). Figure 3.5 shows similar results for the section normal to the q tubes.

3.2 FEA Shell Model of a Module

In this design, at any given layer (BW1, 2, 3), each face of the octagonal detector surface is made up of 3 modules. The maximum length of any given module is assumed to be one third of the axial length of the BW3 module, i.e. 9964 mm. The width is, of course different for each module. The dimensions used in the analysis described below are taken from the 11/25/91 configuration of the detector.

Figure 3.6 shows a model of the longest 8-layer BW1 module. Because of symmetry, it is only necessary to model one quadrant of the module. The tube/plate structure is modeled by equivalent shell elements as described above. The side and end plates of the module are modeled by 19 mm shell elements. The top and bottom rails and the outer plates are also included as shown in close up in Figure 3.7. This module is in the top position in the barrel and is thus the worst loading case. Various support conditions are analyzed to determine the optimum position for the support points. At present, these are assumed to lie along the long edges of the module. Depending on the final configuration of the magnet and its coils, the support points may be moved in from the edges. This will decrease the values of deflection given below. Figure 3.8 shows that with the supports at points 20% of the length of the long edge in from the corners, the maximum out of plane deflection is 0.457 mm, a very acceptable value. With this support condition, the only type of magnet deformation that can produce stresses in the BW1 modules is a twisting of the octant surface. Analysis of the above model for this case shows that an out of plane deflection of 1 mm at one support (with respect to the plane defined by the other 3 supports) requires a force of only 300 kg.

Similar models are also analyzed for the BW2 and BW3 modules. These modules are assembled as single structures consisting of a BW2 and a BW3 rigidly connected by plates. An initial analysis is done by modeling the BW2 and BW3 modules separately using supports all around the periphery. This gives the deflection of the modules with respect to the supporting structure. The maximum out of plane deflections are found to be:

BW2 – 0.796 mm
BW3 – 1.308 mm

It is interesting to note that the much thicker BW3 module gives a greater deflection. This shows very clearly that additional stiffness gained from the greater thickness is more than offset by the increase in weight.

The overall BW2/BW3 assembly is modelled by connecting the separate modules by 19 mm thick flat plate elements. The result is shown in Figure 3.9 for the whole structure supported at 4 points at the

The overall BW2/BW3 assembly is modelled by connecting the separate modules by 19 mm thick flat plate elements. The result is shown in Figure 3.9 for the whole structure supported at 4 points at the 20% points on the long edges. The maximum deflection of the assembly is 1.423 mm and occurs at the center of the BW3 module. Note that this represents a very small increase over that for the BW3 module resting on a completely rigid support. The whole assembly thus has a very stiff periphery and will thus be insensitive to the number and location of its supports. A further model was analyzed with a 19 mm thick plate used as a web running across the structure at its mid point and between the 2 modules. Figure 3.10 shows that this simple addition reduces the deflection to 0.689 mm.

3.3 Shear Stresses in the Adhesive Joints

To investigate this in more detail, a test specimen was built from 3 in. tube and 0.0625 in. plates similar to those to be used in the modules. This specimen (shown in Figure 3.11) consists of 2 layers of tubes sandwiched with 3 layers of plates and can be loaded in tension as shown so the center plate applies a shear load to the tubes. The deflection of the center plate relative to the outer plates is measured with a LVDT displacement transducer and strains at various points of interest are measured with strain gauges. A finite element model of the specimen was also run using Ansys. Tests and analysis are done both with epoxy adhesive only at the tube/plate joints and also with the glue used at the tube to tube joints. For the case with glue at the tube to tube joints the center plate deflection is 0.00309 in. by analysis and 0.00343 in. experimentally, using a 50 lb axial load in both cases. The shear stiffness for this geometry is greater by a factor of 6 than that for glue used only at the tube/plate joints. The FEA model includes elements for the adhesive so estimates of the stresses in the adhesive can be made. When the specimen was loaded to failure, the adhesive bonds remained intact. Failure occurred through the adhesive at an applied load of 1373 lb when Ciba-Geigy 1526 epoxy was used. At this load, the Ansys model showed that the maximum tensile stress in the aluminum was 28500 psi, close to the yield strength (34000 psi) of the metal. The analysis also indicated a shear stress of 2550 psi in the epoxy at the failure load. The manufacturer gives a value of 3000 psi for this material. One obvious artifact which could be responsible for the difference was that one of the strain gauges was partly under the glue line and, as the gauge was covered with a polyurethane protective coating, this causes a high local stress concentration. Strain measurements made at points on the tubes close to the adhesive connections are about 25% lower than values found from FEA. This result is expected as the gauges measure the average stress over their active area (0.125 x 0.125 in.^{2} in this case) and are located in an area with very high stress gradients. These results can be used to estimate actual stresses in the adhesive in other structures such as our prototype and even complete modules. Because the local geometry at the tube/plate junction is identical to that found in the actual modules, we can use the results of FEA of a section of module to estimate the overall failure load for the module. Experimental strain readings taken on such a structure will be used to calculate the stresses in the tube wall at points close to the adhesive. It is assumed that the stress in the adhesive is proportional to the stress in the adjacent tube wall. The stress in the adhesive at failure can thus be found by extrapolation from the FEA results. Using the equivalent shell FEA model for the whole module, bending moments and shear forces can be found at any point on the module and then used as boundary conditions to a detailed FEA model of a small section of the tube/plate structure. The adhesive stresses found in this way can then be compared with the adhesive failure stress found from the above test.

3.4 Discussion

The deflection results are summarized in Table 3.1.

TABLE 3.1. BW1 AND BW2/3 MODULE DEFLECTIONS.

MODULE OR ASSEMBLY	MAX DEFLECTION (mm)
BW1, 4 point support at 20% points	0.46
BW2/3, 4 point support at 20% points	1.42
BW2/3, 4 point support at 20% points and with central web	0.69

The most important result is that an 8-layer BW1 module is practical. The module is supported at 4-points on the long edges and at points located approximately 20% of the module length in from the corners. The exact distance will be determined once the final module configuration is known. A pure kinematic, 3-point support is not practical for this module. However, though the deflection of the BW1 module can be kept very small, the module is actually quite flexible in the twisting mode. This means that the module will not be affected by any likely deflection of the magnet toroid. The results for the BW2/3 assembly give a somewhat high deflection. However, the largest deflections occur at the middle of the module, well away from the critical end plates in the modules, and thus have no effect on the precision with which the anode wire ends are located. The limiting factor here is how far the anode deviates from a point mid way between the field shaping electrodes. As the wires also sag by approximately 1.2 mm along their length, the differential motion will to some extent be compensated.

The other important result of the analysis is that we must put adhesive between the tubes as well as between the tubes and plates to maximize the shear stiffness of the modules.

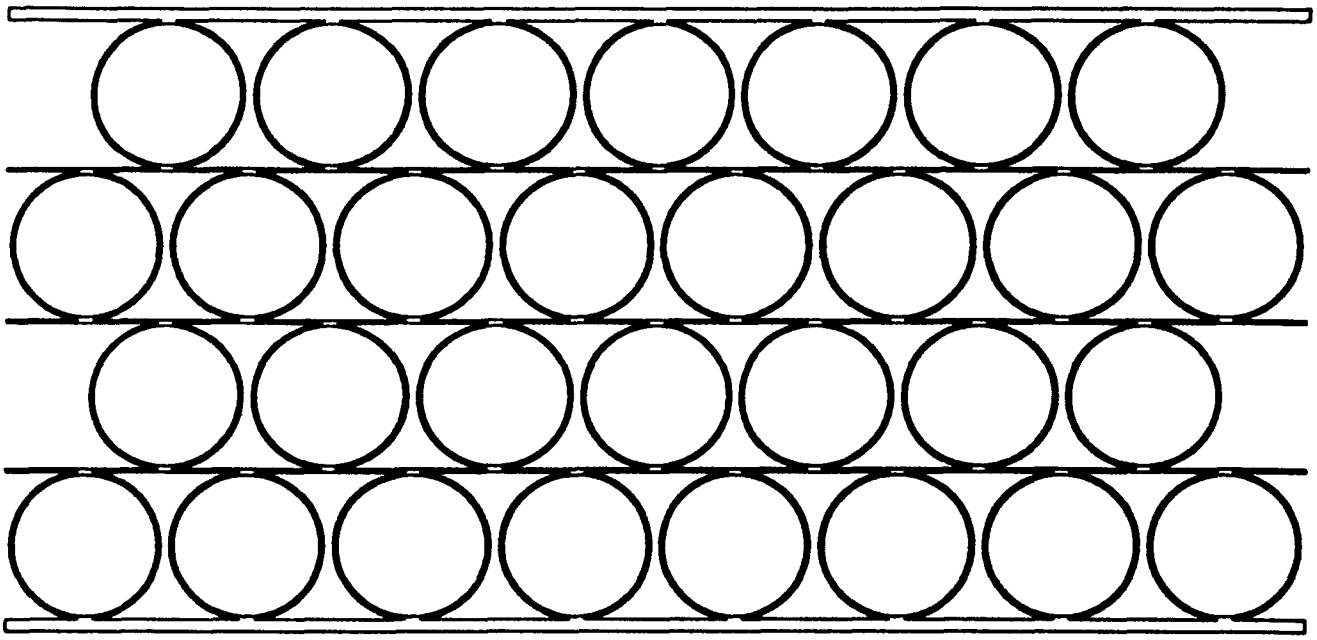

Figure 3.1. Cross-section of a 4-layer prototype. All tubes are 1.59 mm wall thickness and 72.6 mm outside diameter. The top and bottom plates are 6.35 mm thick and the intermediate plates are 1.59 mm thick.

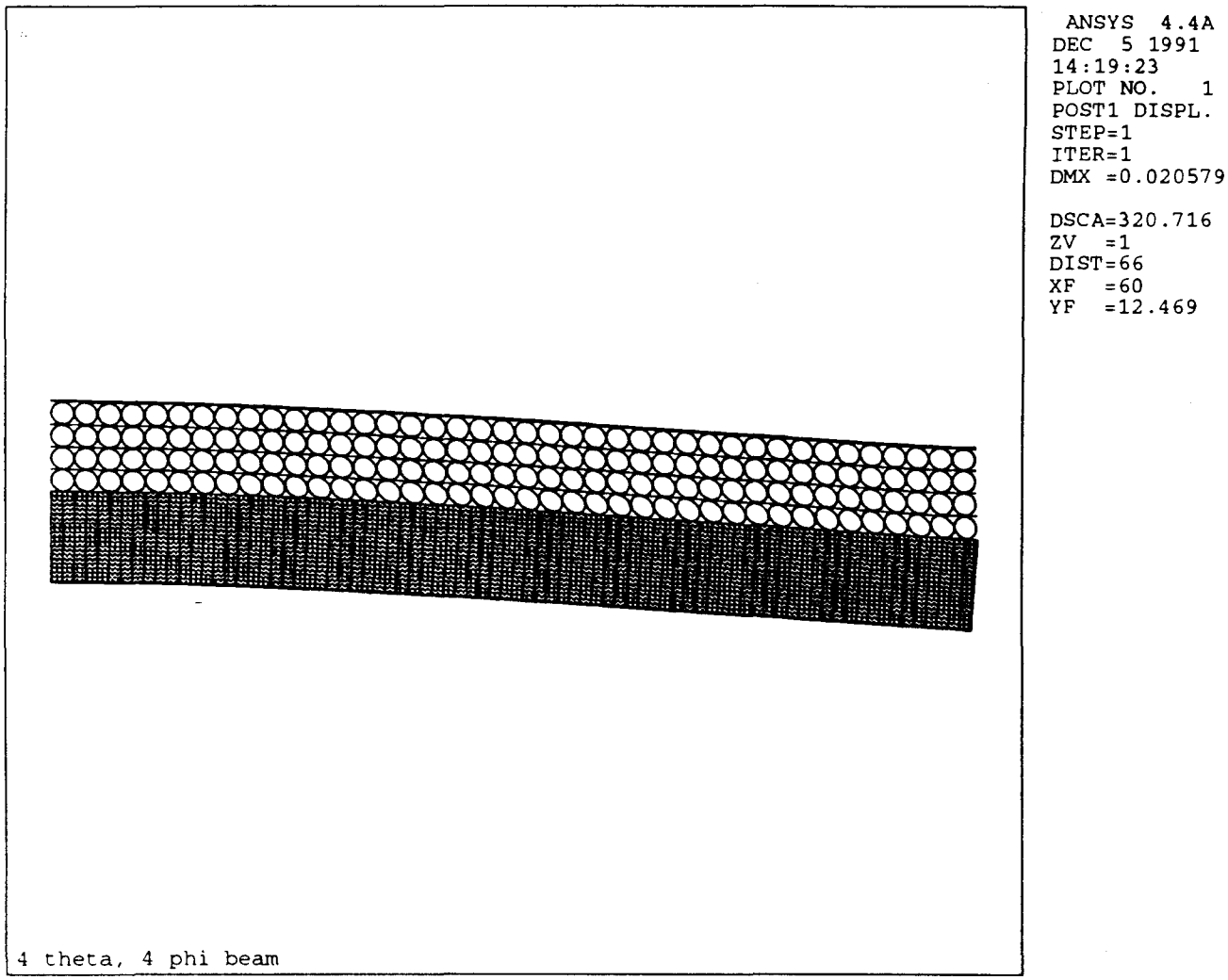

Figure 3.2. Finite element analysis of 8-layer beam model.

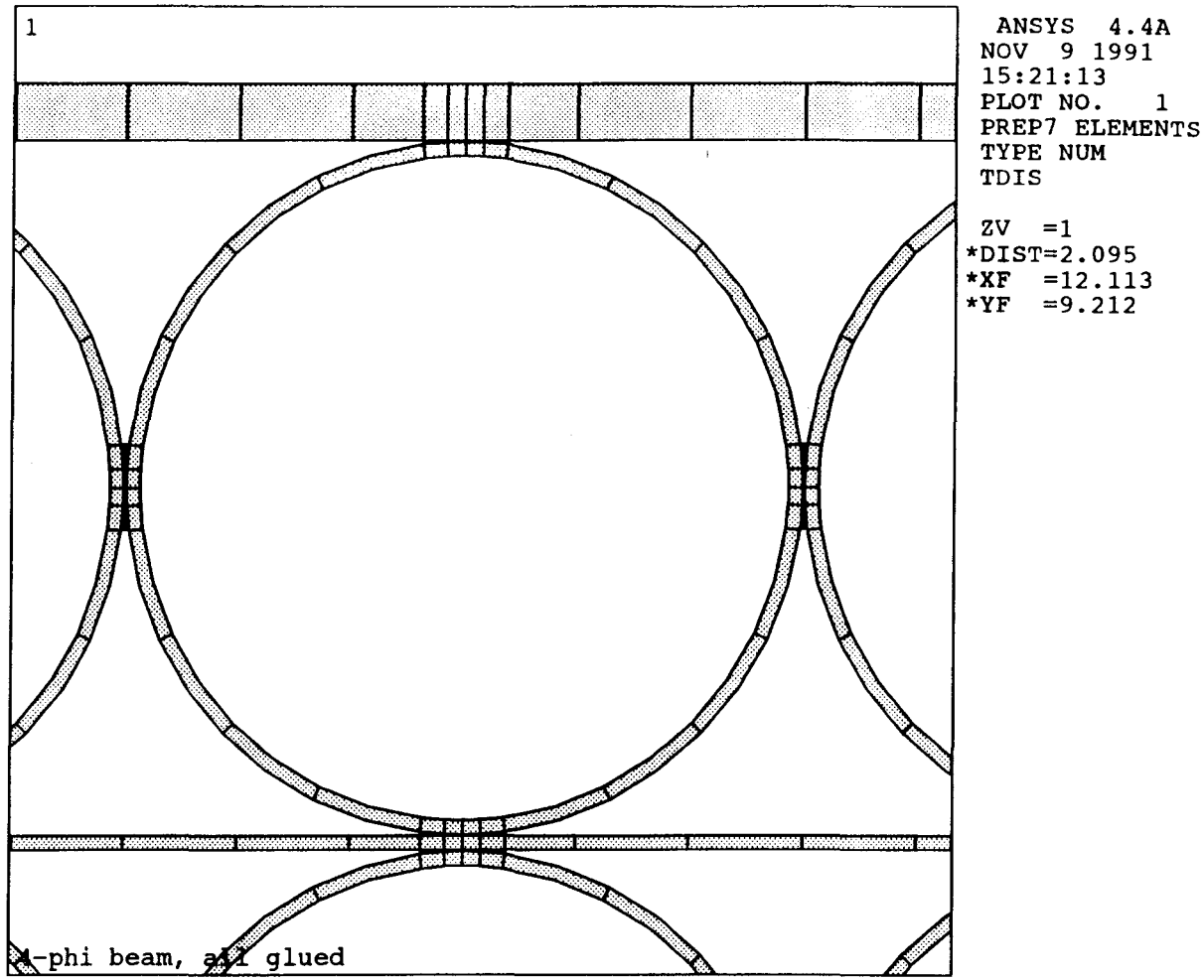

Figure 3.3. Close up of beam model showing elements in tubes, plates and the adhesive joints between the tubes and between the tubes and plates.

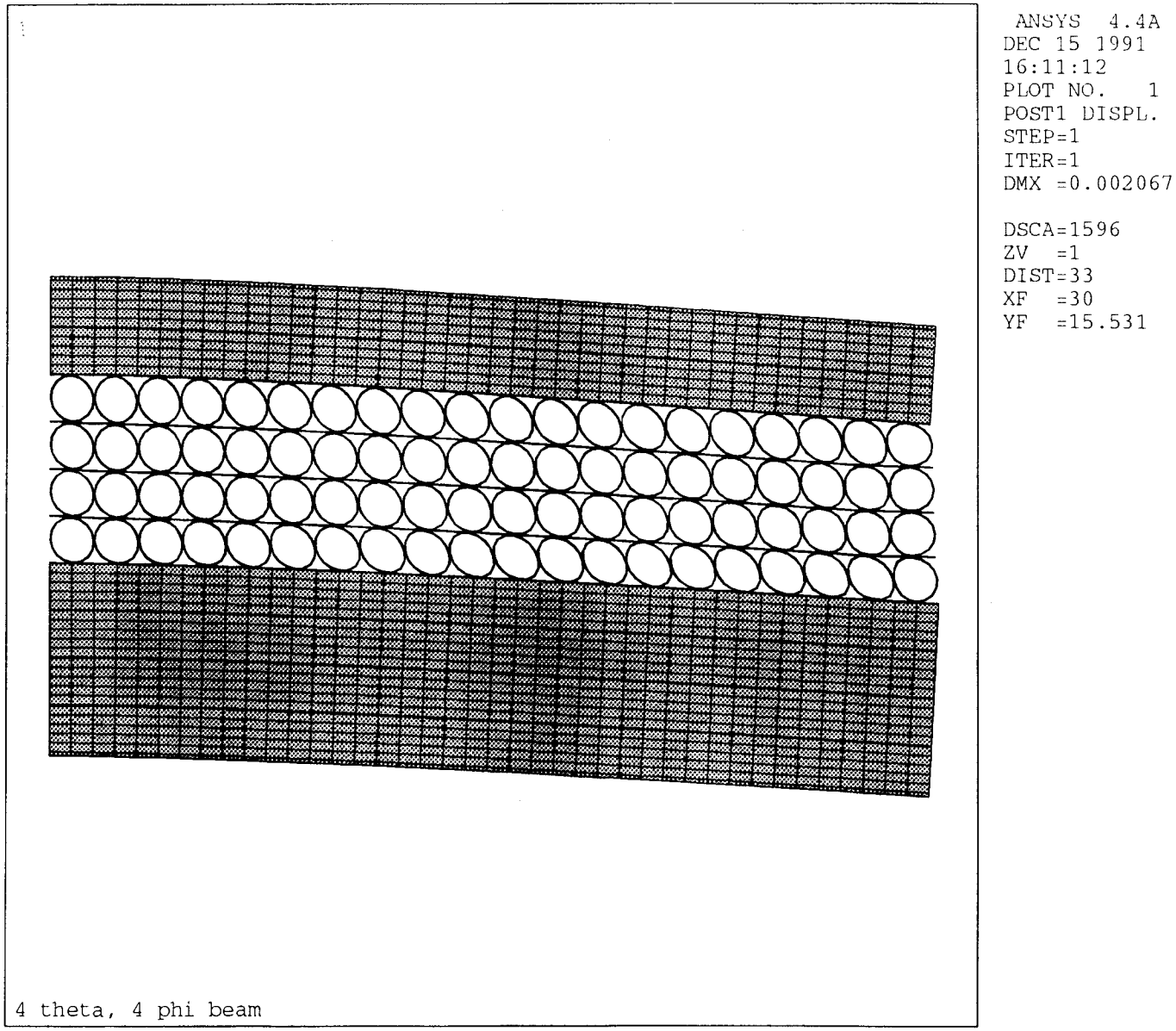

Figure 3.4. ANSYS model of the 10-layer BW3 structure.

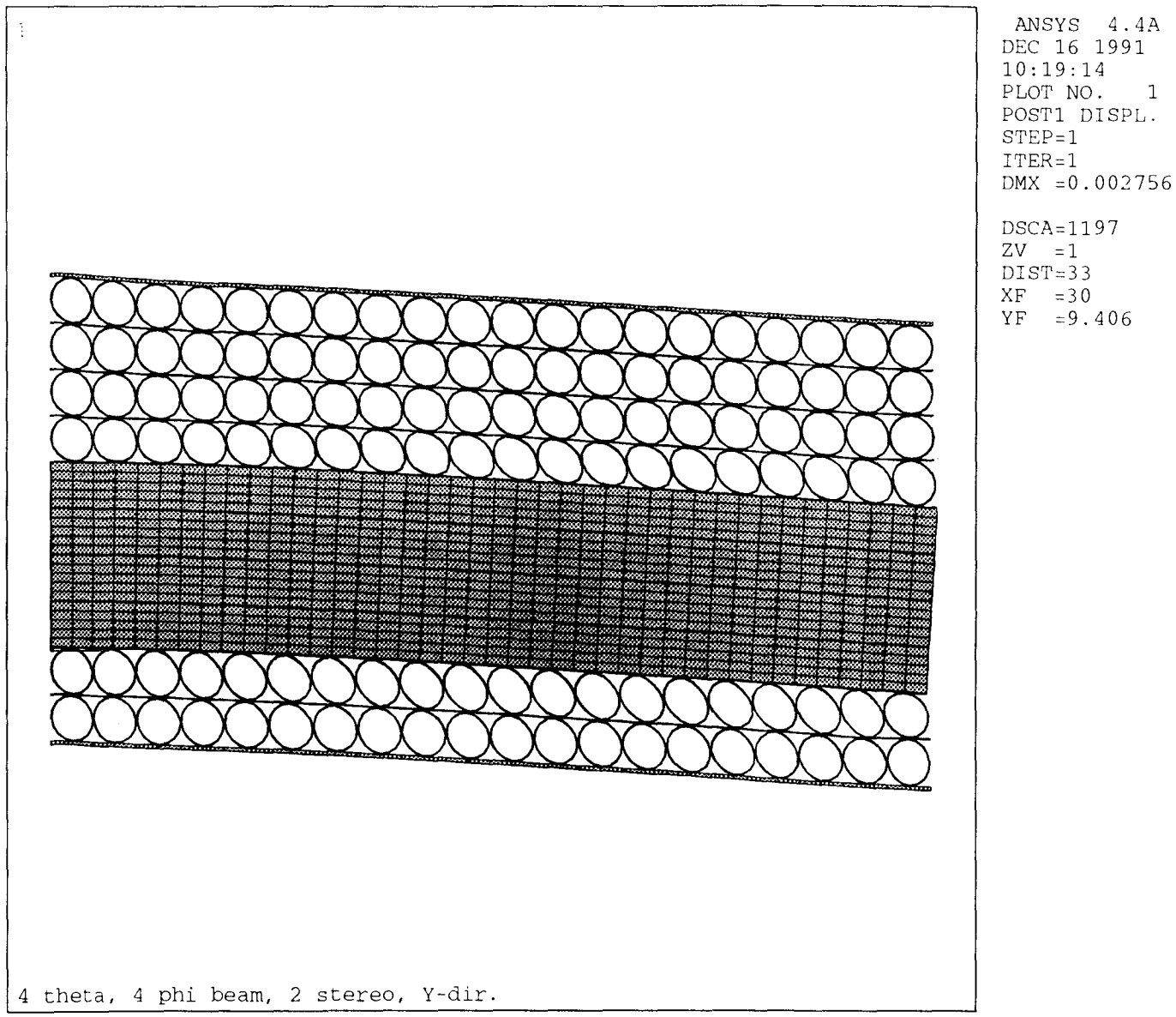

Figure 3.5. ANSYS model of 10-layer BW3 structure.

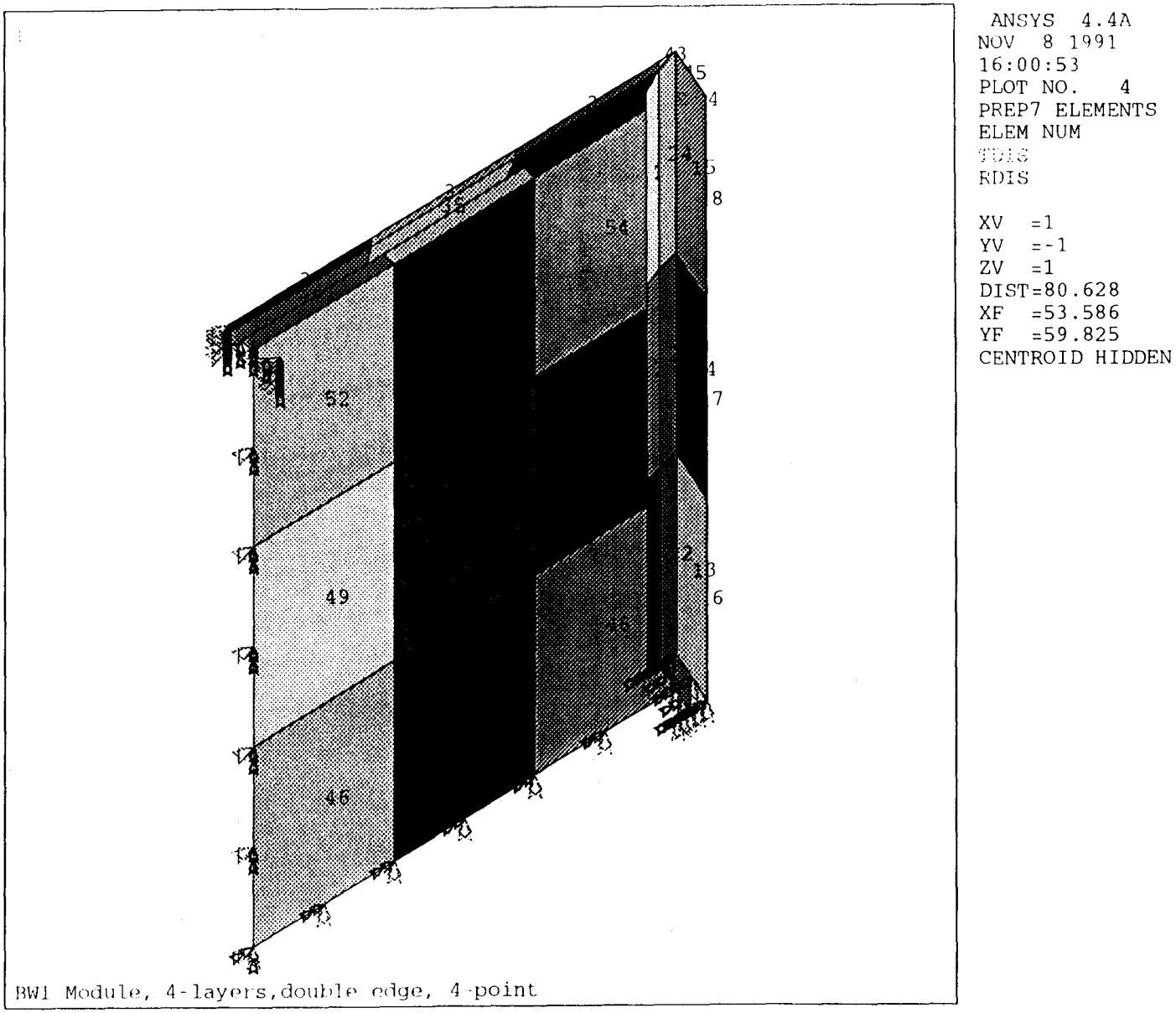

Figure 3.6. Finite element model of one quadrant of a BW1 module. The tube and plate assembly is modeled by an equivalent orthotropic shell.

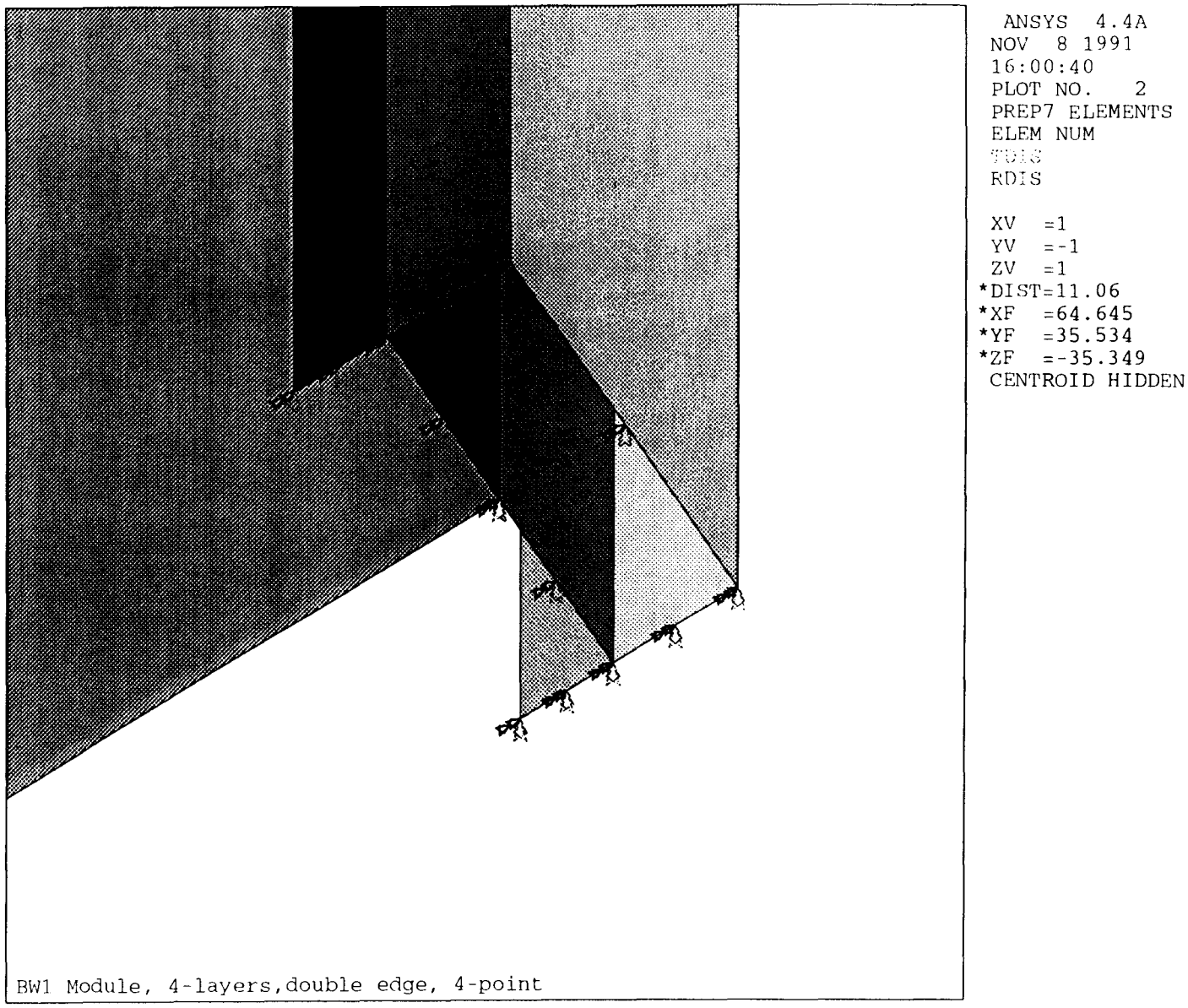

Figure 3.7. Close up of edge of FEA model of BW1 module showing modelling of the peripheral structure elements.

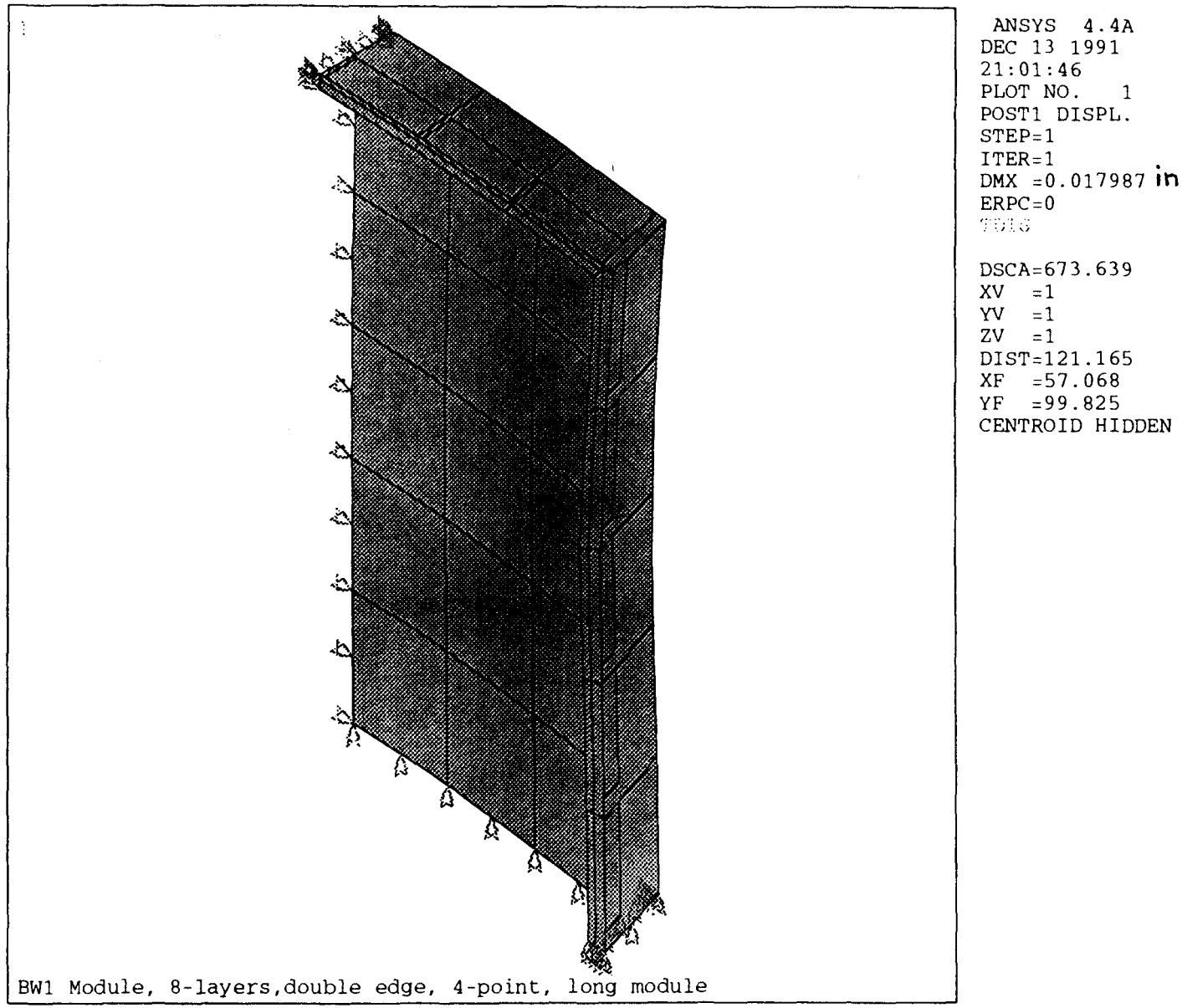

Figure 3.8. Deflection results for the BW1 module. The support is 20% of the way along the long edge of the module.

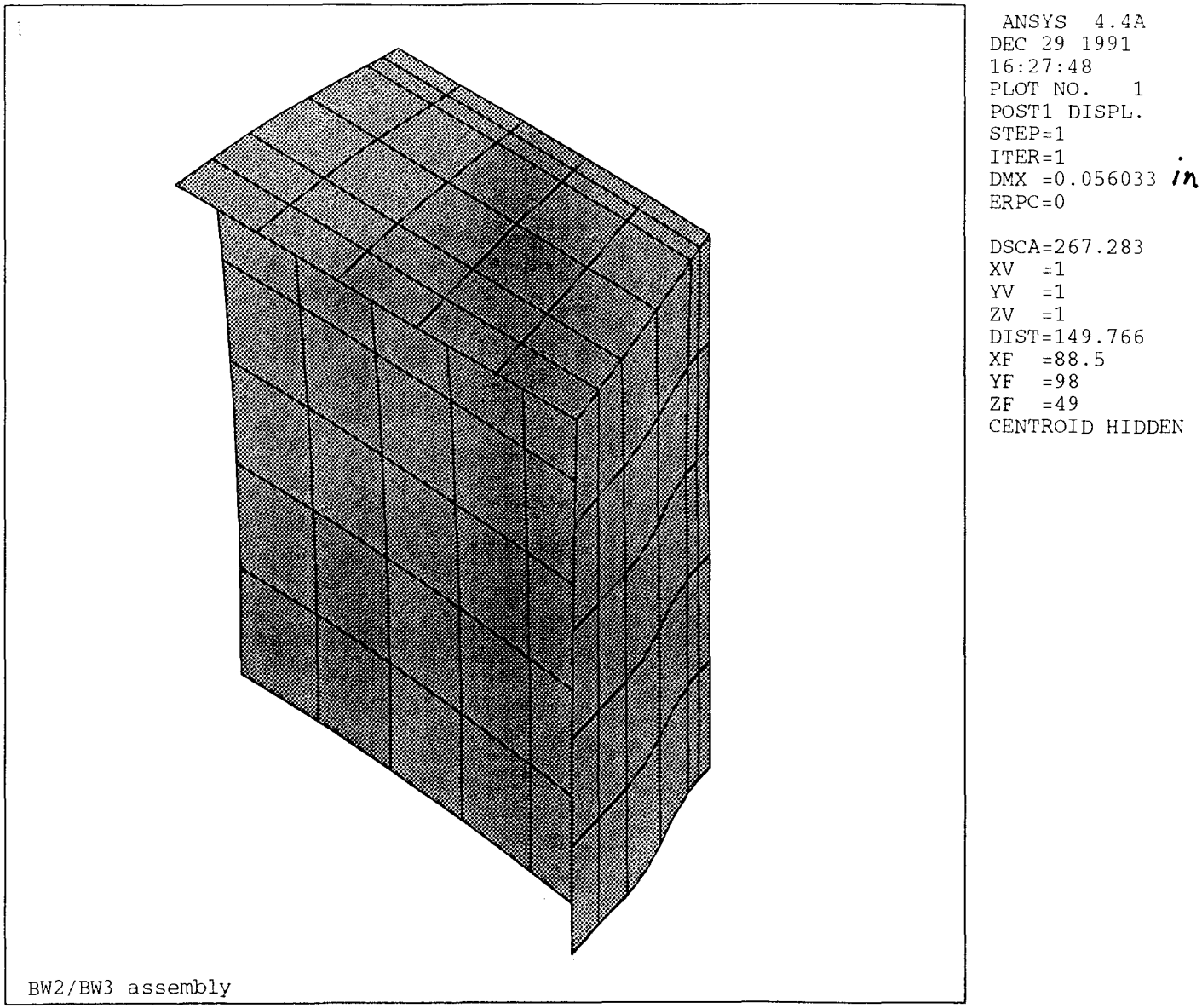

Figure 3.9. Deflection results for the BW2/BW3 assembly supported at four points at 20% points on the long edges.

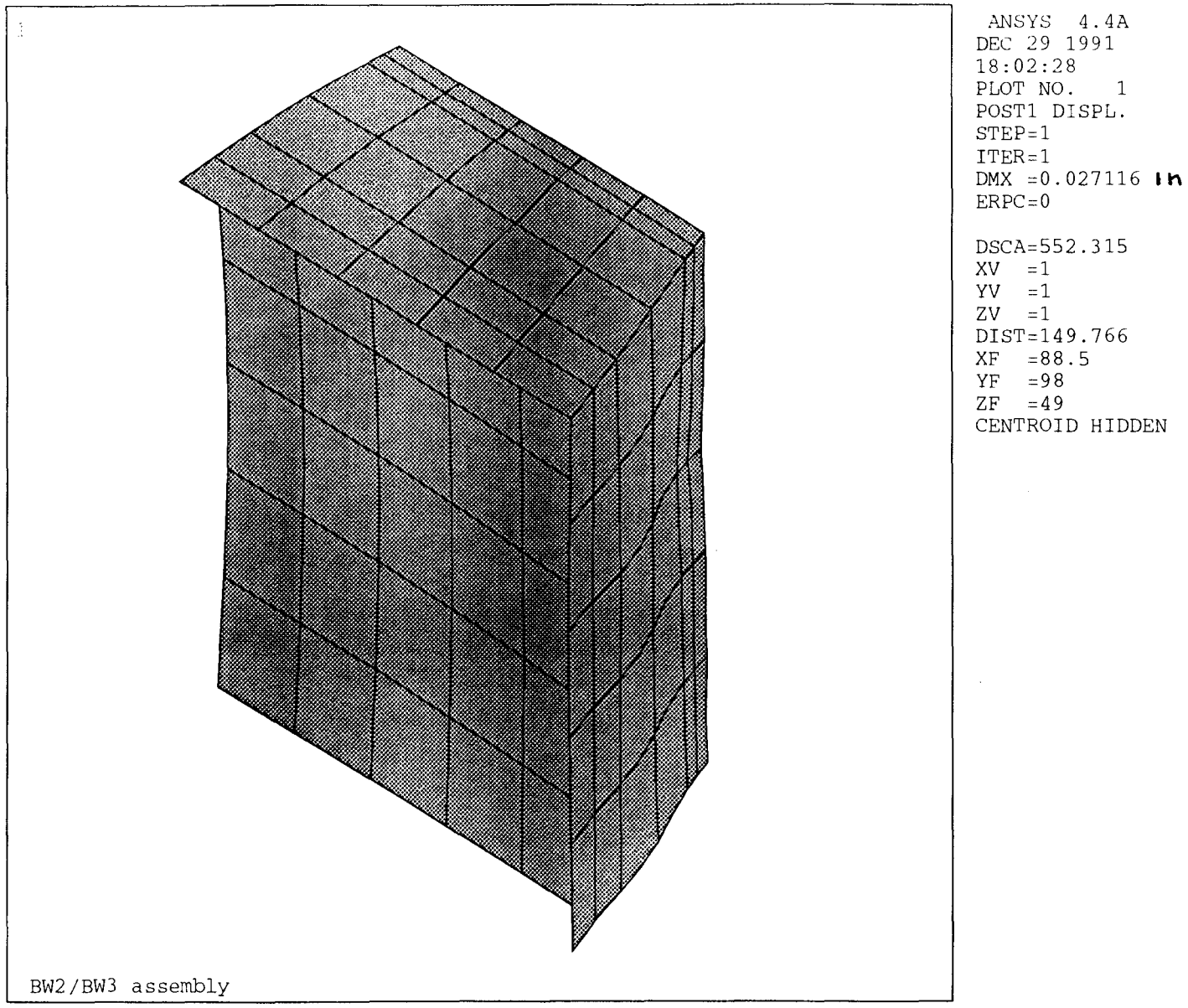

Figure 3.10. Deflection results for BW2/BW3 assembly with a web across midpoint.

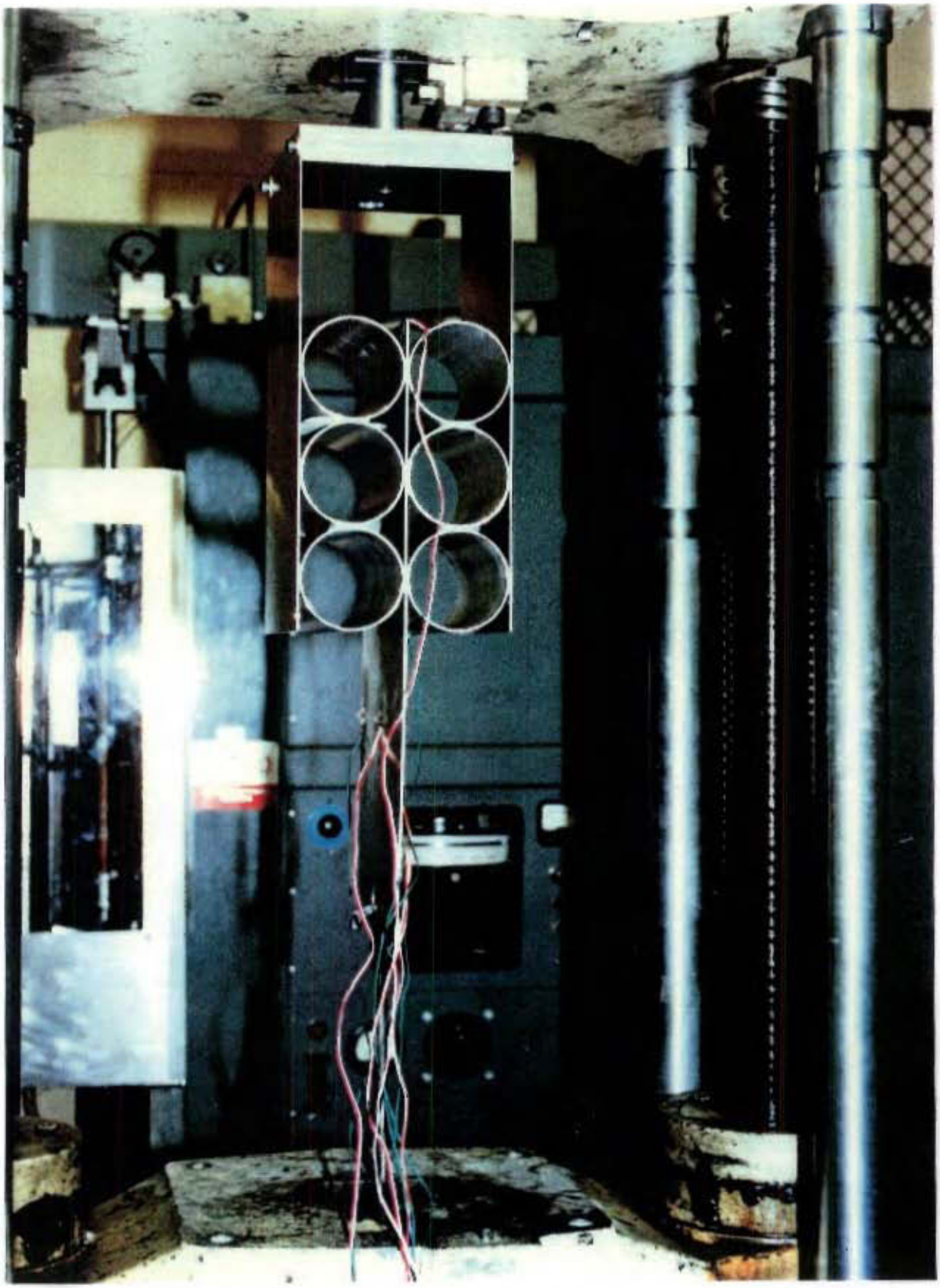

Figure 3.11. Test specimen in tensile testing machine.

4.0 DRIFT CELL DESIGNS

Our drift cell design is based on 75 mm diameter cylindrical aluminium tubes. We have two options: simple drift tube without field shaping and drift tubes with field shaping electrodes. The drift cell designs and justifications of the designs are discussed in this section.

4.1 Simple Drift Tube

The first option is simple tubes without additional field shaping electrodes. A simple drift tube has an anode wire at the center of a conductive tube. It requires only a positive high voltage. The tube design parameters are given in the table below.

TABLE 4.1. DESIGN PARAMETERS – NO FIELD SHAPING.

TUBE SHAPE	ROUND
Inside radius	3.6 cm
Wall thickness	1.6 mm
Wire diameter	153 μm
Wire material	Gold plated tungsten
Wire tension	3 kg
Gas mixture	P10 or Ar-CH_4-CO_2 (90-5-5)
High voltage	+3.6 kV
Gas gain	~10^5
Resolution	TBD

Figure 4.1 shows the high voltage and signal connections. The high voltage is fed in from the left and the signal output from the right. The anode wire is terminated at the high voltage end by a 360 Ω resistor.

We choose round tubes because unlike the square or rectangular tubes, the electric field inside a cylindrical tube is completely symmetric around the anode. The position measurement, therefore, does not depend on the track angle. The formation of a local vector from hits in drift cells of different layers is straightforward as illustrated in Figure 4.2.

The resolution and operating conditions of simple drift tubes are mainly determined by the following factors:

- tube inside dimension
- anode wire size
- wire sag and tube deformation
- gas mixture
- proportional mode or streamer mode.

These factors are discussed in the following sections.

4.1.1 Tube Size and Gas Mixtures

The lower limit of the tube size is mainly determined by economic considerations. The total number of tubes is about 70,000 in the central and intermediate regions based on 75 mm diameter tubes. We feel this is an acceptable number. The upper limit of the tube size is determined by tube performance

factors, mainly the desired resolution. The bigger the tube, the more difficult it is to obtain good resolution. We will discuss this problem in more detail later.

Simple drift tubes are commonly used as tracking devices for large muon detectors. Conventionally, the tube cross section is small, ranging from 0.9 cm (ZEUS)[1] to 3 cm (D0 forward muon system).[2] Such tubes are normally operated in the streamer mode.One inch square streamer tubes are the most popular for muon chambers. Using standard C_4H_{10} based streamer-mode gas, a MIT group (member of GEM) recently obtained 60 μm resolution in beam tests with 1-in. square drift tubes. This is perhaps the best resolution achieved with this kind of tube operating at one atmosphere pressure.

Simple drift tubes with diameters as large as 4 in. have been used as muon tracking devices in the past.[3,4] However, high resolution was not the primary goal for these systems. The SDC muon group has never considered the option of small cross section drift tubes mainly because the large number of tubes required. Instead, we choose a relatively large tube diameter of 75 mm. In order to achieve the desired position resolution, many factors have to be carefully considered when using simple drift tubes of such size.

The most important factor affecting the performance of large diameter tubes is the electric field distribution inside the tube which is given by

$$E_r = \frac{V}{r ln(b/a)}$$

where V is the voltage applied to the anode, r is the distance to the center of the tube, a is the anode radius and b is the cathode inner radius.

The electric field as a function of distance from the anode wire is plotted in Figure 4.3 for three different anode wire diameters, 50 μm, 100 μm and 150 μm. The high voltage values are determined by requiring that the gas amplification factors (in proportional mode) be the same for the three cases. These high voltage settings are valid for all four gas mixtures discussed in the next section.

The most serious problem encountered in operating large cross section, simple drift tubes is that the drift field varies as 1/r and has low value over most of the drift volume. Large diameter anode wire can help improve this situation. But even for a 150 μm anode wire, the drift field at the wall is still only about 160 V/cm, far below the saturation level for conventional drift chamber gases. The issue of choosing gas mixtures will be discussed later in more detail.

For the simple drift tube option, we will use 150 μm diameter anode wire. We have studied effects of anode wire diameters on tube operation. Results of our study are summarized in Reference 5. Our conclusion is that 150 μm anode wire can be used for proportional drift tubes.

Another factor limiting the size of the tube is electron diffusion. In Figure 4.4, the diffusion coefficient of Ar-CO_2 (80:20%) mixture is given as an example. The diffusion coefficient is given approximately by 200 μm$\sqrt{x}$. The average drift distance in our drift tube is about 2 cm. The diffusion for a single electron is about 300 μm on average. If the discriminator threshold is set to 4 primary electrons, then diffusion limits our resolution to ~150 μm.

Choosing a correct gas mixture is essential for successful drift chamber operation. Let us consider the following gas mixtures: Ar-CO_2 (90:10%), Ar-CH_4 (90:10%), Ar-CO_2-CH_4 (90:5:5%) and Ar-CH_4-CF_4 (90:5:5%). We limit the quenching components to less than 10% to ensure that the mixture is nonflammable. Further reducing the quenching component may result in unstable operating conditions.

In general, parameters affecting resolution of drift chambers are

- electric field and its uniformity,
- pressure and temperature dependence of drift velocity,
- sensitivity of drift velocity to pollutants,
- sensitivity of drift velocity to gas mixing ratio,
- electron diffusion,
- time measurement errors,
- wire location precision.

Figure 4.5 shows the drift velocity as a function of electric field for these four gas mixtures. These curves are measured by our Seattle group. Based on these measurements, the maximum drift time can be easily calculated. Results of these calculations for our drift tube (3.7 cm drift) are listed in Table 4.2.

TABLE 4.2. MAXIMUM DRIFT FOR DIFFERENT GAS MIXTURES.

GAS MIXTURE	MAXIMUM DRIFT TIME (μs)	COMMENTS
Ar-CO_2 (90:10%)	1.44	too slow
Ar-CH_4 (90:10%)	0.92	acceptable
Ar-CH_4- CO_2 (90:5:5%)	1.03	may be acceptable
Ar-CH_4-CF_4 (90:5:5%)	0.56	very fast

In order that the maximum drift time not be too long, the gas mixture must be sufficiently fast at low drift field. Obviously, Ar-CO_2 (90:10%) does not satisfy this requirement. P10, a commonly used gas for this kind of tubes, gives a maximum drift time of 920 ns. The maximum drift time in Ar-CH_4-CO_2 (90-5-5%) mixture is 1.03 μs. Another extremely fast gas, Ar-CH_4-CF_4 (90-5-5%), has the shortest maximum drift time of 560 ns.

Figure 4.6 shows the computed x-t correlation curves for a drift tube with 7.3 cm inside dimension and a 153 μm diameter wire. The x-t correlation curves are nonlinear in these cases. Among the four gases, P10 and Ar-CO_2-CH_4 (90:5:5%) appear to be acceptable.

The nonlinear x-t relation does not affect the trigger threshold curve significantly. In Figure 4.7 and Figure 4.8, muon trigger efficiencies as functions of P_t are given for a standard trigger configuration. In Figure 4.7, the trigger threshold curve is computed by assuming a linear x-t relation. The curve in Figure 4.8 is based on the x-t relation given in Figure 4.6(b). The difference between these two figures is small. However, the nonlinear relation will strongly affect the chamber resolution. In principle, the x-t correlation curve can be measured and corrected for in offline analysis. The achievable resolution is determined mainly by how well we know this x-t relation and how stable the x-t relation is.

In order to reach optimum position resolution, the following factors have to be studied and monitored.

- Temperature dependence of drift velocity. In Figure 4.9, this dependence is given for P10 gas. This effect can be quite large if the temperature of the muon tracking chambers is not well controlled.
- The variation of gas pressure will be an important factor because the drift velocity depends on the ratio of electric field to the gas pressure inside the tubes. If the gas exhaust goes directly into the atmosphere, the pressure inside the tube will vary by

several percent depending upon the weather. This change may be difficult to monitor. A natural solution is to operate the chamber at fixed pressure or even permanently sealed. (Permanently sealed, pressurized aluminum tubes have been used by the HRS group and have now been proposed as one of the options for the GEM muon detector.)

4.1.2 Wire Sag and Tube Deformation

As discussed before, a key feature of our design is that the anode wire is only supported at the two end caps. We do not have any additional wire support inside the drift tubes.

Extensive studies were made in Seattle over the last year to investigate the properties of different wire material, the wire sag and its effects on drift tube operation. Some of the results are summarized in Reference 6. If tensioned at 70% of the breaking strength, the wire sag of gold plated tungsten wire is about 1.3 mm in a 9 meter long tube. Additional deflection due to electrostatic forces is negligible compared to gravitational sag. Since the shape of the wire inside the tube is precisely known, the wire sag can be corrected in offline analysis. At the trigger level, the wire sag does not matter because the trigger is based on local information from wires in adjacent layers. Due to the deformation of the chamber module, the tube wall will deform. As discussed in previous sections, such deformation is also small.

Because the distance between the anode and the tube wall is large in our design, the change of charge density on the anode wire due to the wire sag and wall deformation is small. The change of charge density is only 0.05% if the anode is displaced from the tube center by 2 mm. The tube operation, therefore, will not be affected. This will not be the case if the tube cross section is small. An extreme case of small cross-section tubes is the ZEUS central muon drift tubes which have 0.9 cm × 0.9 cm cross-section and require wire supports every 45 cm.[7]

Long drift tubes without wire support have been used in high energy experiments. An example is the VENUS muon drift tubes which are 7.6 meters long. The cross-section of their tubes is 5 cm × 7 cm, and the anode wires (70 μm diameter) are tensioned to 400 grams. We have made two 9 meter long drift tubes in Seattle and no problems related to the unsupported anode wire have been observed.

4.1.3 Operation Mode

Drift tubes in our design are operated in the proportional mode. High gain preamplifers are required. If drift tubes can be operated in the streamer mode, the preamplifers are no longer necessary because the signal size is very large, typically 50 mV. Conventionally, C_4H_{10} or C_2H_6 is the major component of gas mixtures for drift tubes operating in streamer mode. Such gas mixtures are highly flammable and cannot be considered for SDC muon system. Our study has shown that it is impossible to operate drift tubes in streamer mode using the nonflammable gas mixtures listed in Table 2.[5] All nonflammable streamer mode gas mixtures people have discovered so far are not suitable for our application.

4.1.4 Double Track Resolution

The length of the track segments inside a simple drift tube varies from zero to the width of the tube. The total charge collected for each track varies correspondingly. This requires that amplifiers have large dynamic range in order to avoid saturation. The decay time of the signal is long due to the time required to collect all charge along muon tracks. Resolving two tracks is, therefore, difficult.

4.2 Cylindrical Tube With Simple Field Shaping

Many different field shaping schemes for muon drift chambers have been developed in the past. A detailed review of this subject is given in a SDC note.[8] We consider that simplicity is the key factor for the success of a system as large and as complex as the SDC muon system. Thus, we have chosen a very simple field shaping scheme.

4.2.1 Cell Design

The cross-section of our drift tube with field shaping electrodes is shown in Figure 4.10. The tube is a thin wall aluminium extrusion with two T-shaped channels to which the field shaping electrodes are attached. The field shaping electrodes are made of coextruded aluminium strip and plastic (Noryl). The electrodes are carefully designed to prevent high voltage break down. We choose round tubes because they can be easily rotated at different θ. Such rotation is necessary in order to avoid the resolution degradation at large θ which will occur if the drift field lines are not approximately perpendicular to the detected muon tracks.

TABLE 4.3. DESIGN PARAMETERS – DRIFT TUBE WITH FIELD SHAPING.

Inside radius	3.6 cm
Wall thickness	1.6 mm
Wire diameter	50 μm
Wire material	Gold plated tungsten
Wire tension	300 grams
Gas mixture	Ar-CO_2 (90-10)
High voltage	Anode at 5.0 kV, electrodes at 5.0 kV
Gas gain	10^5
Expected resolution	< 200 μm

Again, the lower limit of the tube size is determined by economic considerations. The upper limit of the tube size is determined by the maximum acceptable drift time and electron diffusion.

We have chosen 50 μm wire diameter for this option. The operational stability is slightly better for smaller diameter anode wires. Also, the high voltage required is lower. We can safely tension the 50 μm tungsten wire at 300 grams which is about 70% of its breaking strength. Such tension is sufficient to maintain the electrostatic stability of the wire. The wire sag in a 9 meter long tube is 1.3 mm which has to be considered in the offline track fitting process.

As discussed in the previous section, the tube operation is not affected if the anode is displaced from the geometric center of the tube by a few mm. However, we do have to maintain the separation of the two electrodes to within 1 mm in order not to change the tube gas gain by a large amount.

Figure 4.11 shows the high voltage and signal connections. The anode wire and field shaping electrodes are held at the same potential, +5 kV. Therefore, only one single positive high voltage power supply is needed. The drift tube is terminated at the high voltage end by a 360 Ω resistor. The low impedance signal path is provided by the capacitance between the electrodes and the aluminium wall which is several nF. We do not have the high voltage capacitor as we have in Figure 4.1 for the case of no field shaping.

4.2.2 Gas Mixture and Operating Conditions

The gas mixture we choose is argon 90% and CO_2 10%. The drift velocity as a function of electric field is given in Figure 4.5. Saturation starts at 750 V/cm and continues to higher field. The drift field lines and field uniformity are given in Figure 4.12 and Figure 4.13. The variation of the drift field within the range 0.5 cm to 3.2 cm is less than 10%. The variation of drift velocity over the entire tube is much less than 1%. The computed x-t correlation curve is given in Figure 4.14. The linearity of this x-t relation is very good. The maximum drift time is 770 ns. Since we operate the drift tube in the saturated mode, degradation of resolution due to environmental factors such as atmospheric pressure variation and temperature change is minimized.

The drift velocity of the 90:10% mixture is sensitive to the variation of CO_2 concentration. Such sensitivity can be reduce by increasing the CO_2 to >16%. Significantly higher voltage will be required in order to reach the drift velocity saturation plateau. We believe that it is not too difficult to control the gas mixing ratio for the Ar-CO_2 mixture. Therefore, we prefer not to increase the CO_2 concentration which will make the chamber design more difficult.

If shorter drift time is desired, we can use faster gas. In Figure 4.15, the measured drift velocity as a function of electric field and the x-t correlation curve is given for Ar-CF_4-CH_4 (80:10:10%). The maximum drift time is only 360 ns and the linearity of the x-t correlation curve is reasonably good. Another fast gas mixture proposed by the DO muon group is Ar-CF_4-CO_2 (90:8:2%). Its measured drift velocity as a function of electric field and the x-t correlation curve is given in Figure 4.16. The maximum drift time is 460 ns in this case.

4.2.3 Double Track Resolution

With only two electrodes, one above and one below the anode wire, the drift field can be shaped into a very narrow band 1 cm wide. The two track resolution for parallel tracks can be as good as a 2 mm which should provide enough rejection power for δ rays.

REFERENCES

1. F. Gasparini et al., "ZEUS Drift Tubes," NIM **A267** (1988) 87.
2. Y. Antipov et al., "D0 SAMUS," Fermilab Preprint 91, 217.
3. J. Allaby et al., "MAC Detector," NIM **A281** (1989) 291.
4. Y. Asano et al., "VENUS Drift Tubes," NIM **A259** (1987) 430.
5. T. Zhao, "Experiences with Short Drift Tubes," SDC-91-00116.
6. U. Bratzler et al., "The Properties of a 9.2 m Long Drift Tube," SDC Note.
7. ZEUS Design Report, 1987.
8. T. Zhao, "Tracking Muons at SSC," SDC-91-00003.

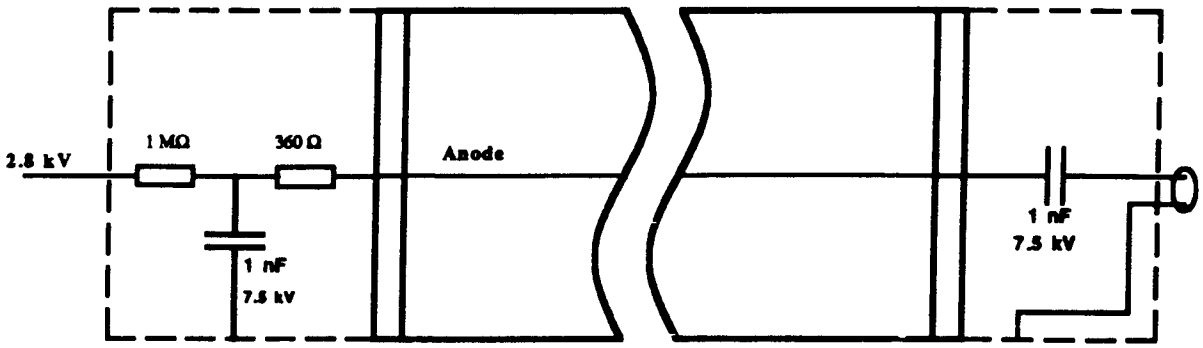

Figure 4.1. High voltage and signal connections.

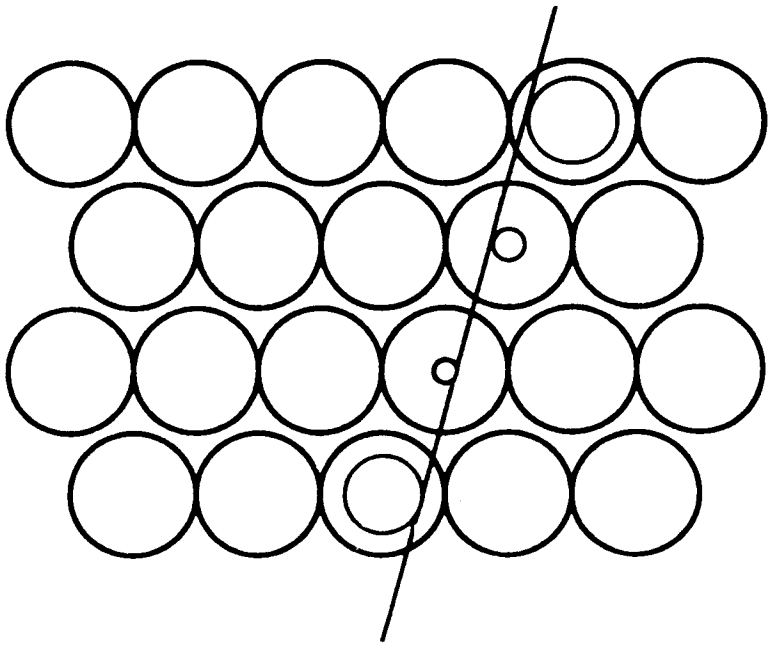

Figure 4.2. A reconstructed muon track.

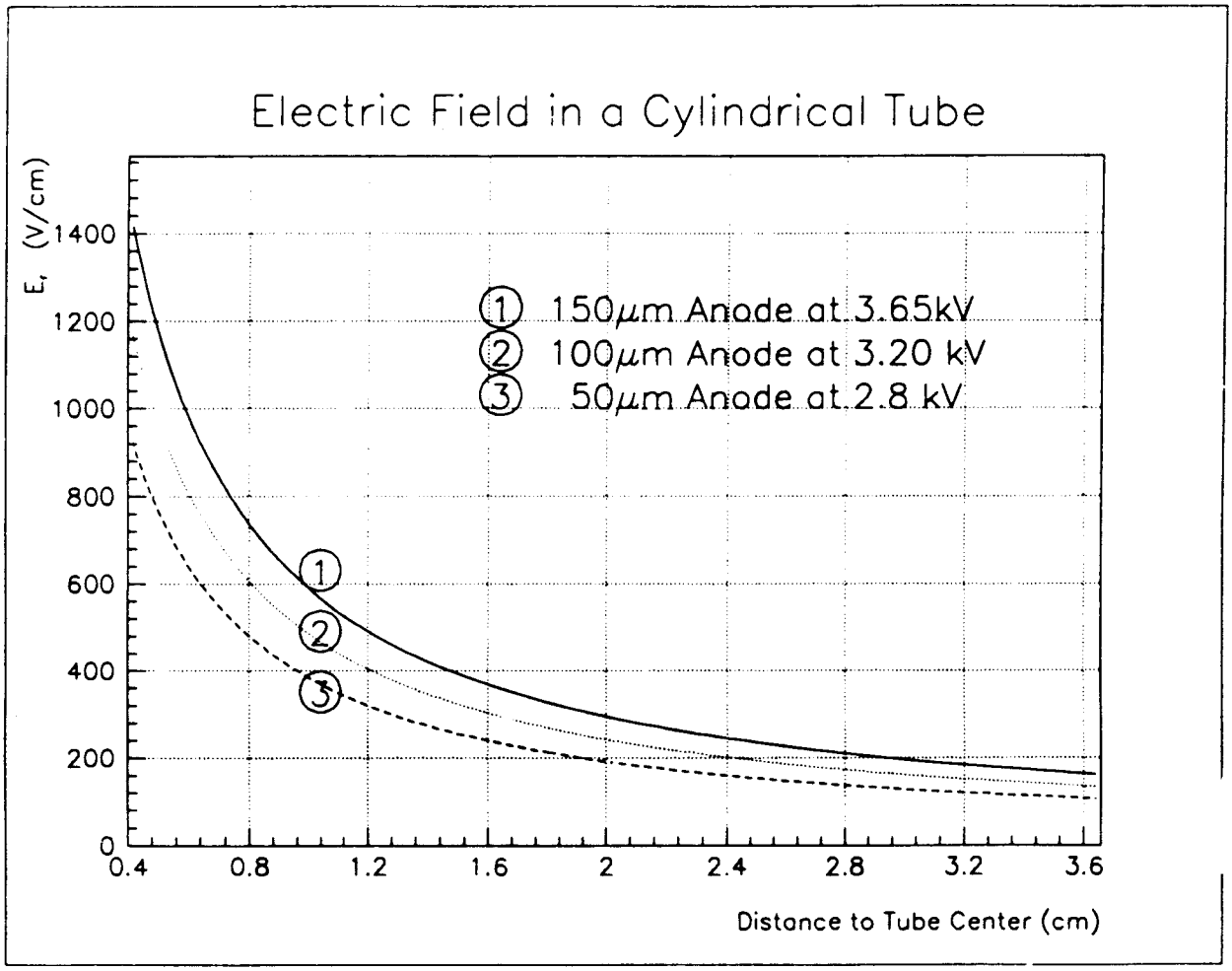

Figure 4.3. Electric fields as functions of distances to the tube center. Proportional mode operation using gas mixtures with 90% of argon and 10% of quenching gas is assumed.

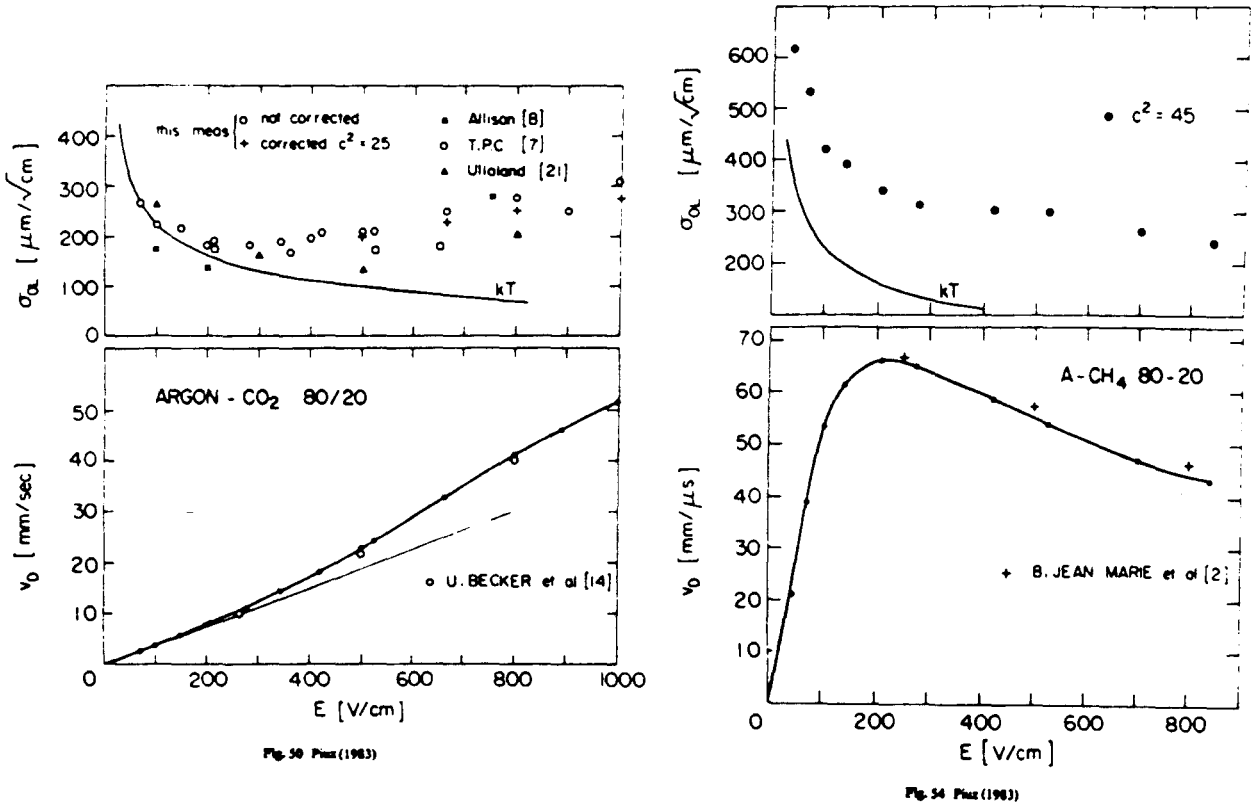

Figure 4.4. Electron diffusion for two gas mixtures.

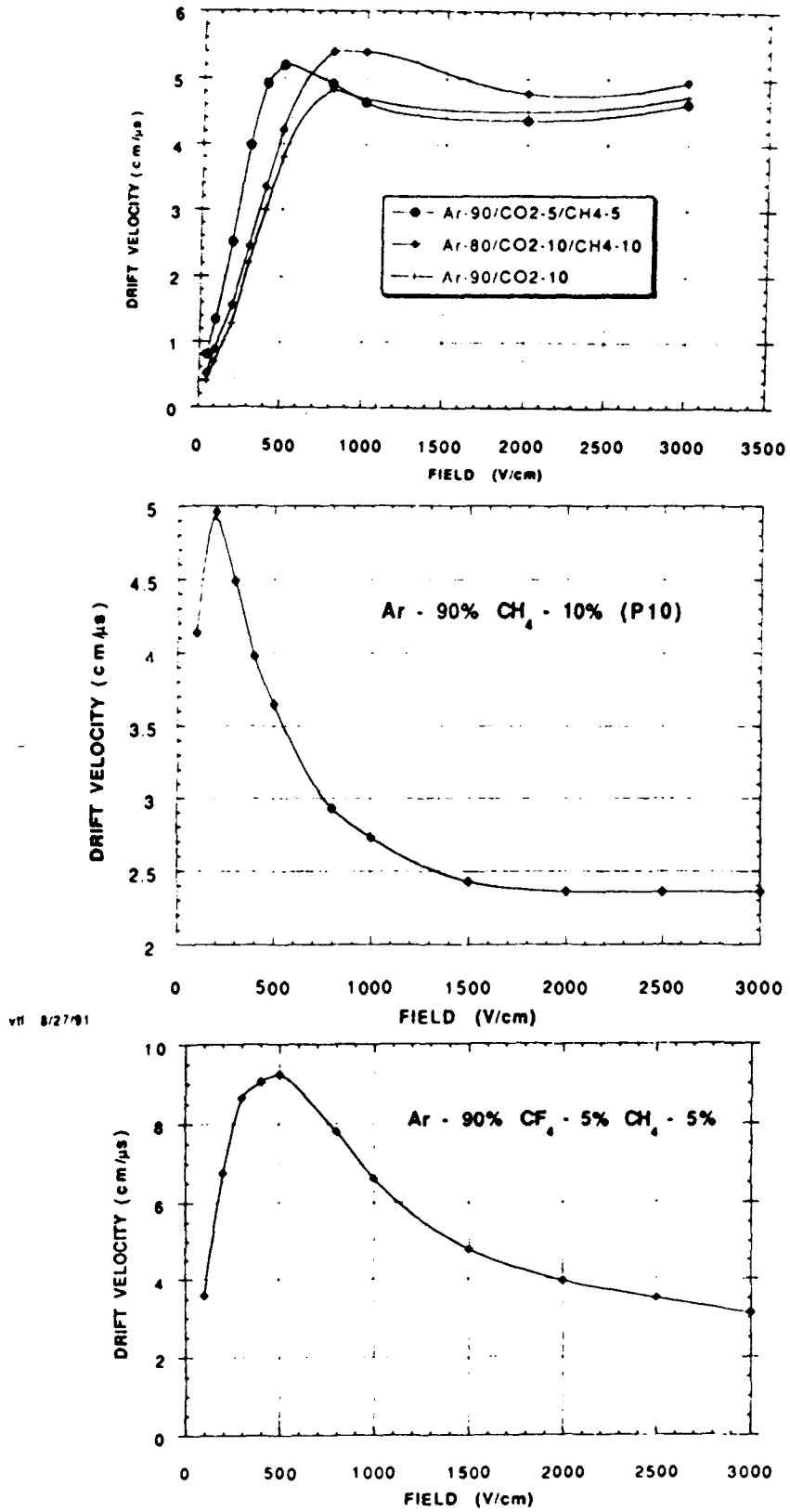

Figure 4.5. Electron drift velocity vs electron field.

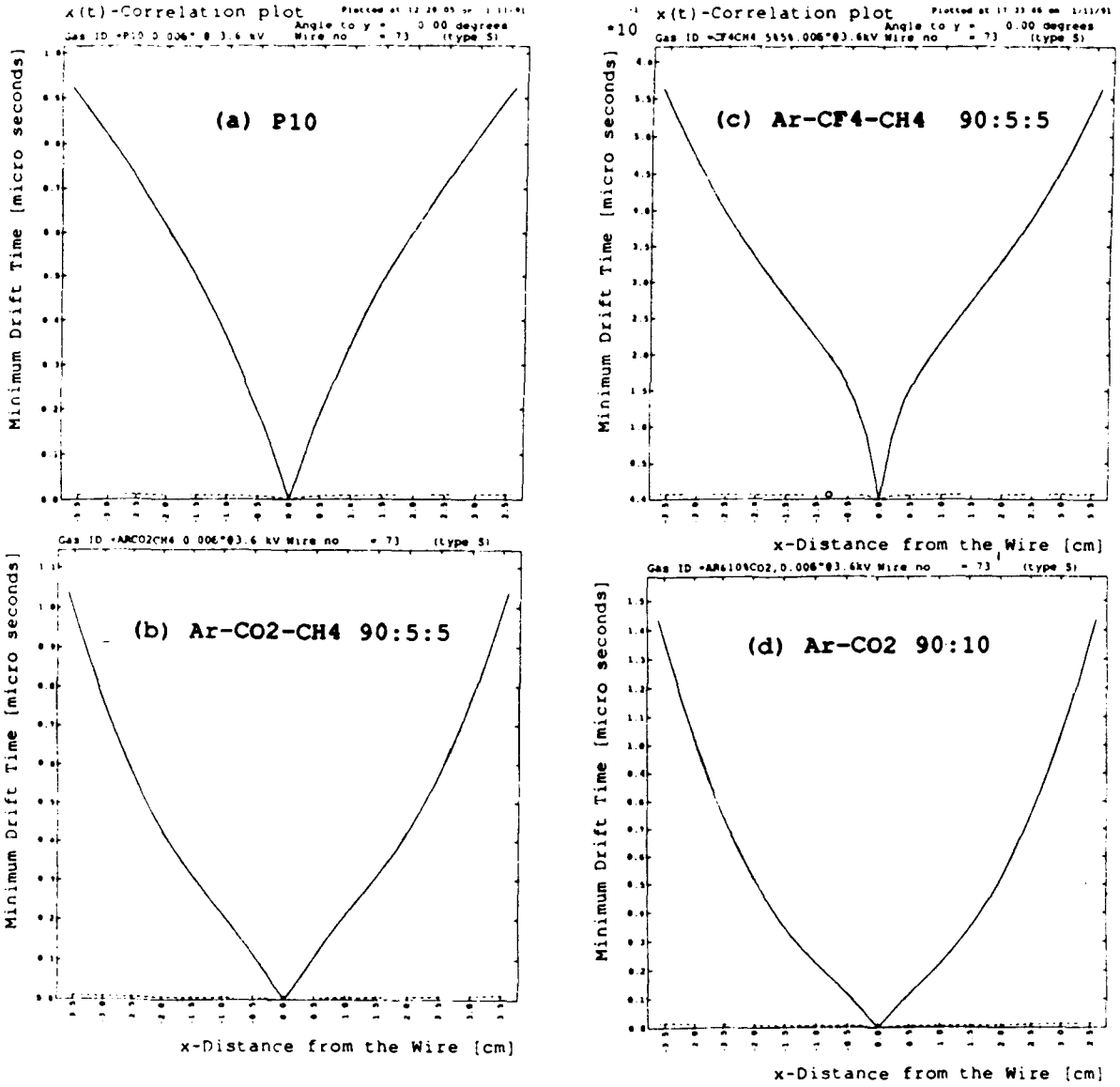

Figure 4.6. x-t correlation plots.

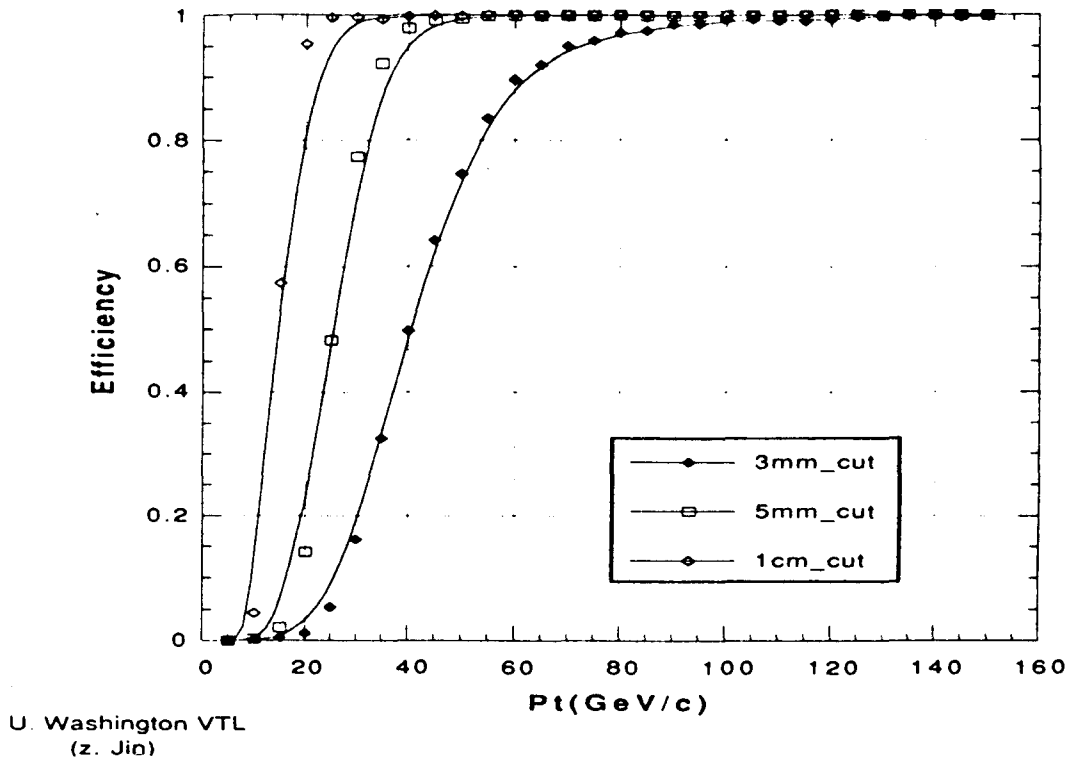

Figure 4.7. Trigger efficiency vs transverse momentum computed by assuming a nonlinear x-t correlation given in Figure 4.6b.

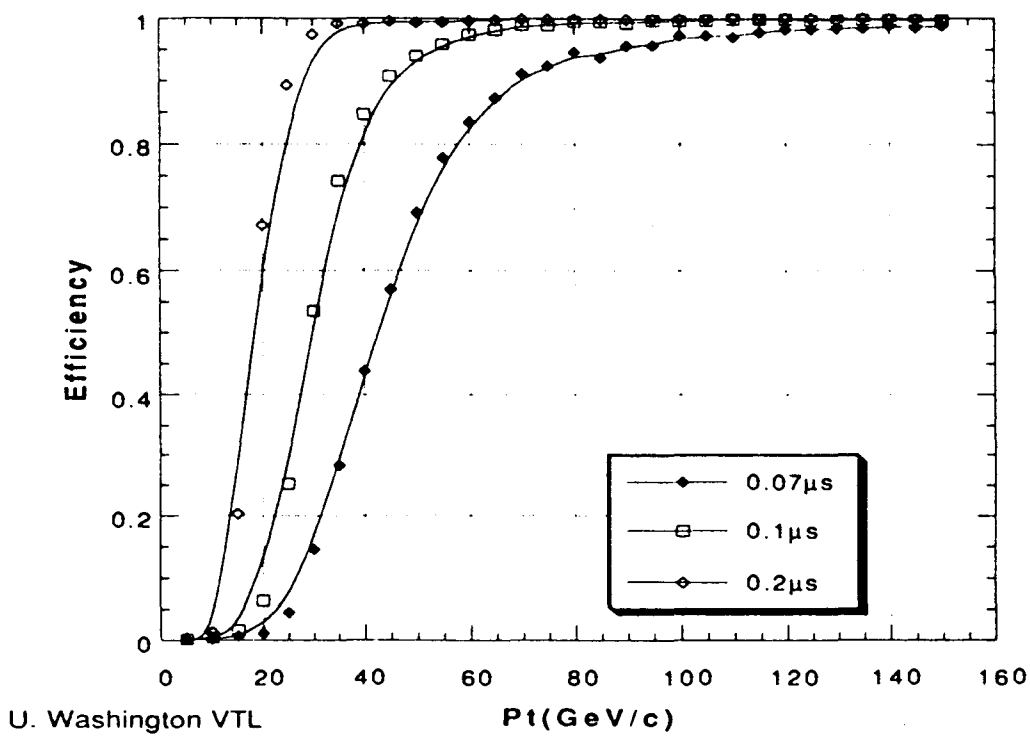

Figure 4.8. Trigger efficiency vs transverse momentum computed by assuming a linear x-t correlation.

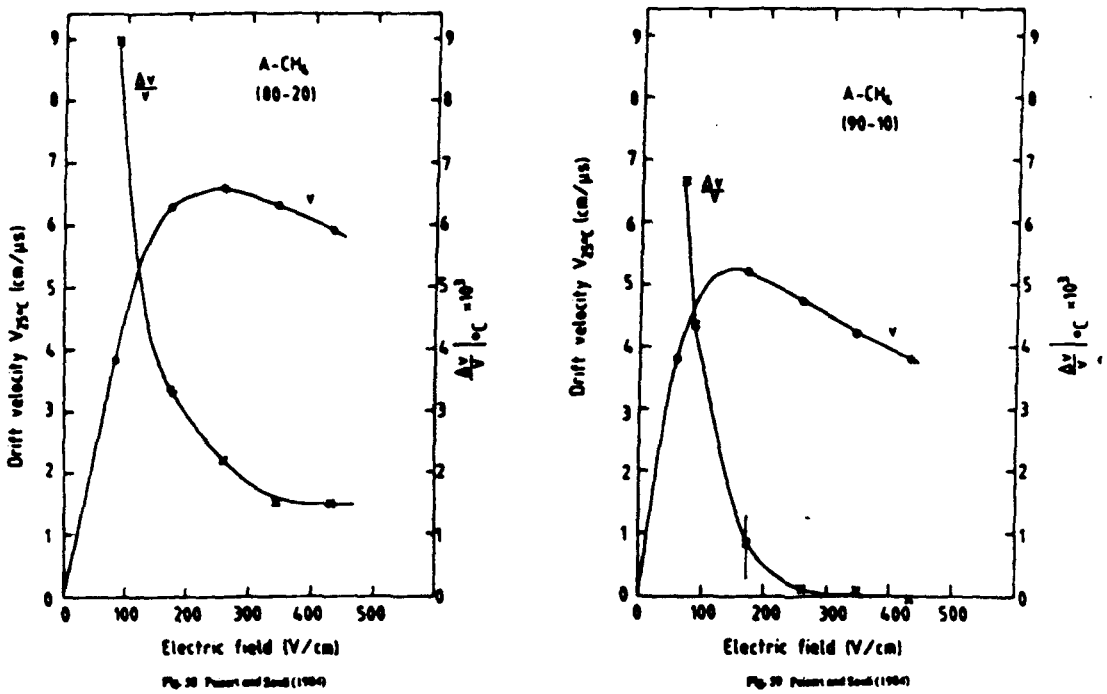

Figure 4.9. Temperature dependence of drift velocity for P10 gas.

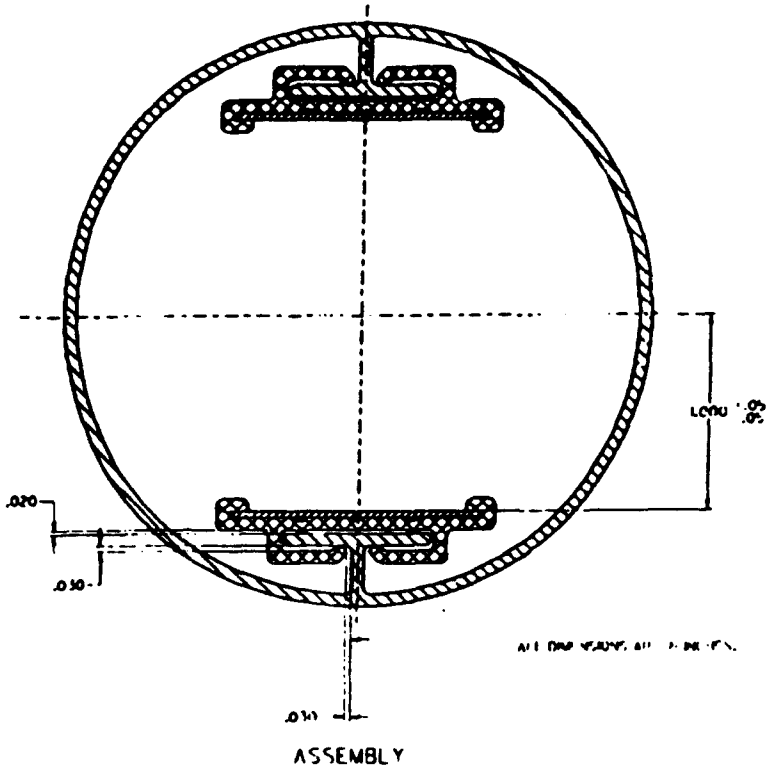

Figure 4.10. Cross section of a drift tube.

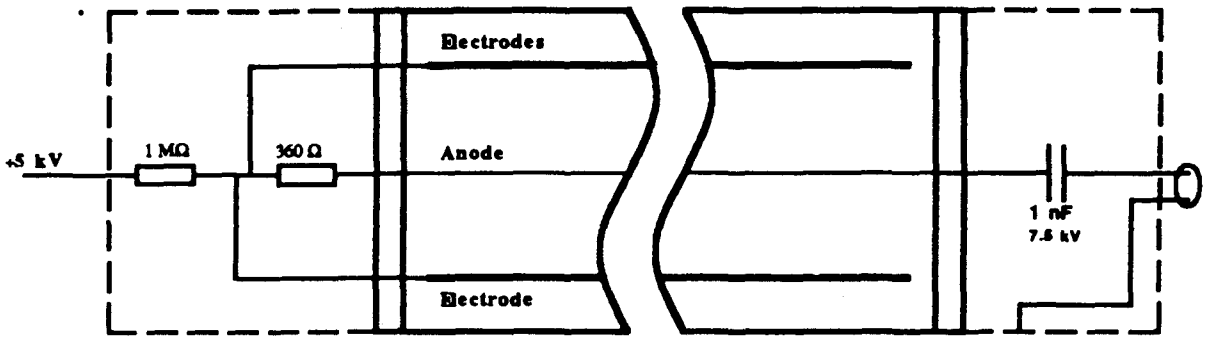

Figure 4.11. High voltage and signal connections. Field shaping electrodes and anode are both at +5 kV.

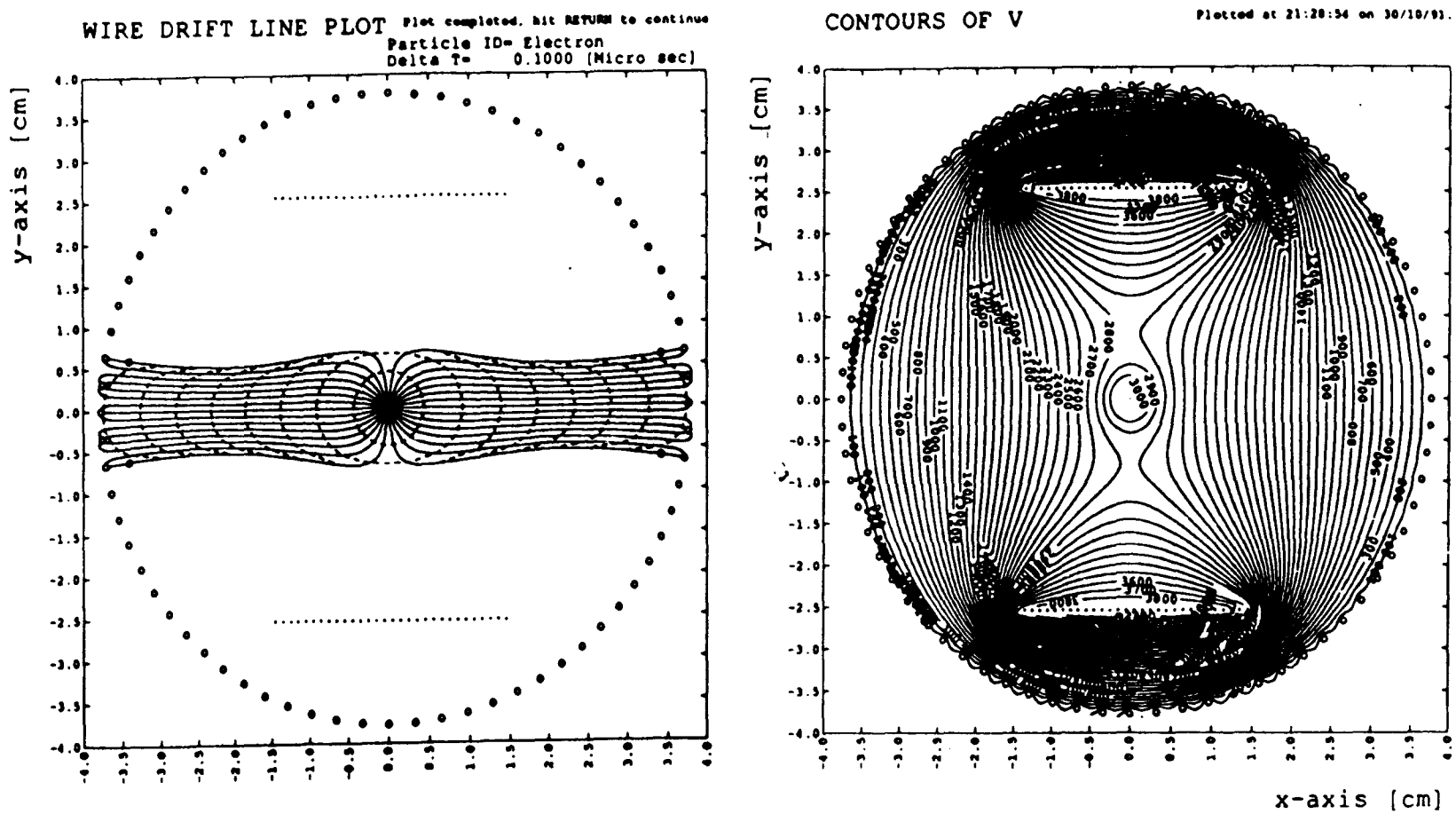

Figure 4.12. Drift field lines and equipotential contours. Anode and electrodes are both at +5 kV.

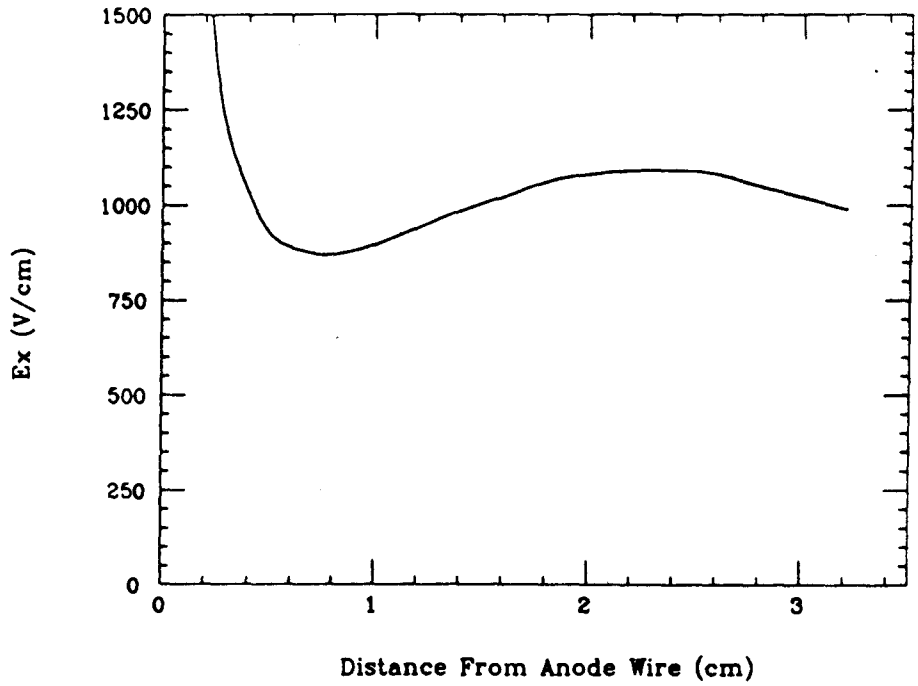

Figure 4.13. Drift field uniformity in the drift cell. Anode and electrodes are both at +5 kV.

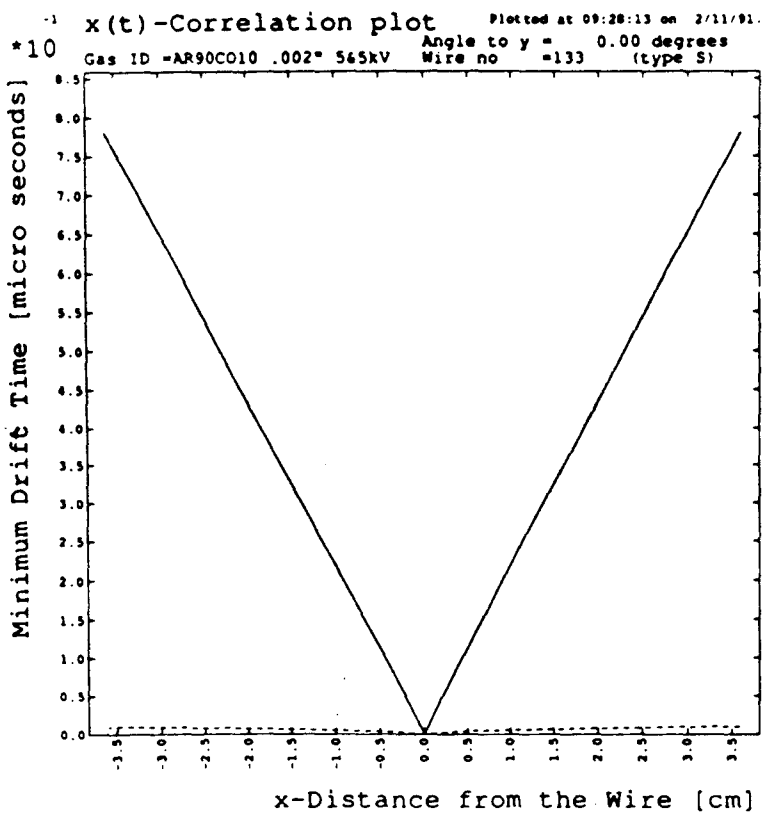

Figure 4.14. x-t correlation curve for Ar-CO_2 (90:10%). The maximum drift time is 780 ns.

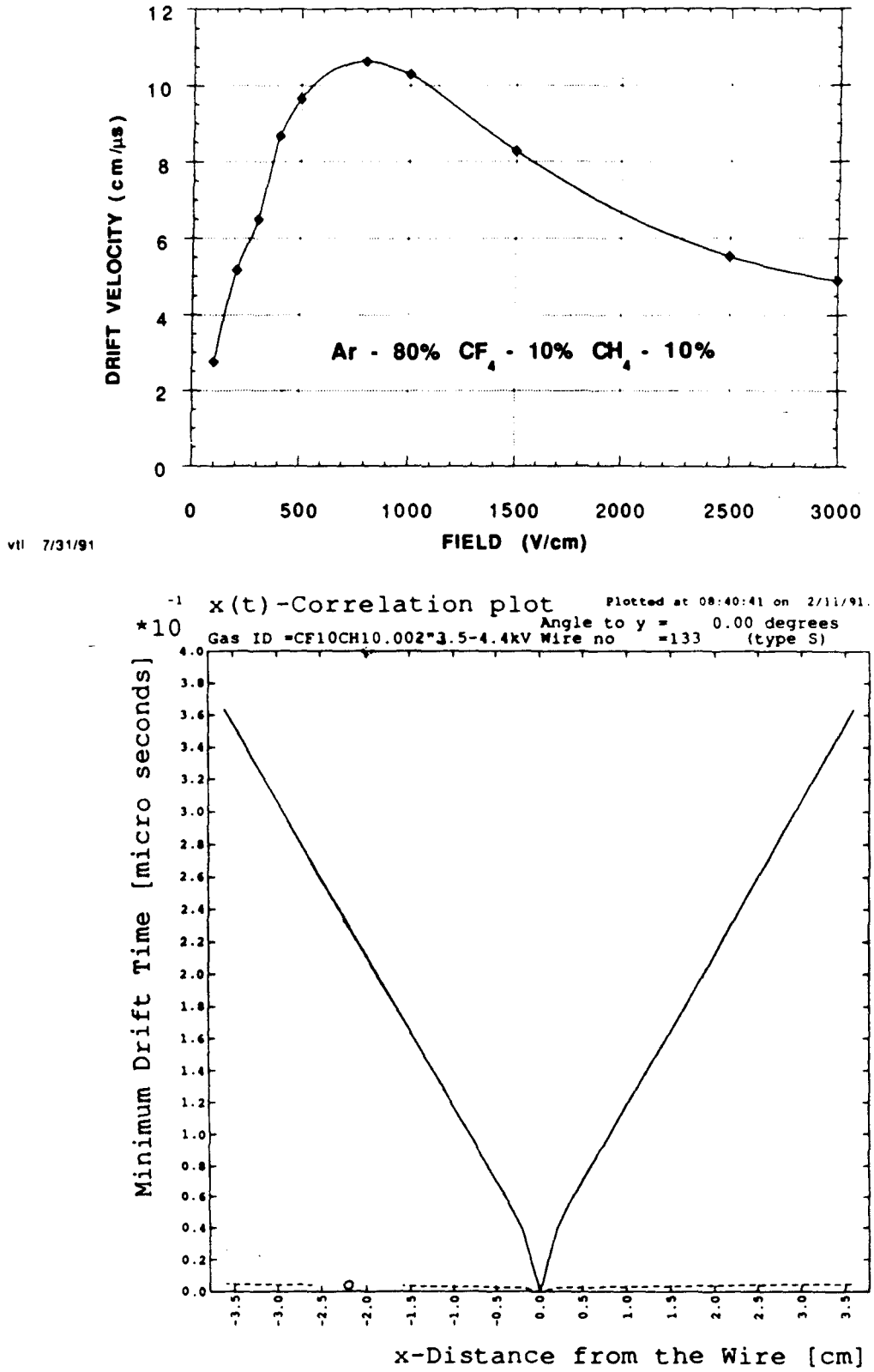

Figure 4.15. x-t correlation curve for $Ar\text{-}CF_4\text{-}CH_4$ (80:10:10%). The linearity of this curve is very good except for the region of r<0.5 cm. The maximum drift time is only 360 ns.

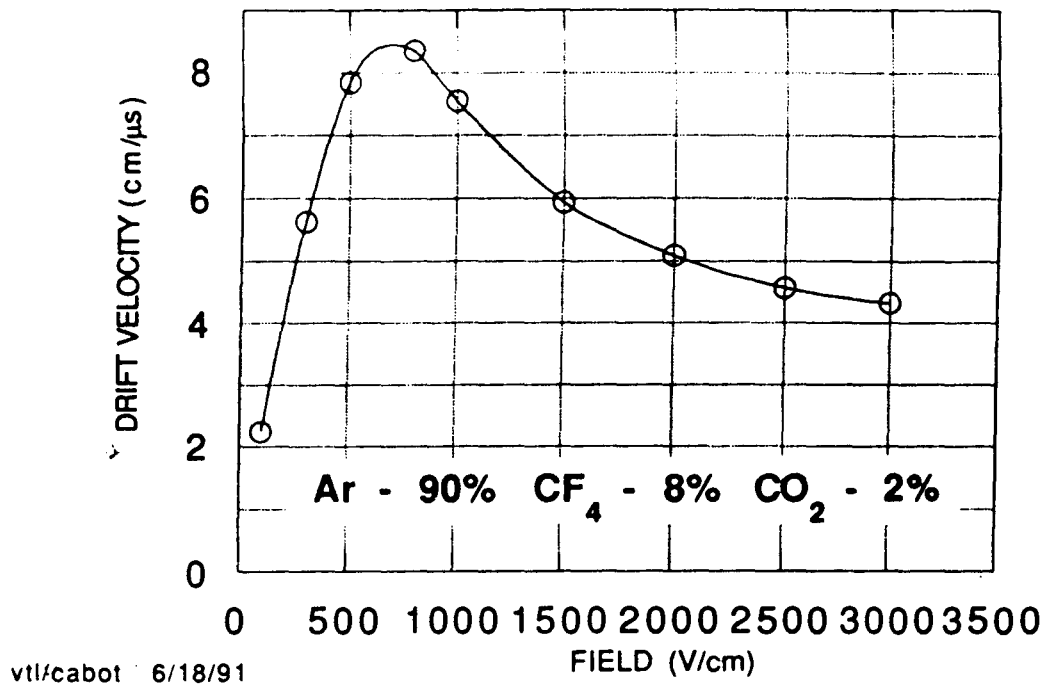

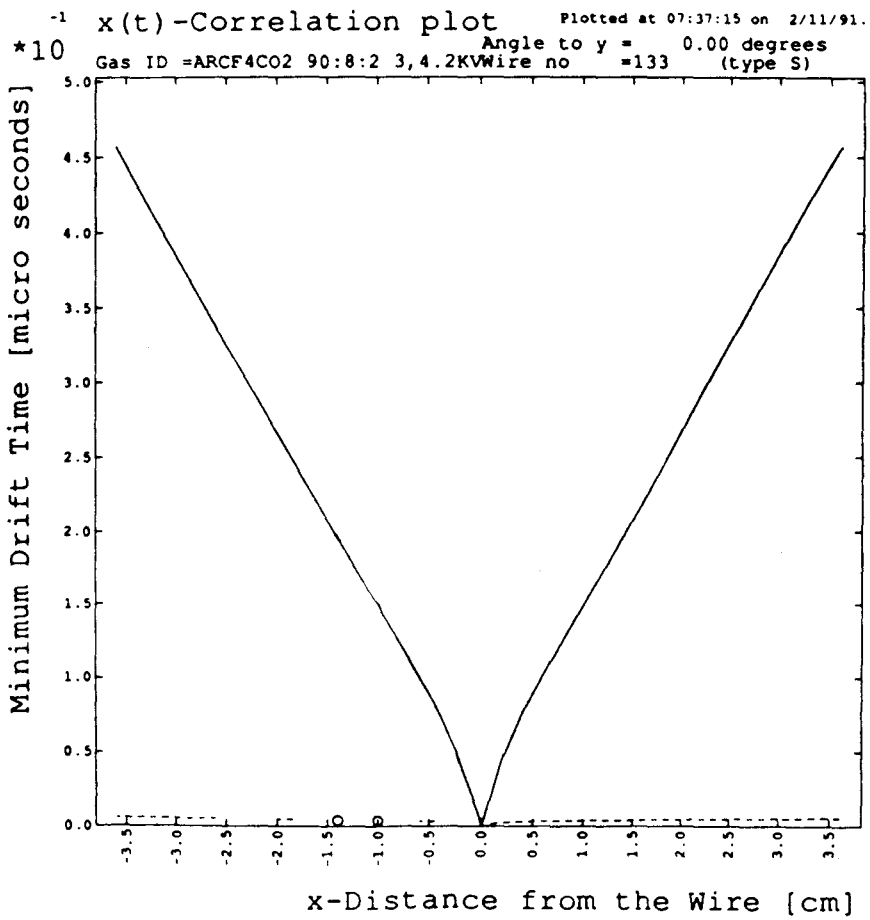

Figure 4.16. x-t correlation curve for Ar-CF_4-CO_2 (90:8:2%). The linearity of this curve is very good except for the region of r<0.5 cm. The maximum drift time is 460 ns.

5.0. TRIGGER

In this section, the basic level 1 trigger concept, the computer simulation and the trigger electronics design are discussed. The level 2 trigger will not be discussed since it is identical to that discussed in the SDC LoI.

The wire chamber trigger is similar to that used by CDF. Wires in every other plane are projective to the interaction point. The time difference Δt between pulse arrivals on paired wires is then inversely proportional to the transverse momentum of the trajectory of muons. Trigger thresholds are set on Δt by simple circuits. These circuits are designed in such a way that the P_t thresholds are programmable. The level 1 trigger system arrives at a decision within 1 μs after the beam crossing.

5.1 Level 1 Muon Trigger Simulations

5.1.1 Basic Trigger Arrangement

A minimum trigger system requires two layers of drift chambers. The problems associated with a minimum system consisting of only two chamber layers are:

1. Geometrical effects limit the efficiency. The drift tube walls create dead regions. Also, the trigger acceptance for a pair is not complete due to the toroid bend, especially for lower P_t muons.
2. False triggers can be generated when low P_t muons cross the projective line between the wires and appear to be high P_t muons.
3. False triggers can be generated due to the confusions caused by soft electrons accompanying muons with P_t lower than the threshold.
4. Triggers can be lost due to the confusions of soft electrons accompanying muons which have P_t higher than threshold.

In order to solve all four problems, we must use more drift chamber layers. For example, we can use all 8 layers of the θ-chambers in BW2 and BW3 as proposed by the Michigan group. A muon can fire four trigger pairs generating four time difference signals: T1, T2, T3 and T4. We require a good trigger to satisfy $(T1 \times T2)\cdot(T3 \times T4)$. As a result, the false trigger problem (2 and 3) and efficiency loss problem (1 and 4) are minimized. Results of our simulation discussed below are based on this arrangement.

In the simulation, drift tubes are arranged in 8 cm × 8 cm matrices. Anode wires are projective. The barrel chamber length is 16 meters. The first section of the calorimeter (0.7 meters) is assumed to be lead. (This is one of the options of possible calorimeter configurations.) The multiple scattering and toroid deflection are parameterized and calculated in 5 cm steps. The first station of trigger chambers (BW2) starts at r = 8.35 m. We define the beam direction as the z-coordinate in our study. For 1.5 meter toroid thickness, δz cuts of 3 mm, 5 mm and 10 mm correspond to nominal P_t thresholds of 40, 25 and 15 GeV/c, respectively, with 50% efficiency.

Effects such as the size of the interaction point, the iron toroid thickness, the trigger timing resolution, non-linear x-t relations and different trigger requirements are investigated.

5.1.2 Toroid Thickness

In Figure 5.1, trigger efficiency curves are given for three different toroid thicknesses: 1.5, 1.2 and 1.0 meters. The δz cut (P_t thresholds) have been adjusted to approximately 40 GeV/c for all three cases. The difference in trigger efficiencies between curves for 1.2 m and 1.5 m thick toroids is small. Even the 1 meter toroid is acceptable. However, the rejection capability against the low P_t muon is quite different for these three cases. All three curves in Figure 5.1 have 50% efficiency at about 40 GeV/c. At

20 GeV/c, the efficiency of the 1.5 meter thick toroid is 1.2%. On the other hand, the efficiency of 1.0 and 1.2 meter thick toroid is 3.7%. We can expect that the trigger rate will be much higher for a thin toroid.

5.1.3 Interaction Region Size

Effects of the size of the interaction region is shown in Figures 5.2 and 5.3. One of the two curves in each plot is produced by assuming that $\sigma_z = 5$ cm and the other curve is for $\sigma_z = 15$ cm. In Figure 5.2, the toroid thickness is 1.5 m and it is 1 m in Figure 5.3. Again, the δz cut is adjusted to 40 GeV/c. The consequence for the 1 m thick toroid if the spread of interaction region becomes wide ($\sigma_z \sim 15$ cm) is serious.

5.1.4 θ Dependence

The P_t trigger threshold depends on θ for a fixed δz cut. We can consider two cases:

1. The distance between chamber layers is fixed and the drift direction in the drift tubes is the beam direction. In this case

$$Pt_{threshold} \propto \delta z \times \sin^2\theta$$

   Figure 5.4 shows the comparison between a fixed cut of $\delta z = 3$ mm and a variable δz cut of 3 mm/$\sin^2\theta$. The softening of the trigger threshold due to the $1/\sin^2\theta$ dependence is obvious.

2. In our drift chamber system design, the drift tube is arranged in such a way that the drift field is tilted and high momentum muon tracks are always perpendicular to the drift field lines. In this case, we have

$$Pt_{threshold} \propto \delta z \times \sin\theta$$

   We expect that the trigger can be improved by the $1/\sin\theta$ correction. However, hardware realization for this continuous correction is difficult. We may have to divide the detector into several regions and do this correction in steps rather than continuously. Figure 5.5 shows the comparison between a fixed cut of $\delta z = 3$ mm and a variable δz cut of 3 mm/$\sin\theta$. The improvement due to the $1/\sin\theta$ correction factor is quite large. Another curve is computed by dividing the central muon detector into three regions: 90°–60°, 60°–45°, and 45°–35°. Three different cuts: 3 mm, 3.75 mm and 4.5 mm are used for these three region. These three cuts corresponds to 64 ns, 80 ns and 96 ns respectively. The fact that the two curves are approximately identical proves that a digital trigger circuit operating at 60 MHz is completely sufficient to correct the θ dependence of our trigger system.

5.1.5 Trigger Electronics Time Resolution

The design resolution of the muon drift chamber system is $\sigma_\theta = 250\ \mu$m or 5 ns. This is the fundamental limitation of our trigger design. The resolution of the trigger electronics is another limit. However, these are not important factors because the resolution of the level 1 muon trigger is dominated by the multiple scattering and the finite size of the interaction region. Figure 5.6 shows this is indeed the case. In Figure 5.6, one set of data is generated assuming that there is no time measurement error in our system. The other set assumes a randomly distributed error of ±8 ns in both

the start and stop time of the trigger electronics. These two curves are similar indicating that the sharpness of the P_t cuts will not be degraded by using 60 MHz trigger electronics.

5.1.6 Non-linear x-t Correlation

Non-linear drift velocity is introduced in Figure 5.7. Cylindrical drift tube (without field shaping) and Ar-CO_2-CH_4 with 90-5-5% gas mixture are assumed. For comparison, Figure 5.8 shows the trigger efficiency curve assuming the x-t correlation is linear. As expected, the non-linear drift speed slows down the rise of efficiency curves but not significantly.

5.2 Trigger Rate

The single muon trigger rate is calculated for different muon P_t thresholds. The integrated trigger rates are summarized in the table below.

TABLE 5.1. INTEGRATED TRIGGER RATE FOR DIFFERENT P_T THRESHOLD.

Z-CUT (mm)	P_t THRESHOLD (GeV/c)	RATE (Hz)
13	12	2701
10	15	1960
6.4	20	1062
3.2	40	259

The muon rate at the muon trigger chambers which we use is shown in Figure 5.9. The dotdash curve is for $|y|<1.5$, at a luminosity of 10^{33} $cm^{-2}s^{-1}$. The trigger efficiency used is computed for our proposed muon chamber system and trigger electronics described above. A toroid thickness of 1.5 m and an interaction size of $\sigma_z = 5$ cm is assumed. The error on the start and stop time of the trigger electronics is assumed to be ±8 ns. Effects of δ-rays are not included in these calculations.

5.3 Basic Requirements for the Level 1 Trigger Electronics

CMOS field programmable gate array (FPGA) is gaining popularity very rapidly. The key features of FPGA are its flexibility, large size, extremely fast speed and low power consumption. These features make it very attractive for trigger applications in high energy physics experiments. Compared to custom ASIC's, FPGA does not require an expensive and time consuming chip design process, and good design software support is available. In many cases, FPGA can be more cost effective than the custom ASIC.

We have implemented several trigger circuits into XILINX FPGA chips. The design of these circuits are based on a completely digital trigger scheme proposed by J. Oliver and T. Zhao. We also implemented a circuit very similar to the circuit proposed by J. Chapman. A working prototype which runs up to 60 MHz was demonstrated in the Madison trigger meeting last September by T. Zhao.

5.3.1 Time Required for Level 1 Trigger Generation

Due to the long signal collection time inside drift cells, the time required to generate the level 1 muon trigger is the determining factor for the total pipeline length of the entire SDC detector readout electronics. Our group has proposed a drift chamber system based on cylindrical drift cells with 3.7 cm maximum drift distance. Without field shaping, the maximum drift time can be limited to within 1 μs using P10 or some other gas mixtures. With field shaping, the maximum drift time is 780 ns for conventional gas mixtures and is less than 500 ns for some fast gas mixtures containing small amount of CF_4. It is also extremely important to minimize the processing time of the level 1 electronics.

5.3.2 ΔT Coverage

The basic trigger element of the level 1 muon trigger system is a pair of drift tubes which are separated by about 16 cm/sinθ in our design. The maximum time difference which the trigger circuit has to cover occurs at the lowest P_t and at the smallest θ in the central detector. At $\theta = 40°$ and for $P_t =$ 10 GeV/c p_t muon, the time difference which the trigger circuit has to cover is $\Delta T = T1 - T2 \sim 500$ ns or about 30 clock cycles for a digital trigger running at 60 MHz.

5.3.3 Time Resolution

The fastest XILINX FPGA is rated at 130 MHz which limits the trigger time resolution to 8 ns corresponding to 0.4 mm in terms of drift distance for conventional gas mixtures. In terms of angular measurements, the maximum error given by such trigger electronics is 2.5 mrad. For comparison, the angular smearing due to multiple scattering in the calorimeter and iron toroid is $\sigma_\theta \sim 4$ mrad for a 40 GeV/c muon. The limitation of the trigger angular resolution due to the 5 cm interaction region size is $\sigma_\theta = 6$ mrad at r = 8.5 meters. Therefore, a digital trigger system operating at 60 MHz is sufficient.

5.3.4 Programmability

The trigger logic should be field programmable in order to accommodate unexpected problems and changes in trigger strategies during the experiment's many year life time.

5.4 Circuit Designs

5.4.1 Circuit 1

Figure 5.10 shows the block diagram of a simple trigger circuit. The major component of this circuit is a 24 bit shift register. The clock of this shift register is started by the OR of the two wire hits and stopped by the AND of the two wire hits. The location of the first arrival hit in the shift register is directly related to the P_t of the muon track. Output switches select the desired P_t thresholds and the trigger output is stored in registers for further processing. A complete logic diagram is shown in Figure 5.11.

This circuit is sensitive only to the first arrival signals in each drift tube. Because of this, a high P_t muon can be lost if soft electrons accompanying it create a hit earlier than the real muon hit. Also, low P_t muons can generate false triggers due to soft electrons. In a minimum trigger system which consists only of 2 layers of chambers, these problems would be very serious. However, in a trigger system using all 8 θ layers of BW2 and BW3, these two problems are minimized due to the redundancy of the system. We expect this simple circuit to give satisfactory performance.

5.4.2 Circuit 2

The circuit shown in Figure 5.12 is very similar to the circuit suggested by Jay Chapman. In this case, signals propagate to opposite directions in two shift registers. Properly arranged coincidence gates among the shift register outputs determine the P_t of the muon track. This circuit has multihit capability. In the example shown in Figure 5.12, there are four different trigger thresholds available for further processing.

5.4.3 Implementing into XILINX FPGA

We have implemented the two circuits discussed above into a 3020 chip mounted on a Xilinx prototype development box. The Xilinx 3020 chip used is rated at 100 MHz. But, the development system box limits our clock speed. As a general testing device, it has switches and headers, long printed circuit traces and wire connections. Even with these bad features, we are still able to operate the system at 60 MHz.

In order to evaluate the performance of our proposed trigger system, a CAMAC module which contains two 3020 chips has been constructed. The logic diagram of this CAMAC module is shown in Figure 5.13. Discriminated outputs from a cosmic ray test station which consists of four drift tubes are fed into this CAMAC module and also into a LeCroy 2277 multihit TDC module. This system simulates our proposed level 1 muon trigger system. It is now operational and the evaluation is in progress.

The circuits in the CAMAC module can be operated at a maximum speed of 66 MHz. The reason that we cannot operate the chips at their rated speed of 100 MHz is because we have used standard printed circuit board for prototypes and did not use custom designed boards.

5.4.4 Trigger System Design

In the barrel region, we will need approximately 12,000 channels of trigger circuits. This will require 12,000 Xilinx 3020 chips. The total number of chips can be reduced by using bigger chips. These chips will be divided into boards and crates according to the the geometric arrangement of drift chamber modules. The obvious location for the level 1 trigger crates is the space available in between BW2 and BW3.

As proposed by the Michigan group, it is necessary to use all 8 θ layers in BW2 and BW3 in order to minimize the fake trigger rate due to low P_t muons. The basic trigger requirement is $(T_1 \times T_2) \cdot (T_3 \times T_4)$. T_1 is the trigger signal generated by a pair of tubes in chamber layer 1 and 3 of BW1. T_2 is the OR of two neighbouring cells from layer 2 and 4 of BW2. T_3 is from layer 1 and 3 in BW3 and T_4 is from layer 2 and 4 in BW3.

We have to interconnect the trigger signals between BW2 and BW3. A muon with $P_t = 10$ GeV/c is deflected from the projective line by about ±30 cm. Therefore, both T_3 and T_4 have to be the OR's of at least eight pairs of drift tubes. It requires rather complicated interconnections in order to form a complete trigger tower.

5.4.5 Future Plans

We expect to complete the evaluation of our CAMAC trigger prototype based on 3000 serial chips in the next few months. With the new Xilinx 4000 serial devices, we expect that 120 MHz clock speed can be achieved. The availability of the chips are still limited and the design software is evolving. We plan to upgrade our system to the Xilinx 4000 in 1992.

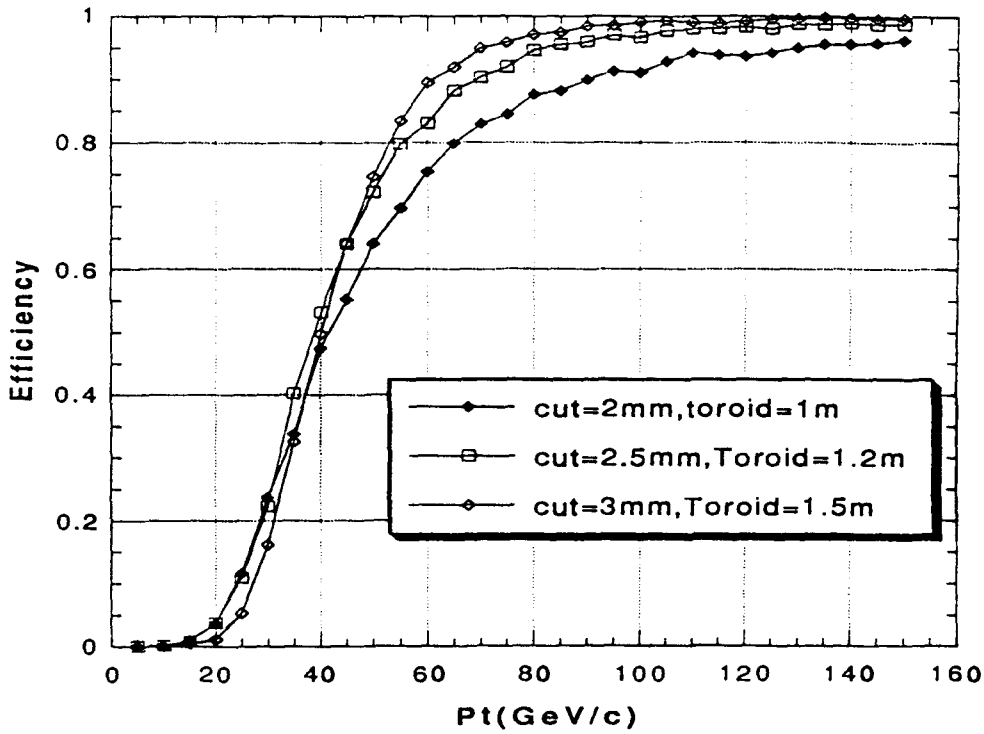

Figure 5.1. Trigger efficiency vs P_t for three toroid thickness.

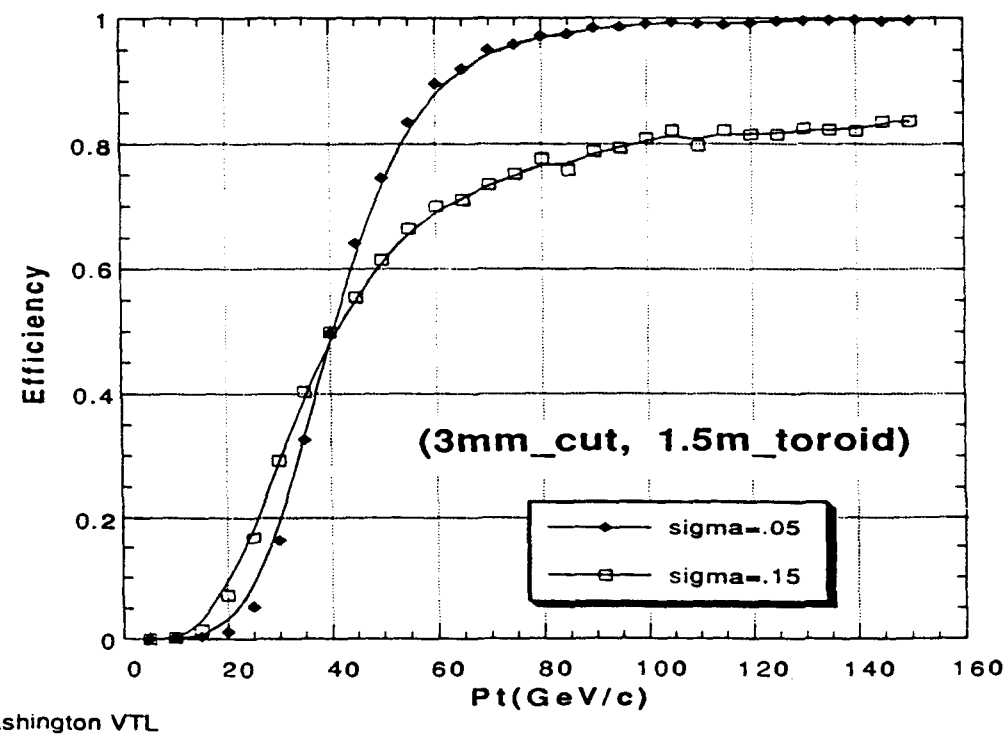

U. Washington VTL

Figure 5.2. Different interaction region sizes and a 1.5 m thick toroid.

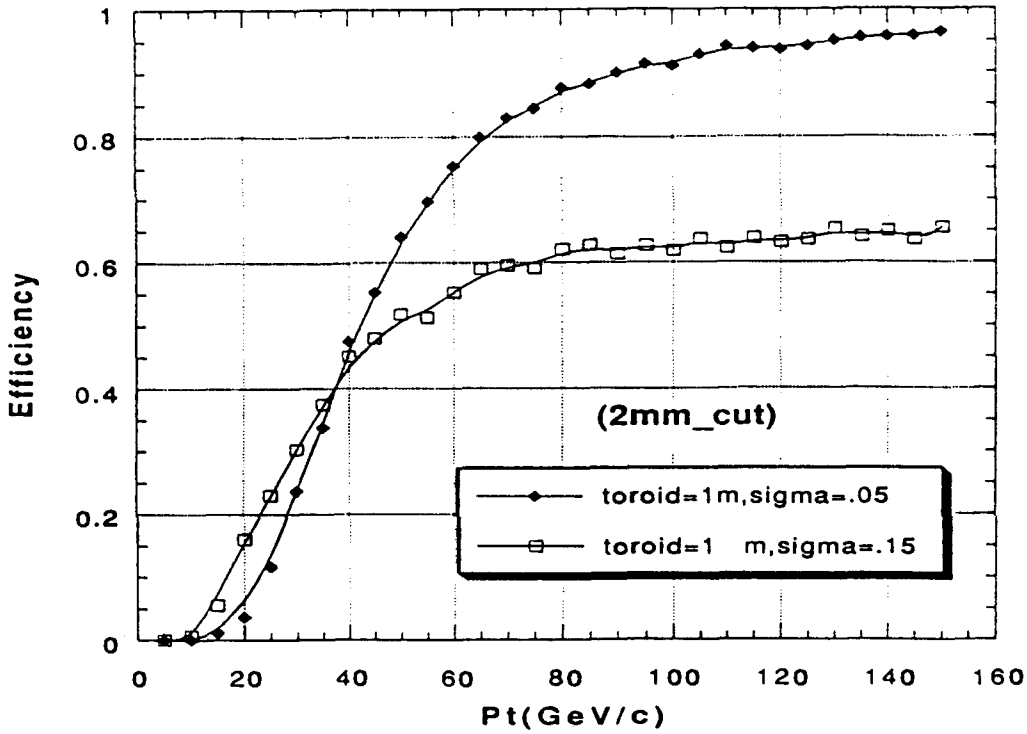

Figure 5.3. Different interaction region sizes and a 1.0 m thick toroid.

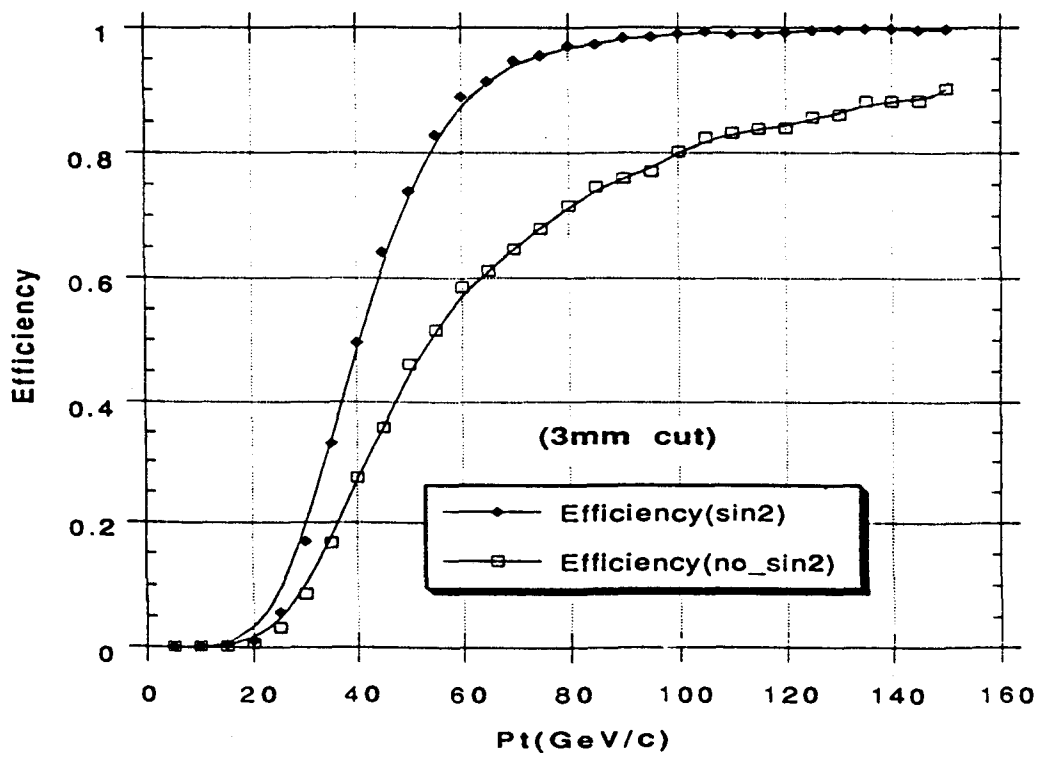

Figure 5.4. Comparison between a constant 3 mm cut and a 3 mm/$\sin^2\theta$ cut.

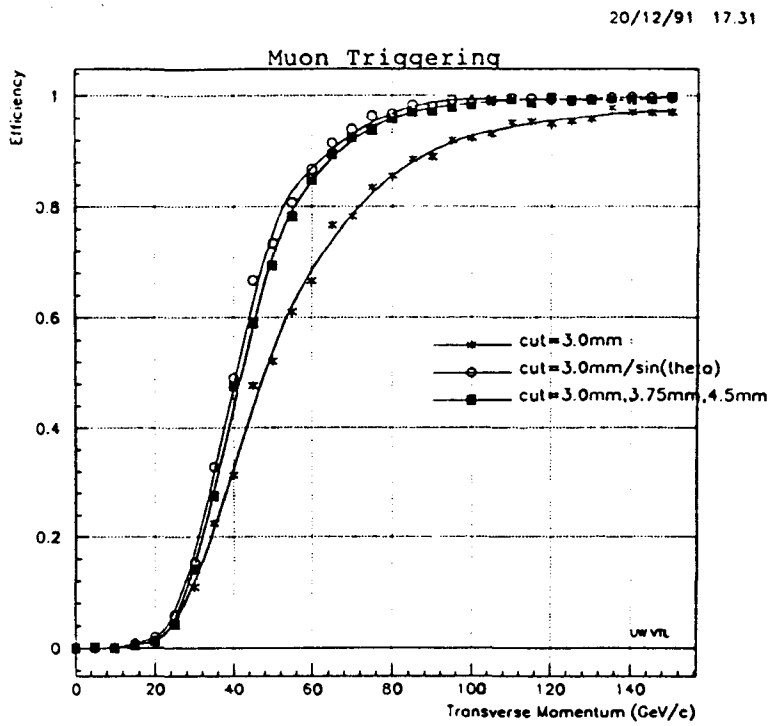

Figure 5.5. Three different cuts for round tubes.

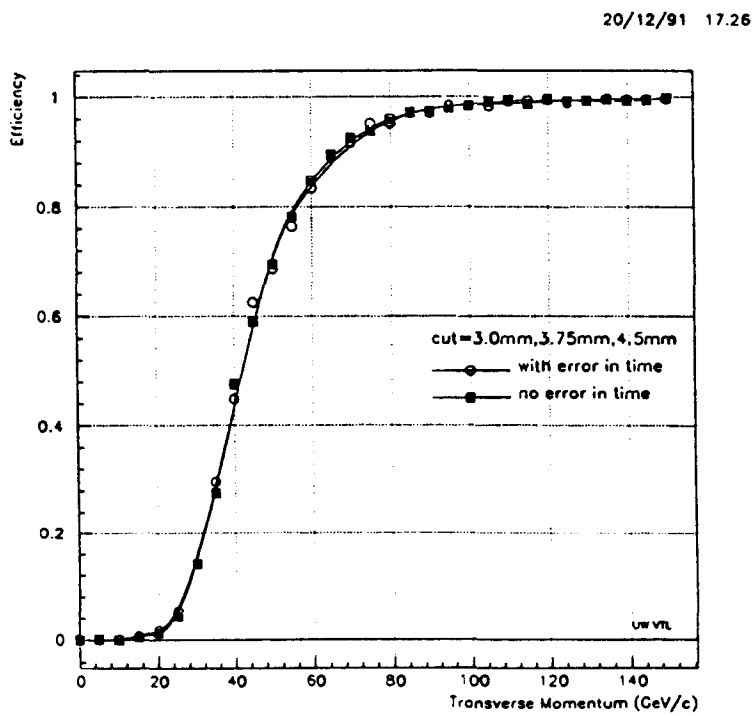

Figure 5.6. ±8 ns error of trigger electronics start and stop time makes no difference.

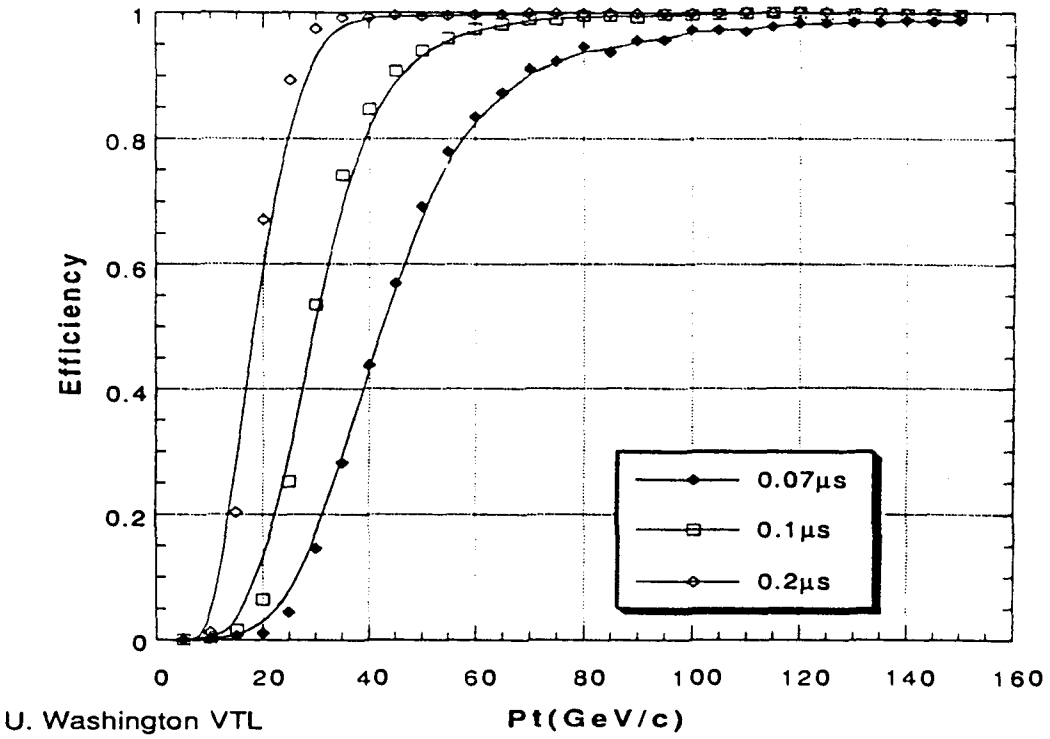

Figure 5.7. Trigger efficiency vs P_t assuming a non-linear x-t correlation.

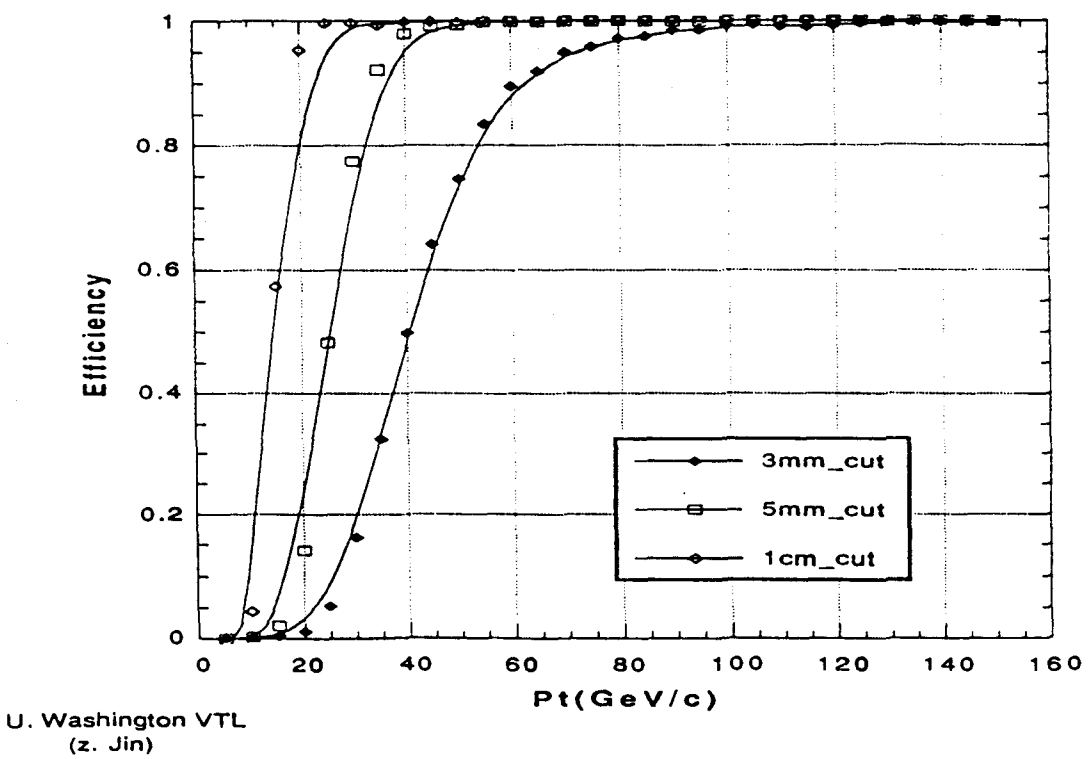

Figure 5.8. Trigger efficiency vs P_t assuming a linear x-t correlation.

Sakai's study

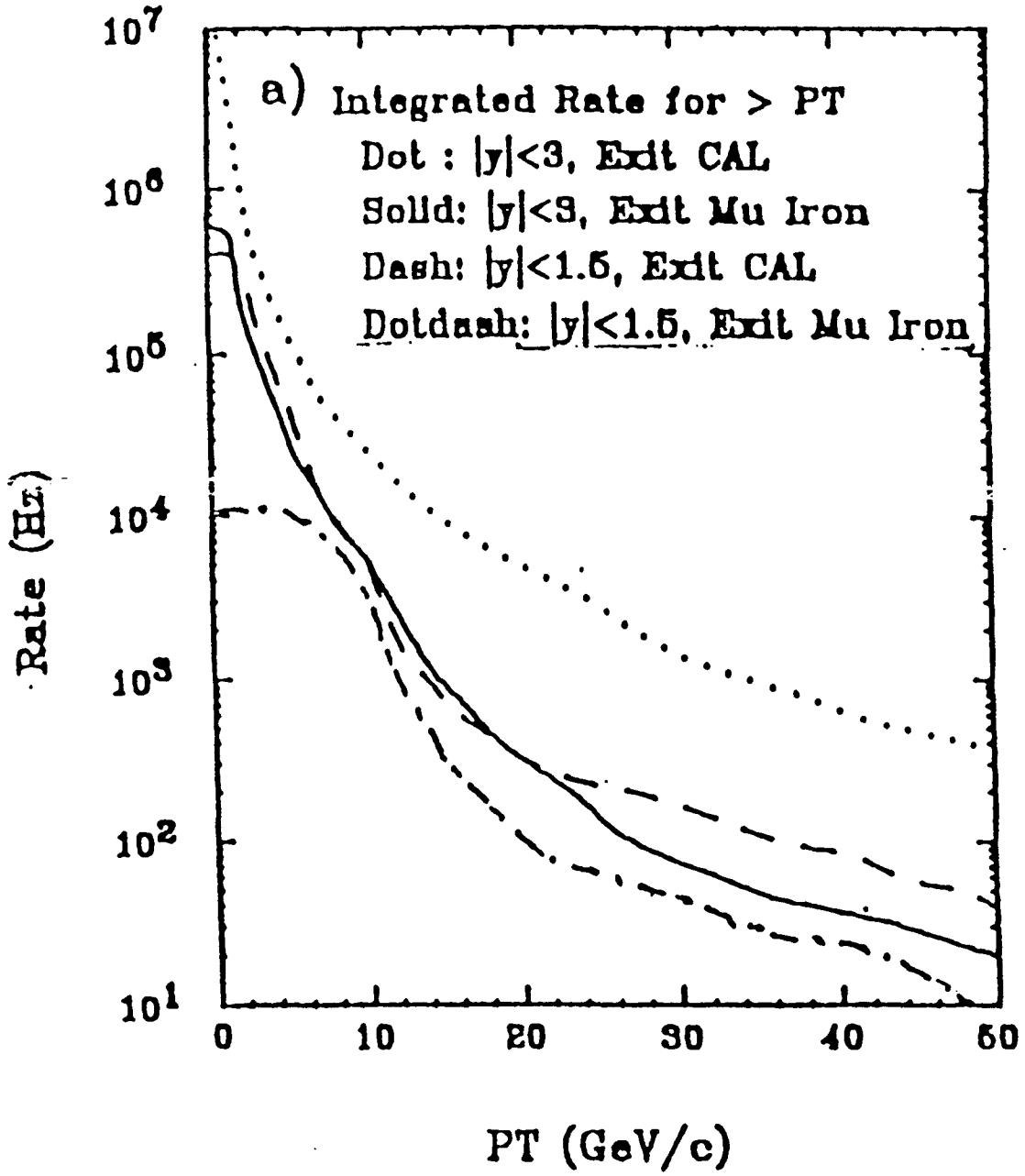

Figure 5.9. Muon rate calculated by Sakai.

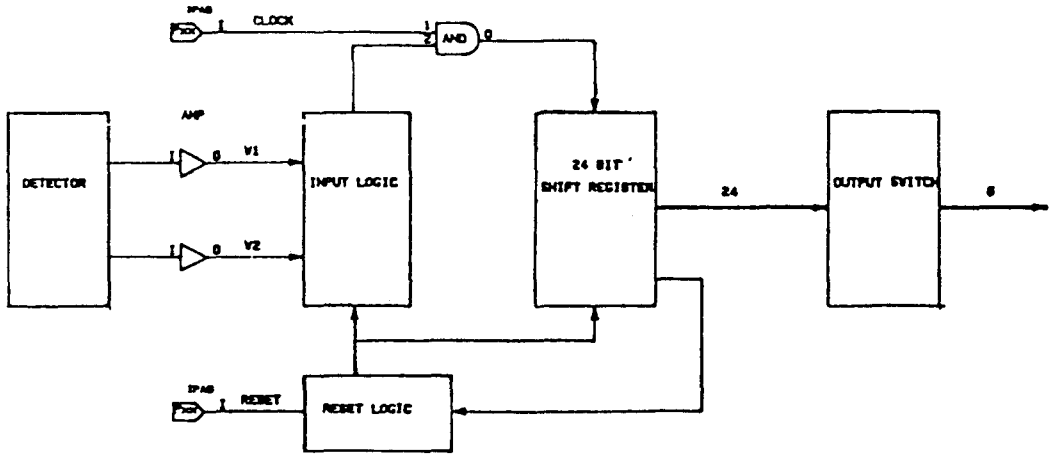

Figure 5.10. Block diagram of trigger circuits.

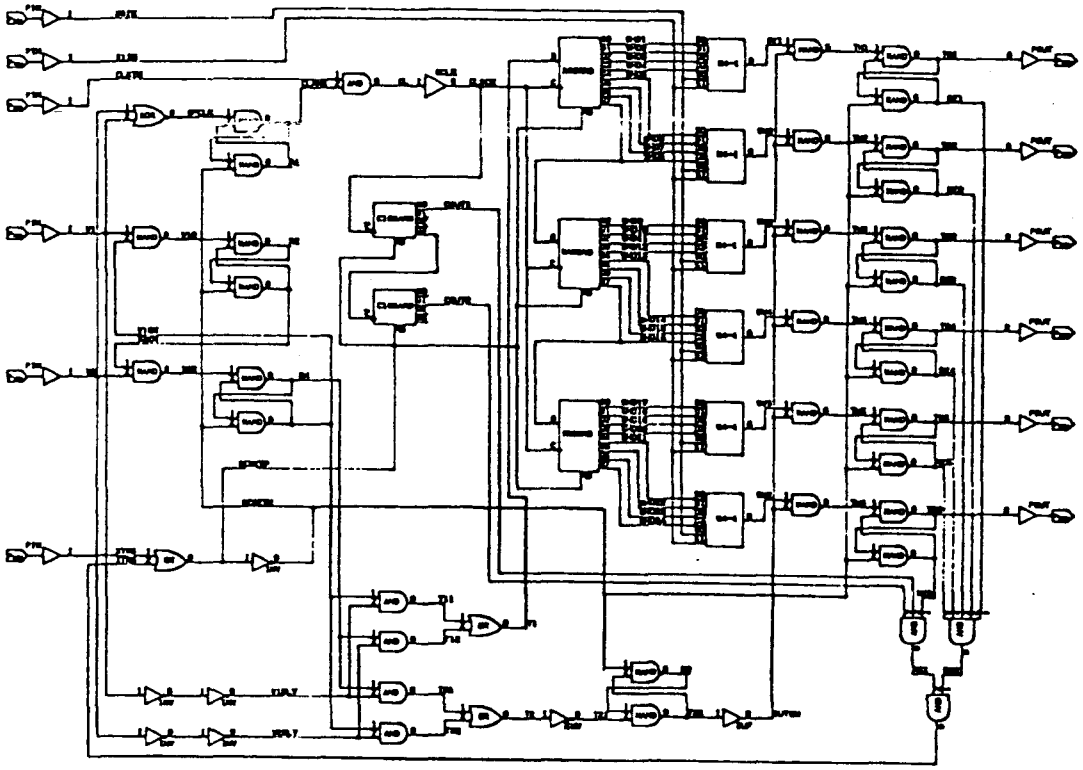

Figure 5.11. Logic diagram of circuit 1.

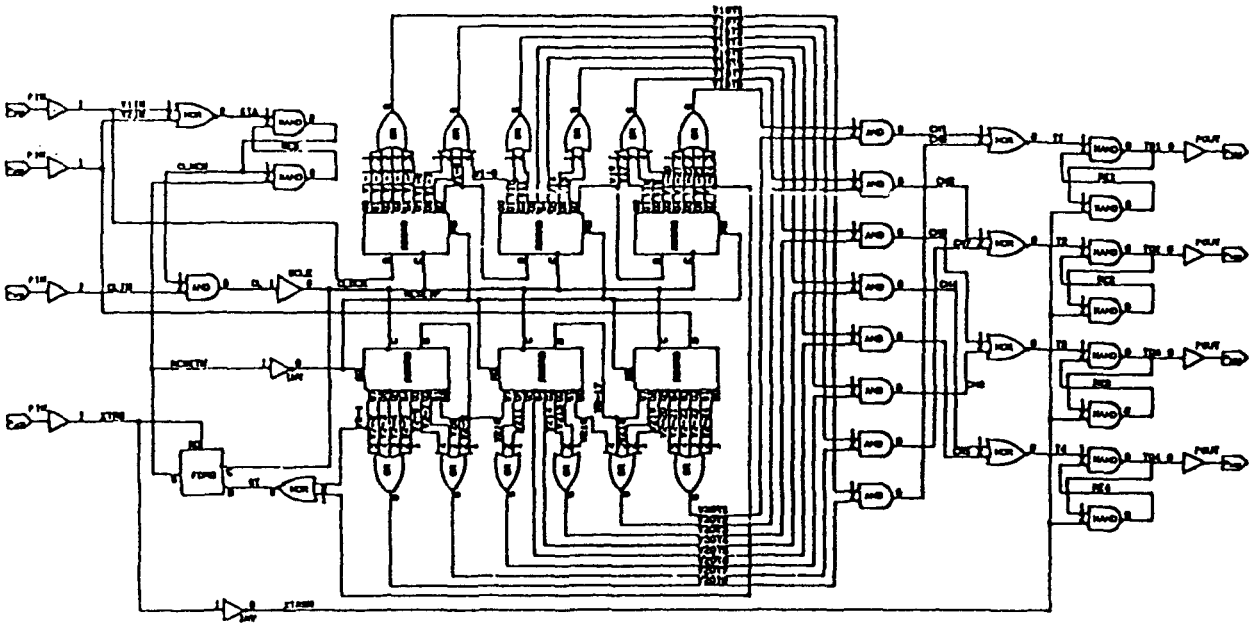

Figure 5.12. Logic diagram of circuit 2.

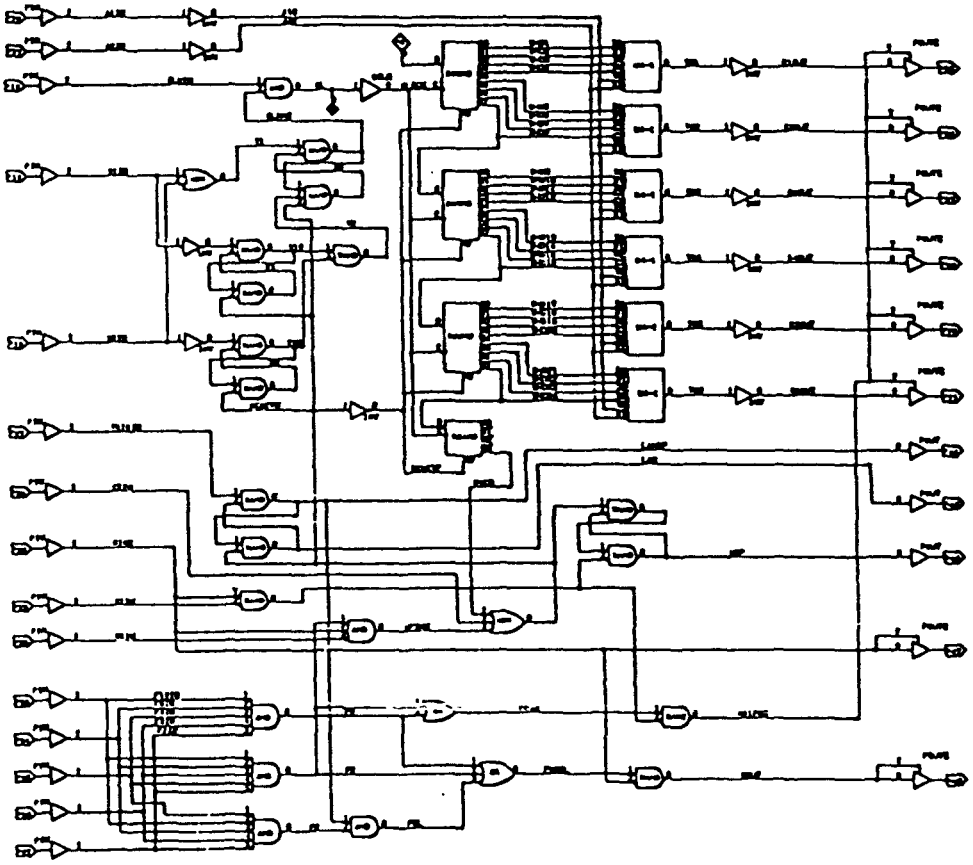

Figure 5.13. Logic diagram of the CAMAC trigger module.

6.0 CELL CONSTRUCTION

The muon chamber design consists of two different options. One of these designs incorporates the use of field shaping electrodes to shape the electric field while the other does not. However, the components used to fabricate both the field shaping and the non field shaping options are quite similar. The differences between these components are explained in detail in the following sections:

6.1 Aluminum extrusions
6.2 Field shaping electrodes (Field shaping design only)
6.3 End caps
6.4 Anode wire
6.5 Gas fitting

6.1 Aluminum Extrusions

The muon chamber design consist of two separate extrusion profiles. The non field shaping design utilizes 75 mm outside diameter (O.D.) by 1.6 mm wall thickness (W.T.) round tubes. The field shaping design consists of 75 mm O.D. by 1.6 mm W.T. extruded tubes with two tees inside as shown in Figure 6.1. Both the field shaping and the non field shaping tubes are extruded from 6063-T5 alloy aluminum. After the tubes are extruded, the ends are machined square and the internal tees (field shaping option only) are cut back as shown in Figure 6.1. This machining is accomplished using a commercial tube finishing machine capable of machining both ends of the tubes at the same time. After machining, the tubes are chromate conversion coated (yellow alodyne) to enhance their surface conductivity. The alodyne process also cleans the tubes of any oils that may have been used during machining.

6.2 Field Shaping Electrodes

Field shaping electrodes are used only in the field shaping drift tube design. These electrodes are fabricated by coextruding Noryl and a thin alodyned aluminum strip into the shape shown in Figure 6.2. The aluminum strip is alodyned using a spray-on alodyning process. The electrode is installed inside the drift tube by sliding it over the extruded tee shape as shown in Figure 6.3.

6.3 End Caps

End caps are located on both ends of the drift tubes. These end caps are assembled on the drift tubes as shown in Figures 6.3 – 6.6. The design goal was to include all the passive electrical components in the end caps, which provide a shield against electrical noise. The end caps are fabricated from the following components:

1. End cap shells
2. Injection molded supports
3. Contact springs
4. Electrical components
5. CERN feed throughs

These components are discussed in detail in the following sections.

6.3.1 End Cap Shells

The end cap shells are made from 6061-T6 aluminum so that they can be machined to 12.5 micron (0.0005 in.) precision. This precision is necessary to accurately position the anode wire with respect to the CNC milled reference end plates. The end cap shown in Figure 6.7 uses a 25 mm precision machined boss as its reference surface. This boss is positioned in the CNC milled reference end plate as shown in Figures 6.8a, 6.8b, and 6.8c.

The end cap shell on the opposite end of the tube cannot be identical to the previously mentioned end cap as it must slide across the face of the reference end plate during the assembly process. Therefore, the second end cap (Figure 6.9) has a flat surface and is positioned by dowel pins as shown in Figure 6.8c. The dowel pins are the precision surfaces that references the end cap position to the CNC milled reference end plate.

6.3.2 Injection Molded Supports

The injection molded supports shown in Figures 6.10 and 6.11 are glued into the end cap shells to anchor the anode wire. The anode wire must be precisely located with respect to the end cap shell reference surfaces. This precision is accomplished by performing the end cap final machining operations after the injection molded assembly is glued into the end cap shell. This enables us to drill the hole for the CERN feed through in the same operation that is used to precisely machine the end cap reference surfaces. The injection molded assemblies utilize insulated receptacles to encapsulate the sharp corners at the ends of the field shaping electrodes so that the electric field remains constant even as it approaches the end caps.

6.3.3 Contact Springs

Tin plated copper beryllium springs (Figure 6.12) are located within the insulated receptacle described in Section 6.3.2. These springs are used to provide the electrical connection to the field shaping electrodes. Identical springs are also used to provide a ground connection for the circuit card described in Section 6.3.4.

6.3.4 Electrical Components

The G-10 circuit cards shown in Figure 6.13 are glued to the injection molded pieces before they are inserted into the end cap shell. The first circuit card contains the electrical components necessary to provide the high voltage input for both the field shaping electrodes and the anode wire. This card also contains a low pass filter to protect against any noise which may be on the high-voltage lines. Two resistors are also installed on this card to provide a "Z_0" signal termination and limit the supply current in the event of a tube failure. An RF pulse transformer is included at the signal end to match the tube impedance to the transmission line impedance and couple the coaxial tube to the twisted pair (reject common modes). The second G-10 circuit card decouples the signal from the anode wire high voltage and provides the output connection for this signal. A description of the end cap electronics is given in Section 4.2.3.

6.3.5 CERN Feed Throughs

The CERN feed through shown in Figure 6.14 is used to anchor the anode wire under controlled tension. This is accomplished by feeding the anode wire through the tube and both end caps. One end cap is then glued to the tube and its feed through is crimped. The second end cap is then glued in place and the anode wire is then tensioned and the feed through crimped. After the CERN feed throughs are crimped into position the shunt connector shown in Figure 6.15 is used to make the electrical connection between the feed throughs and the G-10 circuit cards.

6.4 Anode Wire

The field shaping and non-field shaping options use 50 μm and 150 μm gold plated tungsten anode wire, respectively. The wire is plated with a nickel flash and then plated with gold to 1-3 percent of the wire weight.

6.5 Gas Fitting

The brass barb gas fitting shown in Figure 6.16 is used for both the field shaping and the non field shaping options.

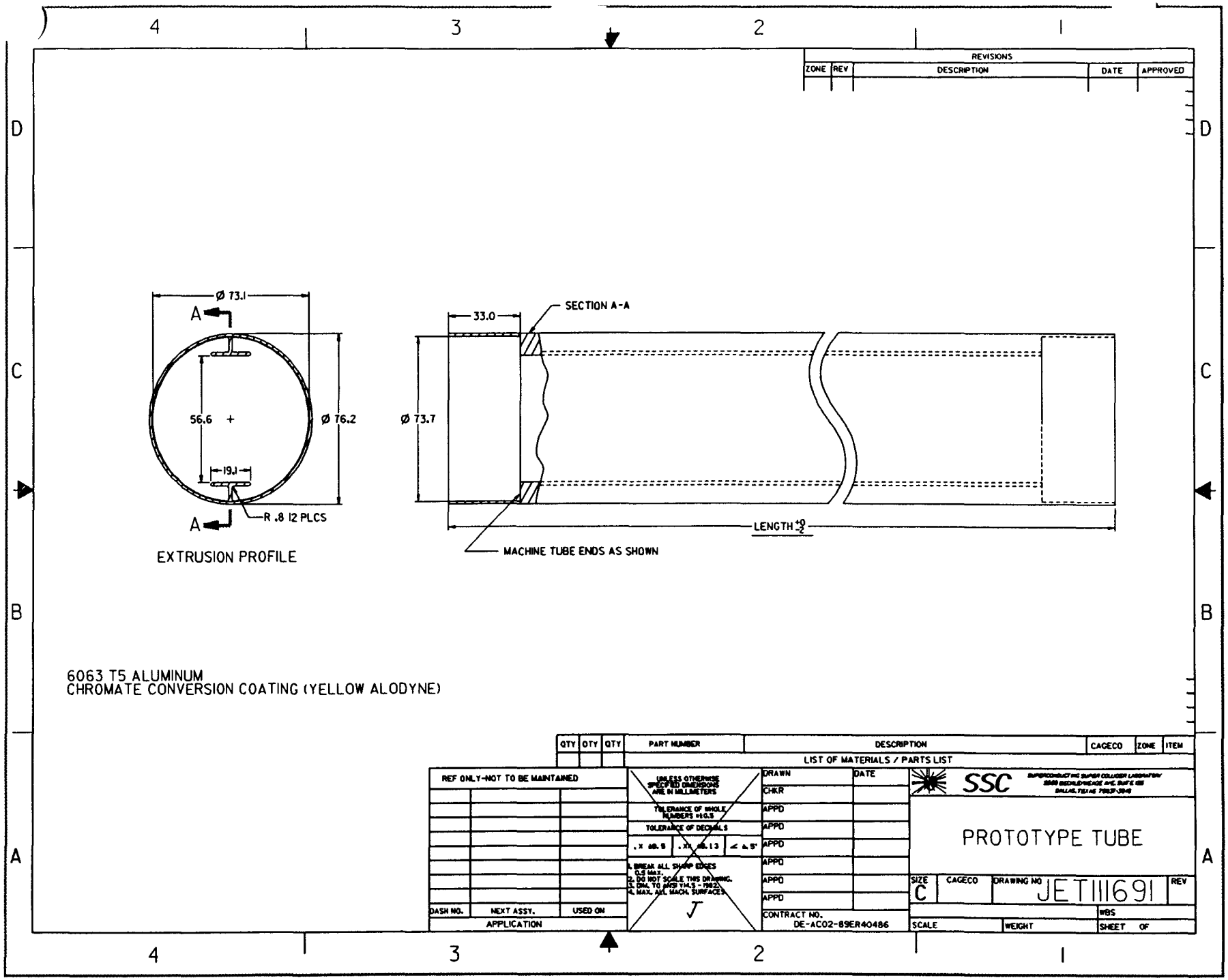

Figure 6.1. Field shaping electrode option extruded tube.

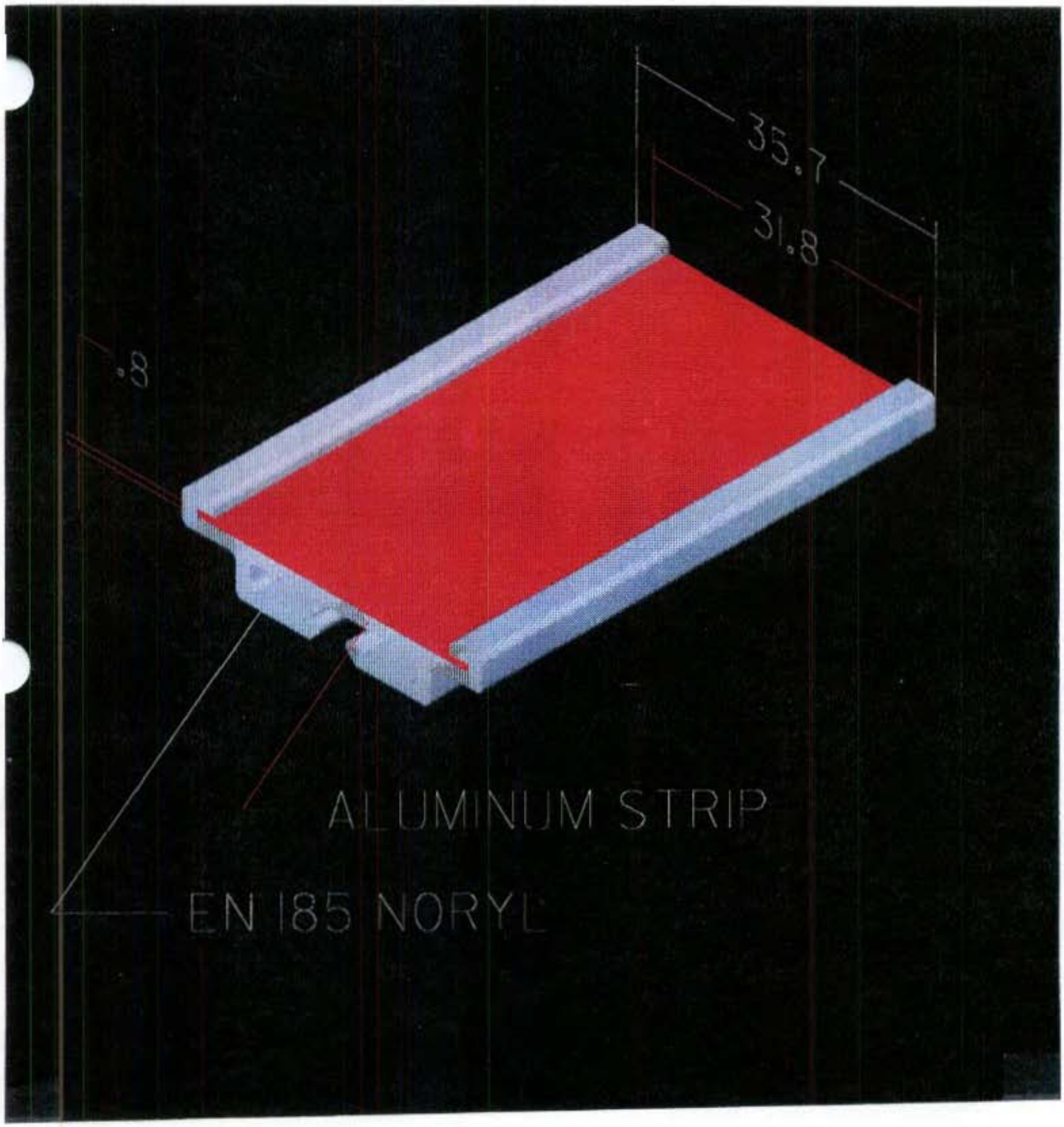

Figure 6.2. Noryl/Aluminum coextrusions.

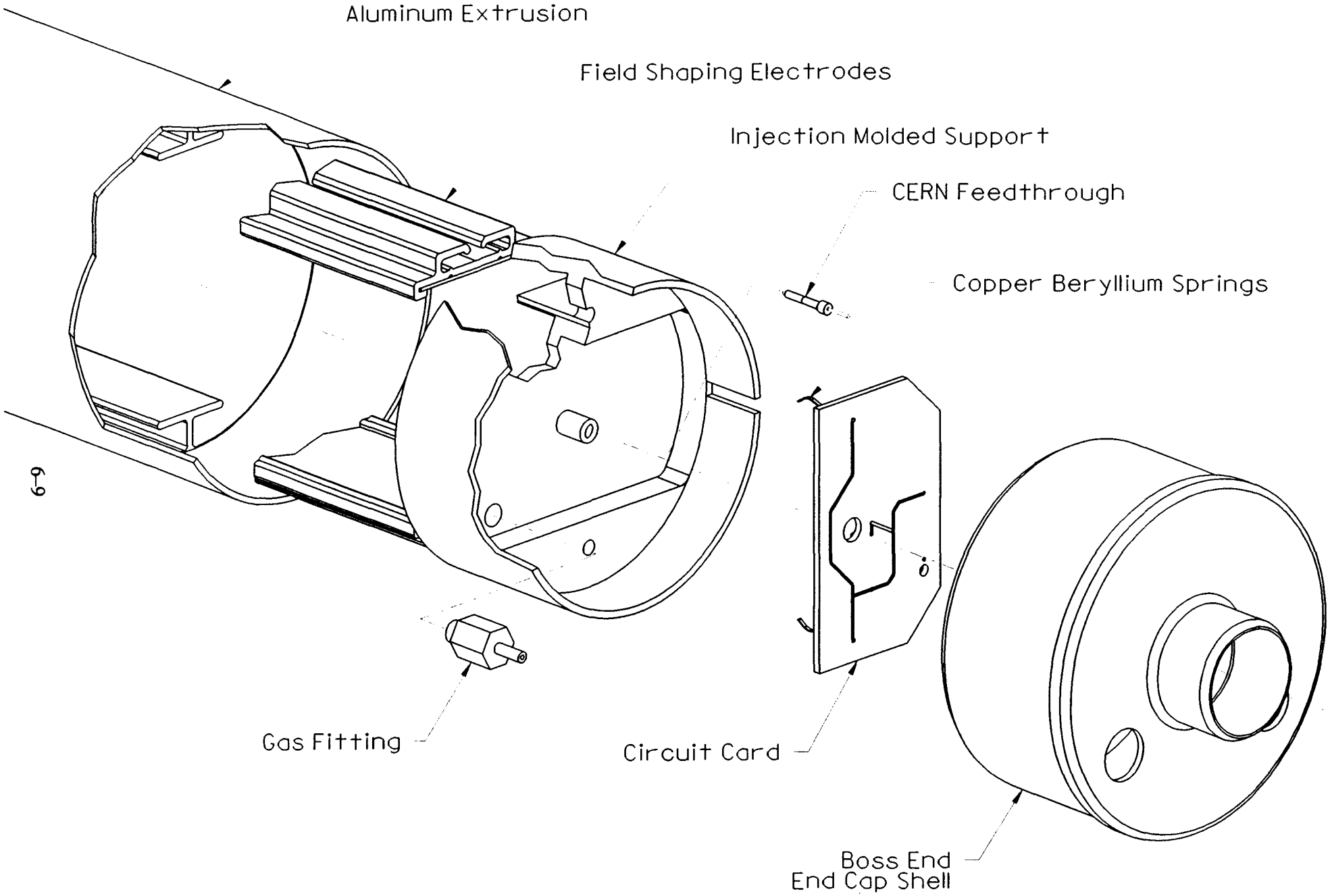

Figure 6.3. Drift cell, boss end exploded view.

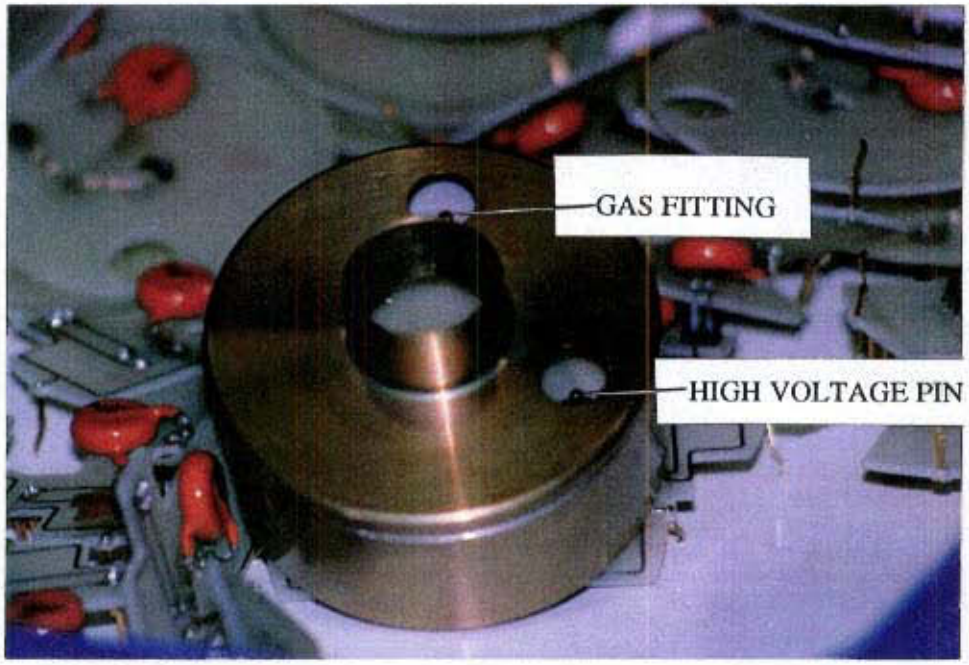

Figure 6.4. Photograph of boss end end cap.

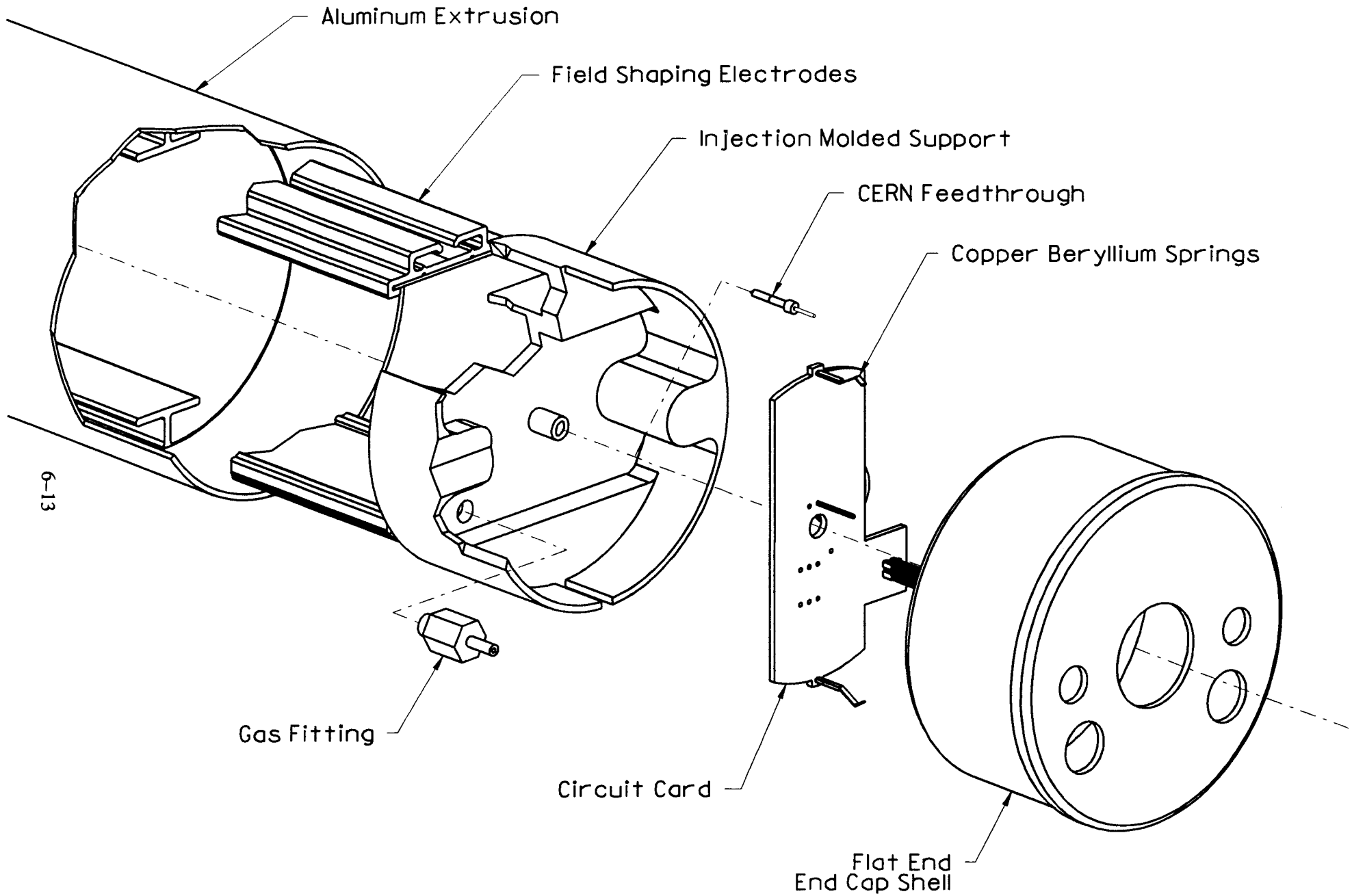

Figure 6.5. Drift cell, flat end exploded view.

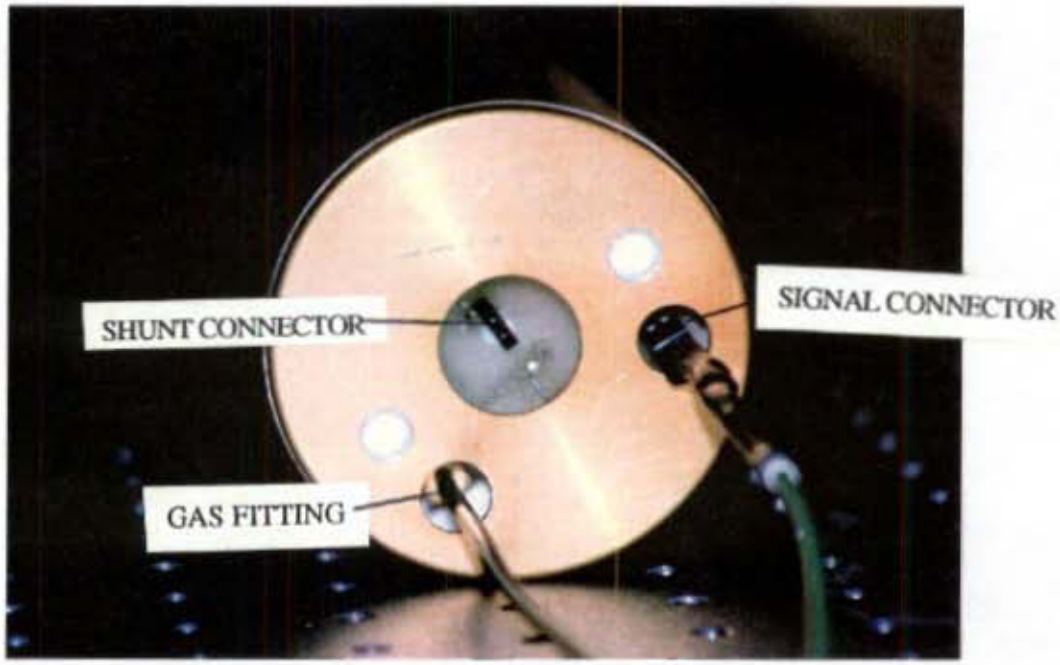

Figure 6.6. View of flat end of an assembled tube.

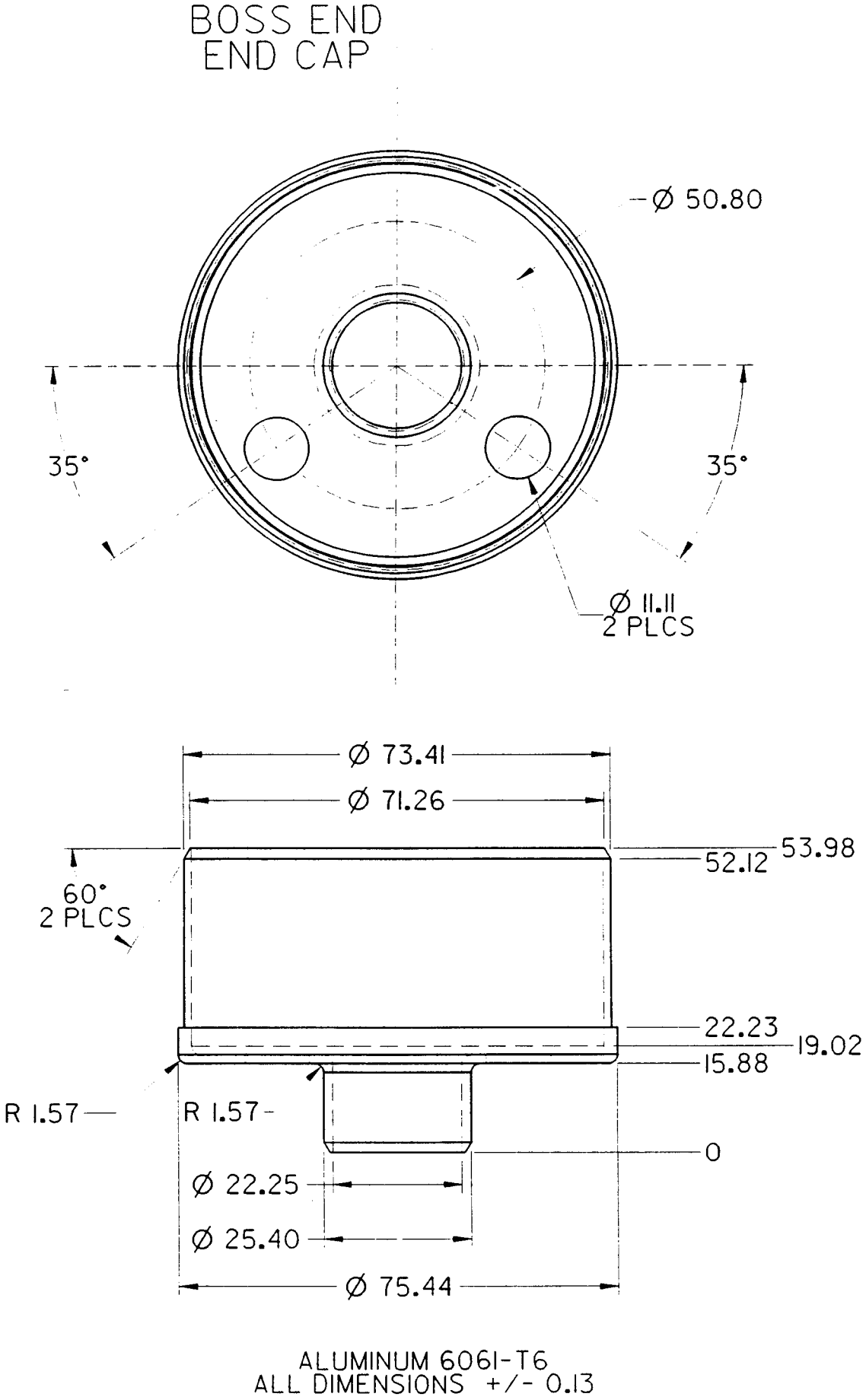

Figure 6.7. Boss end end cap shell.

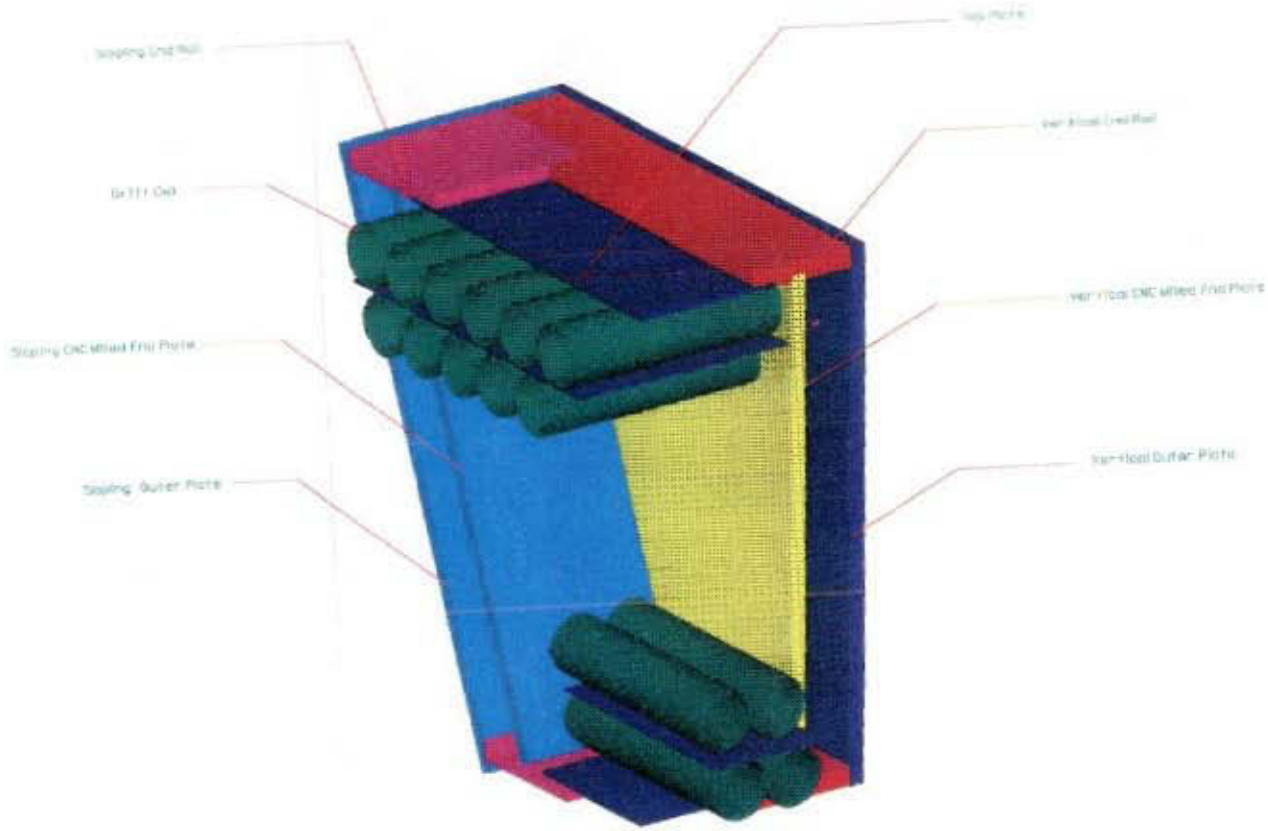

Figure 6.8a. Drift cell installation.

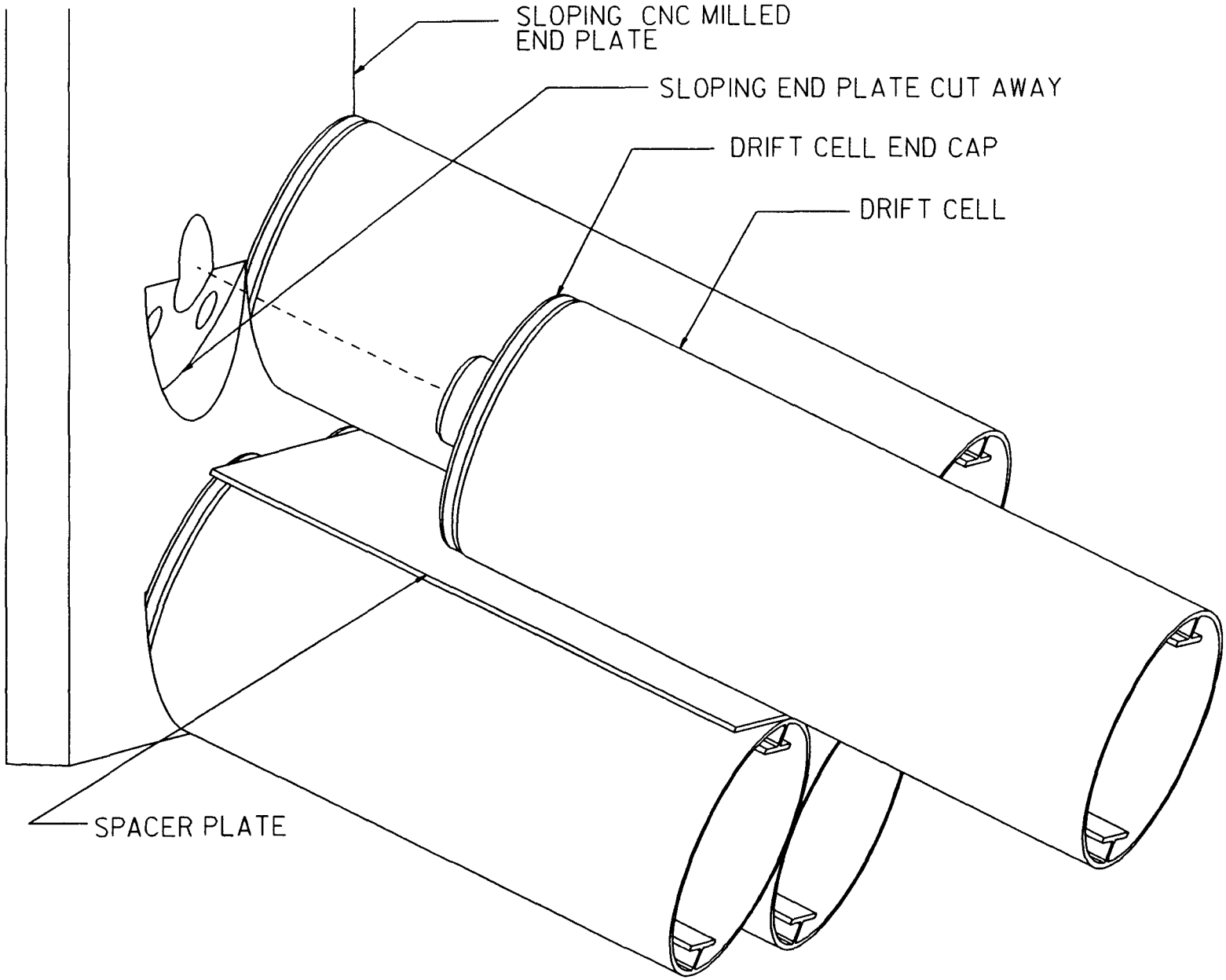

Figure 6.8b. Boss end installation.

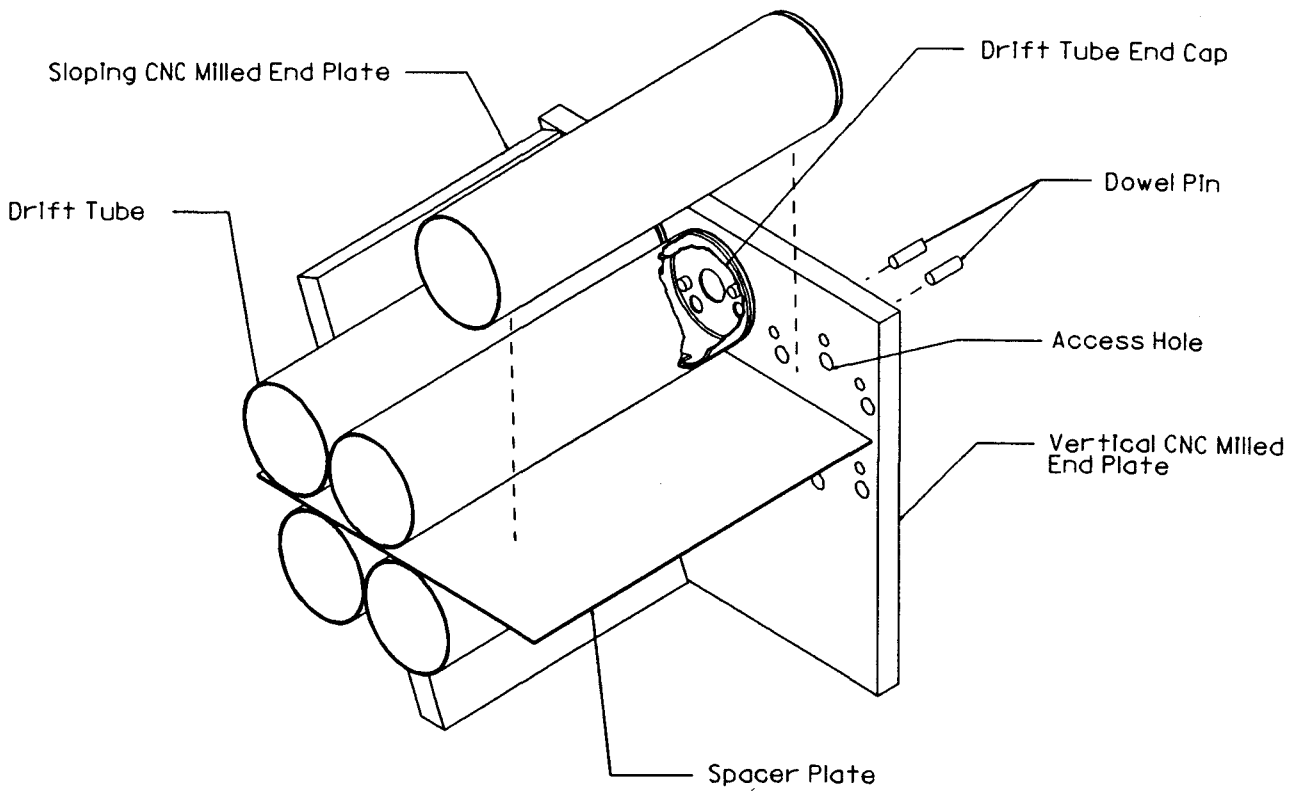

Figure 6.8c. Flat end installation.

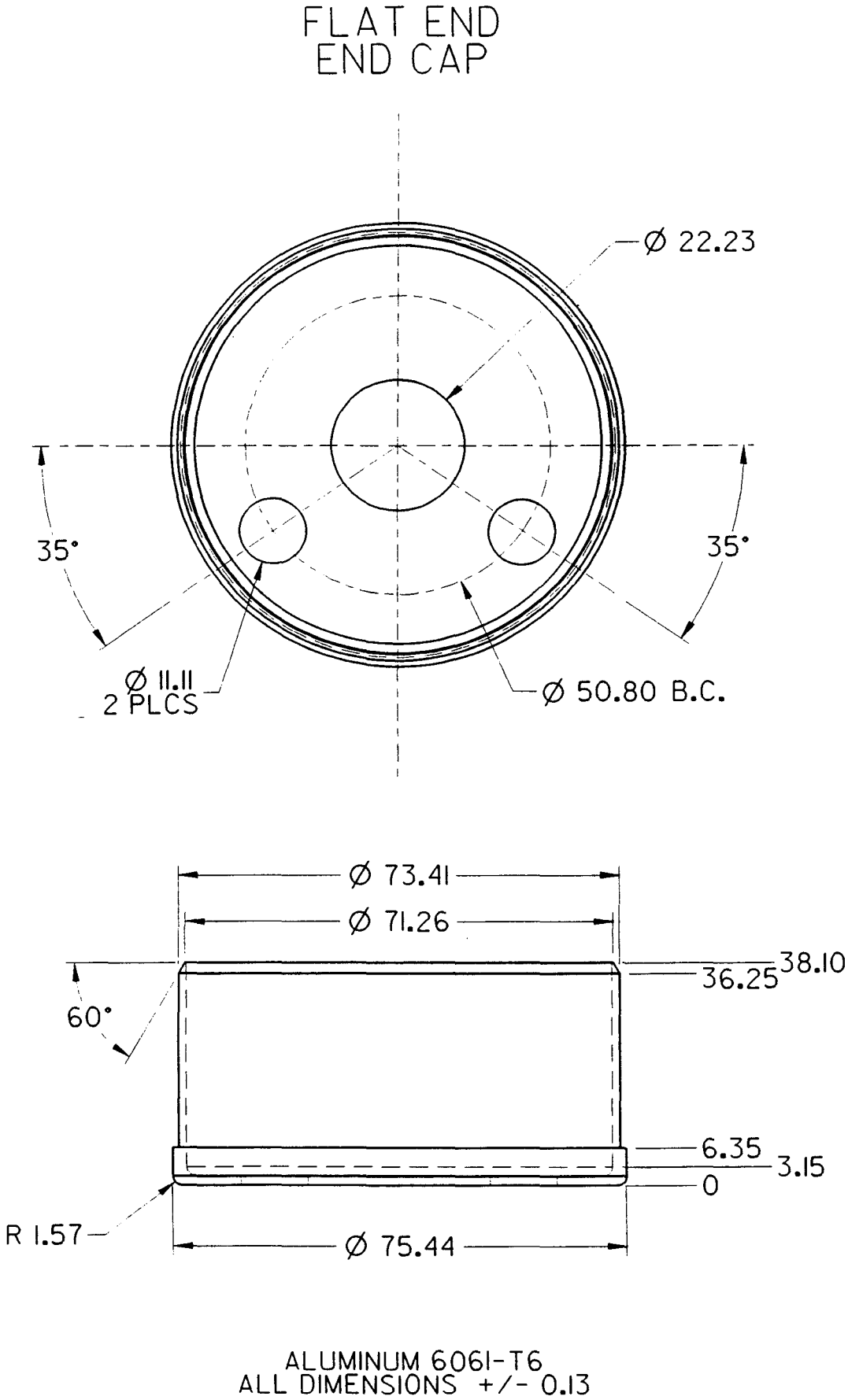

Figure 6.9. Flat end end cap shell.

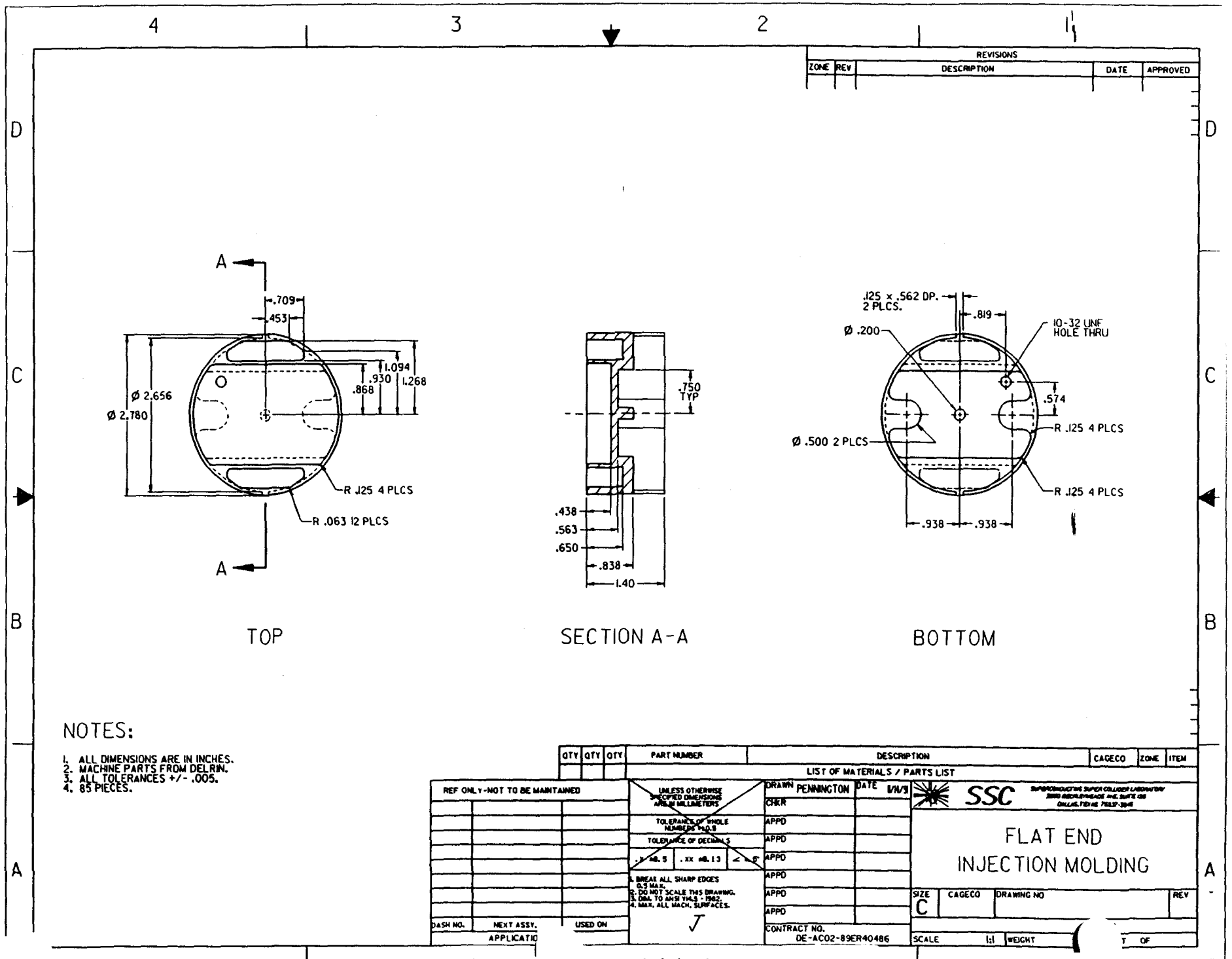

Figure (flat end injection molding.

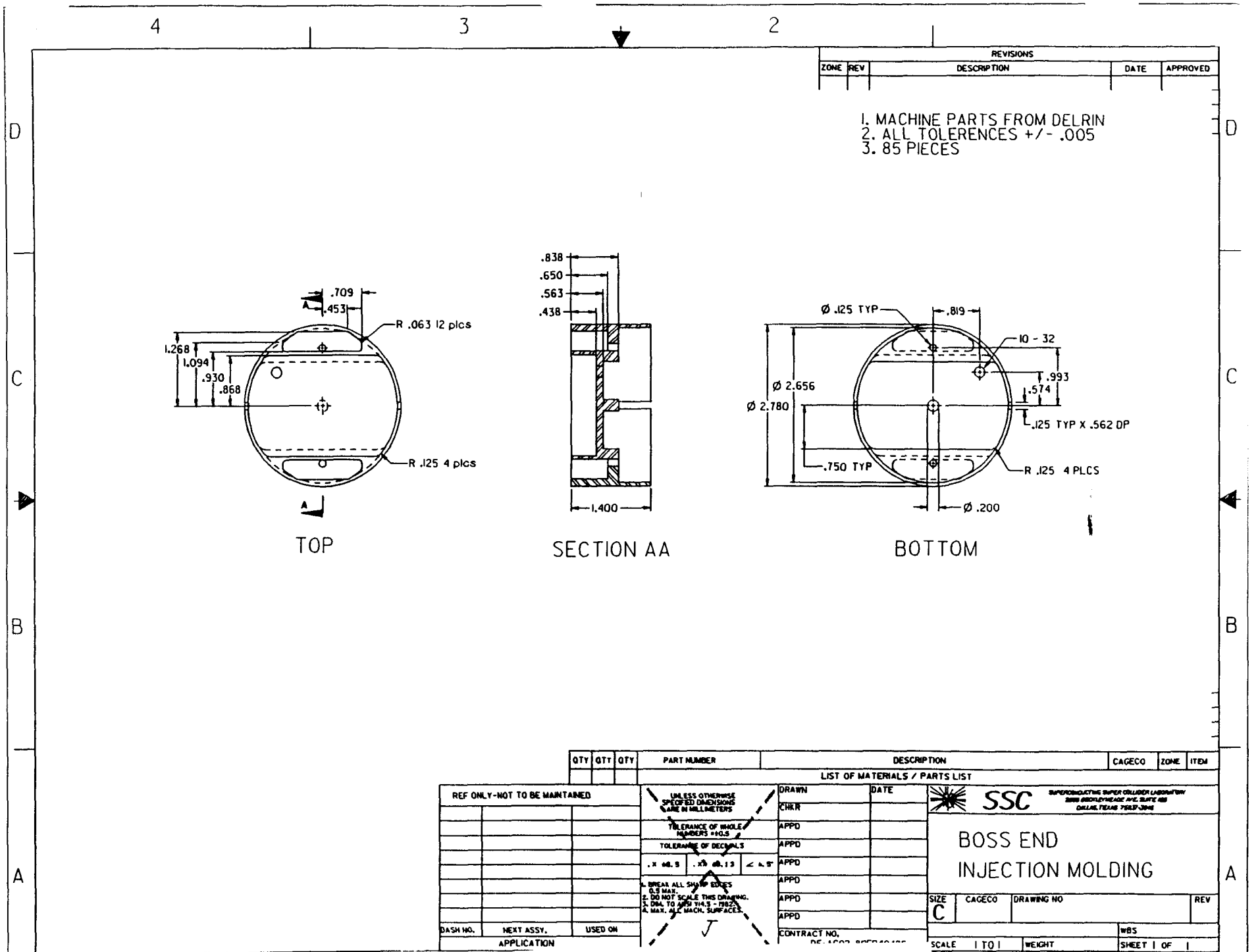

Figure 6.11. Boss end injection molding.

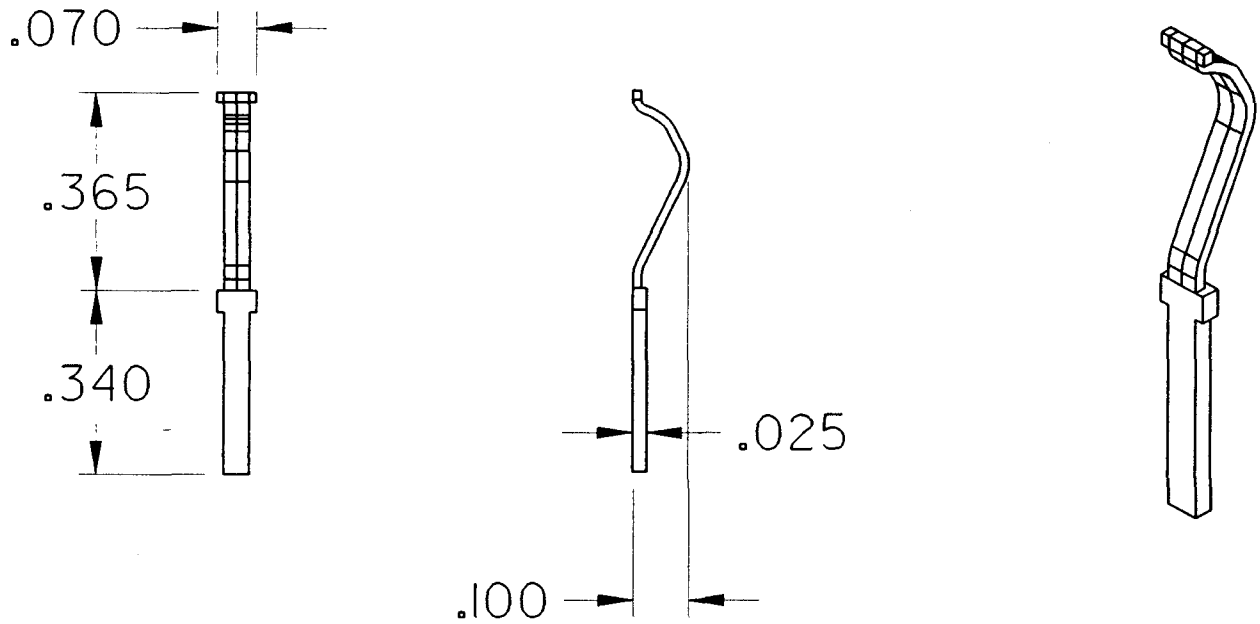

MATERIAL: BRIGHT TIN PLATED
COPPER - BERYLLIUM

Figure 6.12. Copper beryllium springs.

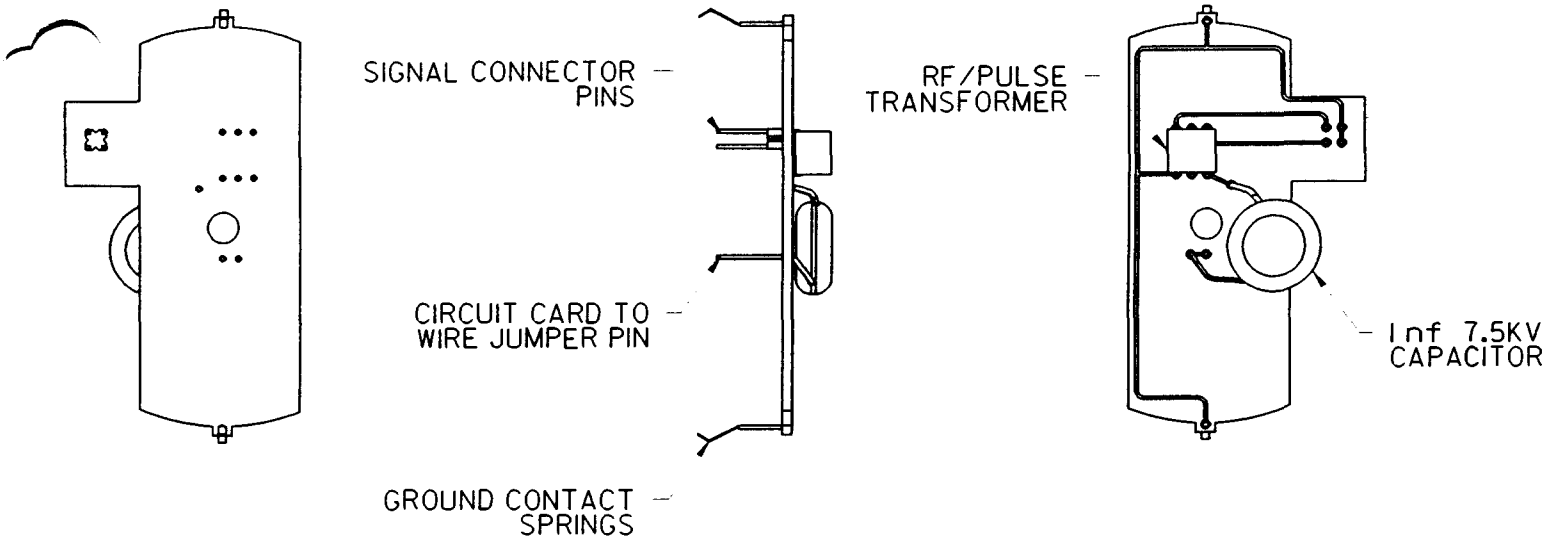

FLAT END CIRCUIT CARD

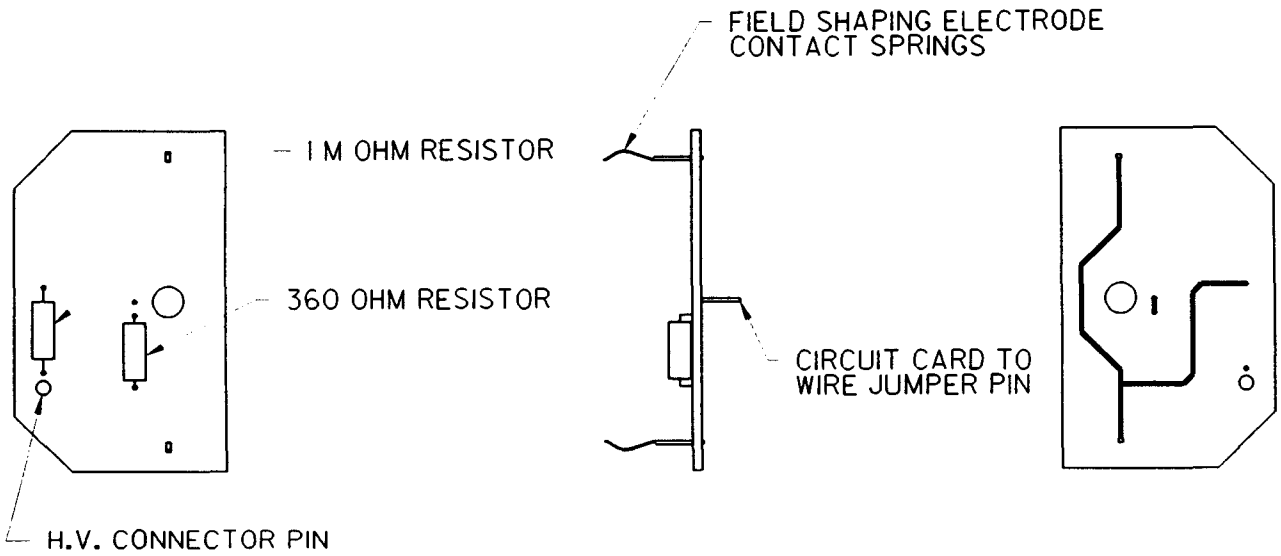

BOSS END CIRCUIT CARD

Figure 6.13. G-10 circuit cards.

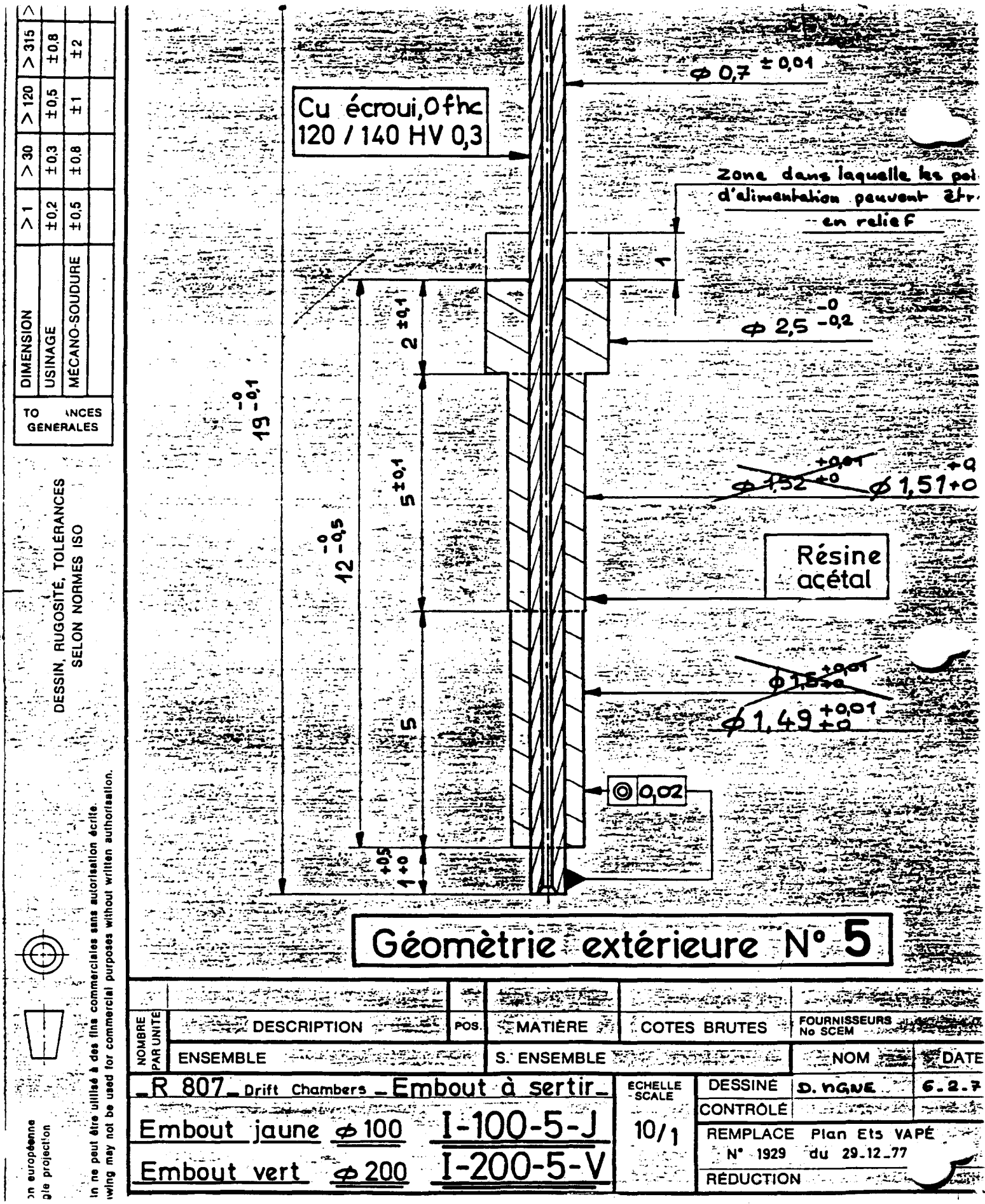

Figure 6.14. CERN feed through.

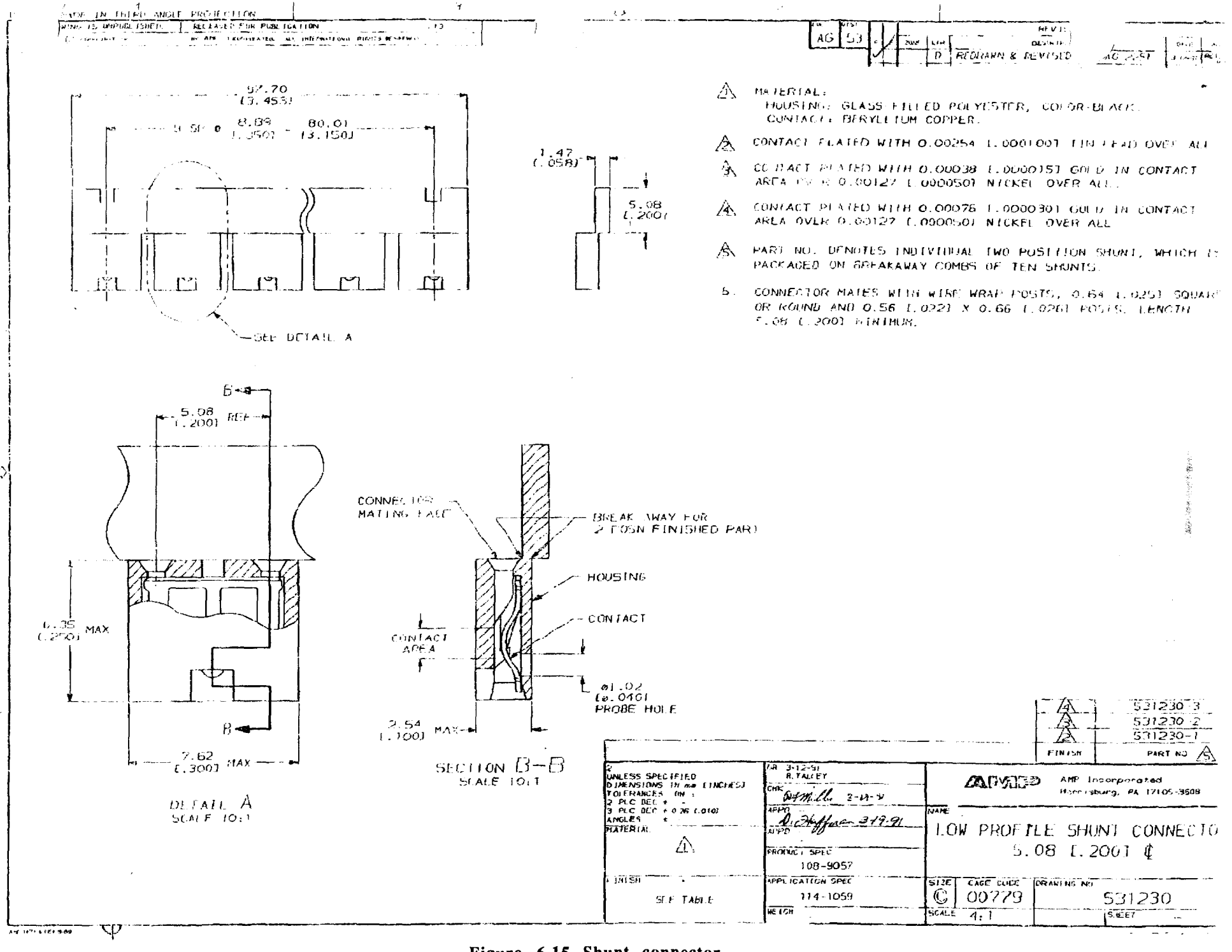

Figure 6.15. Shunt connector.

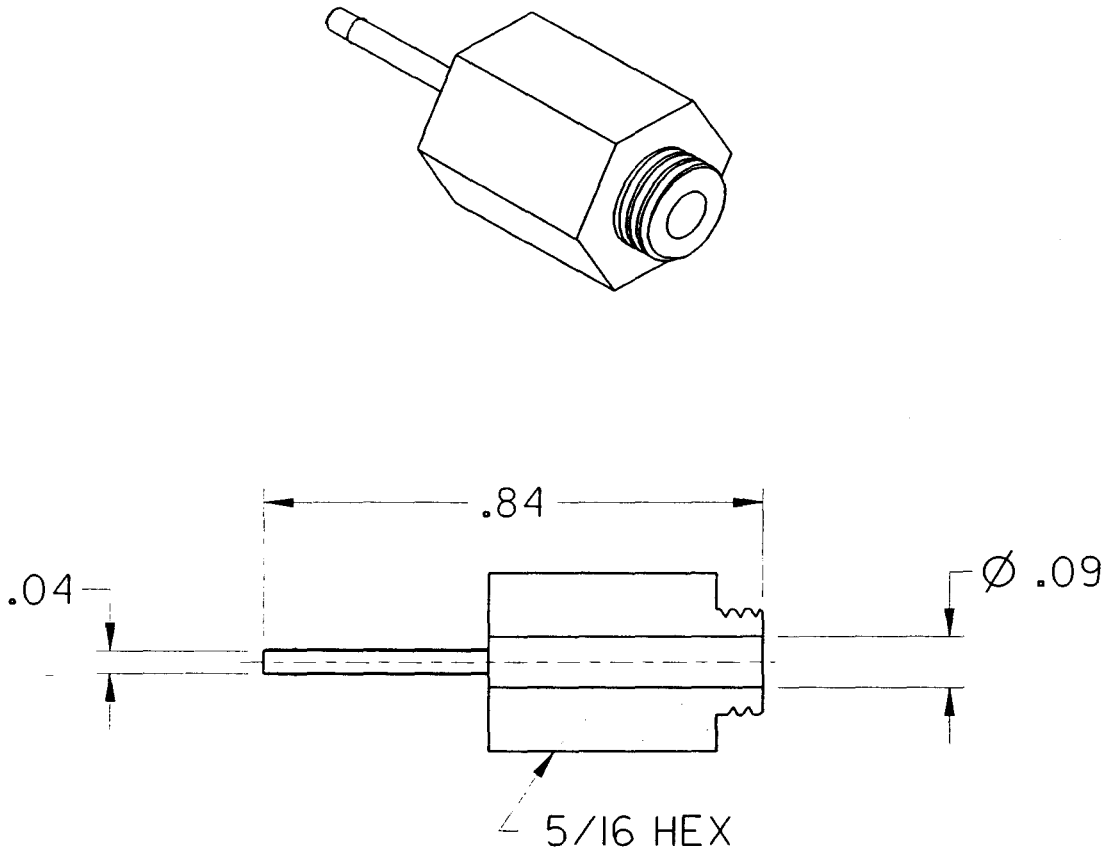

Figure 6.16. Gas fitting.

7.0 ALIGNMENT

7.1 General

There are two distinct aspects to alignment: placement and measurement. We are concerned with these aspects both in the relation of the wires to the module coordinate frame and in the relation of that frame to the global coordinate system. Placement concerns the task of placing the wire as close to the intended position as possible, while measurement concerns the calculation of the discrepancy between the intended and real position.

For the purposes of surveying (with respect to the overall coordinate system of the detector), position sensors are mounted on each module. Prime elements amongst the sensors are "fenceposts". These provide straight line references which run all the way from the central tracker (through the numerous layers of the central detector) to beyond the outermost muon detector. The fencepost comprises of a series of optical elements strung out along a line. The accuracy to which we know the global position of the module's coordinate frame is determined by the accuracy of the sensors and the accuracy to which the positions of the posts are known.

The position of the module's coordinate frame is determined by the rails on which it is mounted. The location of the rails themselves will vary over time as the toroid moves under load. All of the muon chamber designs are subject to these global distortions, which must be measured.

The placement accuracy is determined by the precision of the initial construction and by the departure from that initial state caused by mechanical distortions produced by gravitational forces and/or thermal effects.

The accuracy to which we measure, or know the position of the wires in the coordinate frame of the module is limited by numerous factors. These include the centering of the wire in the feed through, the centering of the feed through relative to the endcap reference surfaces, the comensuration of those surfaces to the mating surfaces in the endplate, and the accuracy on the position of the mating surfaces relative to the neighboring survey targets.

7.2 Wire to Module Alignment

The wires are located by CERN feed throughs. The placement of the feed throughs and the dimensions of the feed throughs themselves have been measured to have a statistical uncertainty well below 10 μm.

The main positioning uncertainties in establishing the wire position with respect to the module coordinate system are:

The relation of the wire to the hole in the feed through	12 μm
The relation of that hole to the outer surface of the feed through	<10 μm
The relation of the outer surface of the feed through to the hole in the end cap	12 μm
The relation of the hole in the end cap to the reference surface in the end cap	12 μm
The relation of the reference surface in the end cap to the mating surface (hole) in the end plate	12 μm
The relation of the holes in the end plate to the local survey holes in the end plate	12 μm
The relation of the local survey targets to their locating holes in the end plate	12 μm
RMS uncertainty	32 μm

7.3 Module Alignment

The mechanical precision with which an individual wire can be located with respect to the coordinate frame of the module is tightly controlled in the present design. All reference and locating surfaces are established by a CNC mill, lathe or survey to 12 μm precision. The procedure required for the above can be summarized as consisting of five main steps:

(i) relating the relevant portion of the wire to the endpoints of that wire;

(ii) relating the endpoints to specific points on the module which serve to define its position;

(iii) relating the specific points on the module to an array of survey devices mounted on the toroid iron, which collectively establish a space frame;

(iv) linking the space frame to the central tracker;

(v) linking the space frame to fixed reference points in the experimental hall.

The module design puts the alignment emphasis on the placement accuracy of a computer controlled mill, and everything else is arranged to preserve that accuracy. All of the proposed designs rely on the precision of NC milled panels for the relative placement of neighboring drift cells. This design is distinct in using single, large panels rather than multiple small panels across the width of a module. This extends the placing accuracy across the whole module, unhindered by errors in the alignment of the subpanels. (The ultimate placement accuracy of a CNC mill is ~10 μm.) The bending of the panel, however, becomes a significant consideration for a long panel. This bending, like the sag of a wire, is very orderly. A very few parameters suffice for its description. These parameters will be continuously monitored by a combination of thermometers and "optical straight edges".

The module is built in an unstressed condition on an assembly table. During the fabrication, the straightness and alignment of the endplates will be established and maintained by jigs to close tolerances of approximately 20 μm. At that time the optical straight edges will be installed and the reference reading made. Once the module is removed from the assembly table, it will flex and bend from the applied stresses. The monolithic module construction provides great rigidity and makes the distortions both small and orderly. Although the distortions are calculable, we do not rely on the calculations alone. The deflections are continuously monitored with the optical straight edges. The distortions of interest are the overall linear scale change due to the thermal expansion of the aluminium and the distortions due to the thermal gradients in the plane of the module. Both are monitored from the temperature measurements. The coefficient of thermal expansion of aluminium is 24 ppm/°K, and the length of a module is about 10 m, thus to measure the temperature to 0.1°C is appropriate.

Temperature gradients normal to the plane will induce bending or twisting of the module. These distortions, like the distortions from mechanical stresses will be monitored by the optical straight edges. These devices will be mounted along all four edges and across the diagonals of each module. The former monitor bending, the latter skew.

7.4 The Optical Straight Edge

The optical straight edge comprises a laser diode, focusing lens and a position sensor (quadrant photodiode). The principle is such that if the three elements are spaced so that the image of the light is focused upon the quadrant detector, and if, indeed the optical centers of the three lie along a straight line, then the photocurrents will balance across both cuts of the detector. If the three are slightly out of line, then the currents will not be equal in a manner which will indicate the sense of the misalignment. The device in this form is a null detector.

The laser diode is effectively a point source. The diameter of the diffraction image at the quadrant is 50–100 μm. The intrinsic resolution achieved is at the micron level.

In order to make use of a null detector, one must have some means of adjusting to null. This may not always be practical, in which case one would want to measure how far the image was from the center. To do this properly, one would substitute a video CCD for the quadrant detector and some extended structured sources for the laser. The proportional response of the quadrant detector can be used to obtain a position measurement, albeit over a very short range. The range can be extended in a variety of ways, but at the expense of resolution and accuracy.

7.5 Creating a Space Frame

The optical straight edge defines three points (light source, lens and quadrant detector) in a line. It is simple to extend to 4, 5, ... points. By using a mirror we can also define a deflected direction. This has the inconvenience that the deflection angle is sensitive to the angular position of the mirror. The problem is overcome by replacing the mirror with a prism which bends the light by 112.5 degrees (a penta prism can be made which will do this). Thus we can relate the octagonal sections within a BWn layer. Further the "wormholes" advocated by D. Eartly provide paths that penetrate through the BW layers all the way from the central tracker to the walls of the experimental halls. We also have line-of-sight paths available in the space between BW2 and BW3 which run the full length of the toroid and beyond. We thus can create a three-dimension mesh of lines which we survey during the construction phase and to which we relate all of the modules and other detectors. The position of the central tracker relative to the mesh can be well monitored as can the relation of the mesh to the hall.

The reference for the detector and the physical objects which define our straight edges is the toroid iron. The iron moves, particularly when the magnetic field is turned on or off, and everything moves and all of the images in our straightedges move in relation to the detectors. From these shifts we can redefine the structure providing we have some invariant base to start from. Perhaps the central tracker is stable as a unit. One could work out from there assuming it remained fixed and then rotate the whole coordinate system if it did not match with the hall definition of the beam direction.

7.6 Verification of the NC Milled End Plates

The end plates on the prototype are representative of a short section of the plates used on a full size module. They are used to locate four layers containing a total of 30 drift tubes. In order to gain insight into the accuracy achievable for the hole location and the hole diameter, these plates were inspected using a BROWN & SHARPE coordinate measuring machine (CMM), see Figure 7.1. This system is a very high precision 3-axis robot which can be programmed to move a sensitive measuring probe in any desired pattern. The CMM is located in a temperature controlled room, and allows the measurement of the x, y and z coordinates of any desired points on an object with an absolute maximum error of 4 μm, within a measuring volume of approximately 0.6 m^3.In order to measure the location and diameter of a hole, the CMM is programmed to make a number of measurements around the circumference. It then calculates the best fit to a circle and reports the diameter and the center coordinates. As an example of the precision achieved and the measurement systematics, one end plate was inspected on two separate occasions. Measurements in the x-direction (across the plate and along a row), showed very satisfactory results: the first measurement gave an error of 4.05 μm and σ = 3.93 μm. This is essentially the resolution limit of the CMM. It is worthwhile to note that the preceeding error and standard deviation reflect the difference between the design and measured values of the hole locations. The second measurement showed larger errors, but these were found to be non-random, increasing linearly across the plate to a maximum of 15 μm. This is interpreted as a temperature difference (~ 1°C) between the two measurements. In the orthogonal direction (i.e., y-direction, from row-to-row), errors of up to 49 μm were observed. Again, these were found to be non-random, and can be explained by the fact that the plate was not perfectly flat. The plate is clamped to a flat jig surface during machining, but was not clamped down on to the CMM.

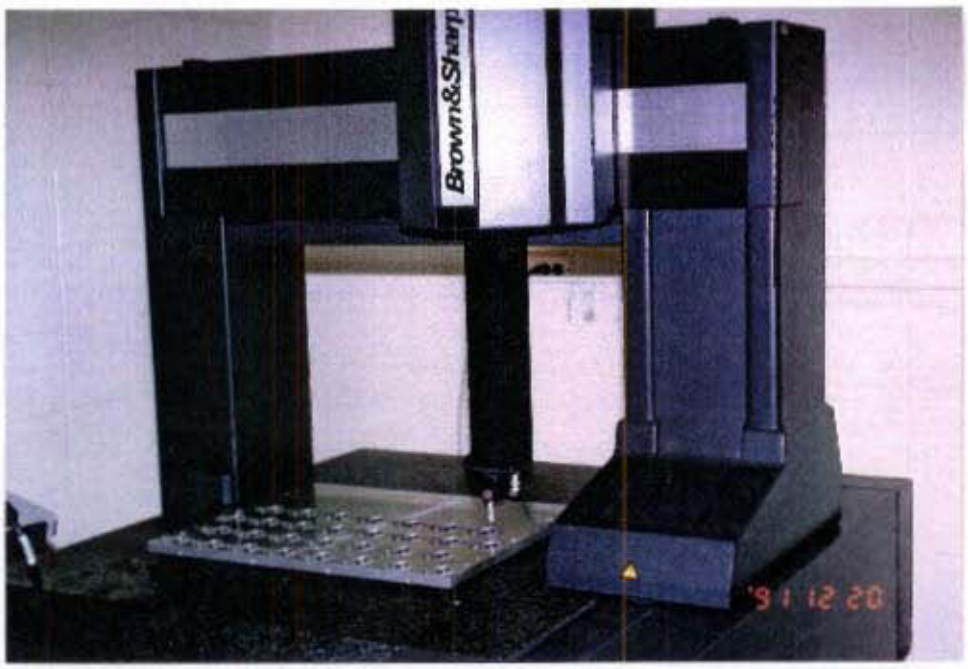

Figure 7.1. Photographs showing the BROWN & SHARPE coordinate measuring machine used to determine the location of the holes and the hole diameter on the end plates.

8.0 MANUFACTURING PLAN

8.1 Manufacturing Approach/Philosophy

Fabrication, assembly and installation of the muon chambers will be accomplished at various universities and the SSC Laboratory with support from private industry which may be required due to production quantities, facility, equipment, or process requirements. It is intended that manufacturing costs will be minimized through the utilization of: (1) "state of the art" manufacturing processes and automated equipment available in industry for fabrication of details and subassemblies, (2) university labor for assembly of the drift cells, and (3) SSCL labor for module final assembly. The source for major details and assemblies is shown below:

Detail/Assembly	Source
Circuit Board Assemblies	Industrial Fab
Injection Molded Plastic Support	Industrial Fab
Formed End Cap Shells	Industrial Fab
End Cap Assemblies	Industrial Fab
Anode Wire	Industrial Fab
Electrodes	Industrial Fab
Drift Cell Tubes	Industrial Fab
End Plates, Machined	Industrial Fab
Edge Members	Industrial Fab
Outer Support Plates	Industrial Fab
Top & Bottom Panels	Industrial Fab
Spacer Sheets	Industrial Fab
Drift Tube Assemblies	University Labs
End Plate Assemblies	SSCL
Module Assemblies	SSCL

A Manufacturing Sequence Flow Plan reflecting the above sources and the following manufacturing plan, is shown in Figure 8.1.

8.2 Manufacturing Description

8.2.1 Circuit Boards

Circuit board assemblies described in Section 6.3 of this report, will be purchased complete from industry. These boards will be printed and drilled with numerically controlled equipment, electrical components mounted and wave soldered complete. Upon completion the circuit boards will be shipped to another vendor for assembly into the end cap shell.

8.2.2 Injection Molded Plastic Supports

Plastic injection moldings featuring pockets which fit around the electrodes inside the chamber tube, will be used in each end cap assembly configuration to provide a mounting surface for the circuit card assembles, material for a press fit wire feed through fitting, and a gas seal for the wire chamber assembly. The moldings will be purchased from industry and sent to the end cap assembly vendor for installation with the circuit board assemblies into the end cap shells.

8.2.3 End Cap Shells

Two end cap shells will be formed from aluminum with some machining to final configuration after assembly with the circuit boards and molded plastic supports. This machining is necessary due to close tolerance necessary due to tolerance requirements. One end cap shell, which will be referred to as the "boss end cap" (Figure 6.7), will be fabricated by stamping to form the shell and 25 mm boss while simultaneously blanking two 11.11 mm diameter holes which provide inlets for gas and high voltage electrical connections. The other end cap shell, which will be referred to as the "flat end cap" (Figure 6.9), will be fabricated by stamping to form the shell and simultaneously blanking one 22.23 mm diameter hole to provide access for installation of the wire feed through, and one 9.5 mm diameter hole for the signal connection. Completed end cap shells will be shipped to a separate vendor for final assembly, and where they will also be machined to final configuration after assembly in order to hold concentricity and dimensional tolerance requirements.

8.2.4 End Cap Assembly

The circuit board assemblies will be assembled with the injected plastic moldings by glueing. These assemblies will then be glued inside the end cap shells to make up the boss end cap and the flat end cap assemblies. The 73.41 mm O.D., 25 mm boss, and a press fit hole for the CERN wire feed through will then be machined on the boss end cap assembly. The flat end cap assembly will also be machined to provide the 73.41 mm O.D., a press fit hole for the CERN wire feed through, and two (2) 9.5 mm diameter dowel holes for alignment and support. Upon completion of the assembly and machining operations, the end caps will be shipped to university labs for installation into the drift cell assemblies.

8.2.5 Electrode Extrusions

The field shaping electrodes, which will be required for the field shaping design only, will be fabricated from coextruded Noryl with an embedded thin alodyned aluminum strip. The extrusions will be cut to length by the vendor and shipped to university labs for installation into the drift cell tubes.

8.2.6 Drift Cell Tubes

The drift cell tubes will be fabricated from purchased aluminum tube extrusions. An extrusion vendor will machine the tubes to length, have them alodyned and then ship them to university labs for final assembly. The field shaping design tubes will feature opposing tee shapes inside which will support the electrodes. The length and inside diameter of both ends of the tube will be machined simultaneously. The tee shapes of tubes with field shaping will be machined simultaneously with the length and inside tube diameter to allow clearance for installation of the end cap assemblies. The non field shaping tube design will require machining of the lengths only. Bar codes applied by the vendor will identify part numbers, tube length, etc. Figure 6.1 provides a sectional view of the field shaping tube design.

8.2.7 End Plates

An industrial vendor will fabricate the module assembly end plates from cast aluminum jig plate machining them on CNC equipment and conducting source inspection before shipping them to the SSCL. The industrial vendor will accomplish the following operations:

1. machine of the periphery
2. drill and tap holes for attachment of edge members
3. drill and tap holes required for joining of the end plates at the corners

4. bore survey holes
5. drill and ream jig locating pin up holes
6. machine locating and support holes for the end cap boss (Figure 2.16) and
7. bore dowel holes to orient and support the drift cell assembly at the end with the flat end cap. Conceptual drawings of the end plates are shown in Figures 2.13 and 2.14.

8.2.8 Rails

The rails (Figure 2.17, 2.18) will be aluminum extrusions machined on CNC equipment by an industrial vendor to drill, tap and counter bore bolt holes for attachement to the end plates and outer support plates. The machined extrusions will be trimmed to length before shipment to the SSCL for installation into the module assemblies.

8.2.9 Outer Support Plates

The periphery, access cutouts and attach holes will be CNC machined in the outer support plates by and industrial vendor and shipped to the SSCL for module assembly. These plates will be fabricated from aluminum.

8.2.10 Top and Bottom Panels

The top and bottom panels of the module assemblies will be fabricated from $1524 \times 3048 \times 6$ mm^3 aluminum plate stock by an industrial vendor. Doublers, or splice plates, will be bonded along one edge and one end of each plate and will extend past the edge of the plate to provide a surface for bonding to adjacent plates upon final assembly of the modules.

8.2.11 Spacer Sheets

Thin aluminum space sheets will be bonded between each layer of drift cells. The sheets will be purchased cut to size from industry.

8.2.12 Drift Tube Assembly

Final assembly of the wire chamber will be accomplished at university labs. The field shaping electrodes will be installed in the tubes by manually sliding the Norel extrusion onto the tee shape inside the tube for the full tube length. The tube/electrode assembly will then be positioned on an assembly table that will have a wire spool and tensioning device on one end. The wire will be threaded first through a feed through, the CERN feed through fitting, and the flat end cap assembly. It will then be fed the full length of the wire chamber tube where the boss end cap assembly and another wire feed through fitting will be added. The feed through fitting at the flat end cap will then be crimped onto the wire and installed into the end cap. Slack on the wire will then be taken up and the flat end cap installed in the tube with bonding adhesive. Adhesive will be applied to the boss end cap assembly which will then be installed in the wire chamber tube. The wire will then be tensioned and the feed through fitting crimped at the boss end cap. The completed drift cell assembly will then proceed to a testing station for a electrical continuity check before installation into the modules. The final assembly sequence of the non-field shaping design drift cells will be the same as described above, except electrode installation will not be required.

8.2.13 End Plate Assembly

Before being loaded into the module final assembly jig, the end plates will be pre-assembled with the rail extrusions which will be purchased from an industrial vendor cut to length and with attach holes

drilled and counterbored. The use of CNC for drilling the bolt holes in the rail extrusions and drilling the tapped holes in the end plates will assure a match of the attach hole pattern upon assembly.

8.2.14 Module Assembly

The drift cell modules will consist of two (2) inclined end plates, two (2) upright end plates, top and bottom panels, layers of drift cells with aluminum spacer sheets between each layer, extruded and machined aluminum edge members, and an outer support structure fabricated from aluminum plate. Four work stations will be dedicated to assembly of the module structure, installation of the wire chambers, assembly of modules and super modules. Initially, all four work stations will be dedicated to the assembly of BW1 modules. When assembly of the BW1 modules is completed, two work stations will be used for assembly of BW3 modules, and two work stations will be used for BW2 modules and BW2/BW3 module stacks (super modules). Final assembly fixtures (FAF), which will consist of large flat work surfaces and adjustable locators, will be located at each work station. After completion of BW1 assembly effort the locators on each assembly fixture will be repositioned to accommodate assembly of BW2, BW3, and the super modules. The BW2 and BW3 modules will be assembled in separate work stations and final assembled into "super modules" with a common outer support structure. The BW2 and BW3 modules which will be installed on the bottom octant of the magnet will not be assembled into super modules and will have separate outer support structures.

BW1 module assembly will begin by loading the end plate/rail assemblies into the FAF and joining the plates at the corners with bolts. The bottom panel will then be installed by bonding to the surface provided by the rails (Figure 2.21) and to adjacent panels (see 8.2.10). The drift cell assembles will then be prepared for installation into the modules by application of adhesive at a point tangent to the outside tube diameter and extending the length of the tube. During the adhesive dispensing operation, the drift cell will be held in a lightweight strongback handling fixture which will also be used for handling and alignment of the wire chambers during installation into the modules. Using the strongback, each drift cell will be lowered into position, the 25 mm boss inserted into the locating hole machined into the end plate (Figure 2.16). Two dowel pins are then installed at the opposite end of the drift cell extending through the end plate into the flat end cap. Adhesive will be applied between and to the tops of the drift cell tubes using a special adhesive dispenser that will track along the tops of the tubes. Aluminum spacer sheets will then be placed on top of the tubes weighted down and the adhesive allowed to cure. After the last layer of tubes has been installed., the top panel tiles and rails will be installed. The wiring and plumbing will then be installed, and the required electrical connections will be made. The locators may then be removed from the FAF and the outer support panels installed.

Assembly operations for BW2 and BW3 modules that will be installed on the bottom octant of the magnet steel, will be the same as described above for BW1. The remaining BW2 and BW3 modules will also follow the same assembly operations except they will be assembled into tower modules with a common outer support structure. The outer support plates will initially be assembled on three sides of BW2. A BW3 module, without outer support plates, will then be positioned over the BW2 module, lowered into place and the final outer support plates installed to complete the Tower Module Assembly.

Upon completion, module assemblies are transported to the interaction halls for installation or, they are sent to storage.

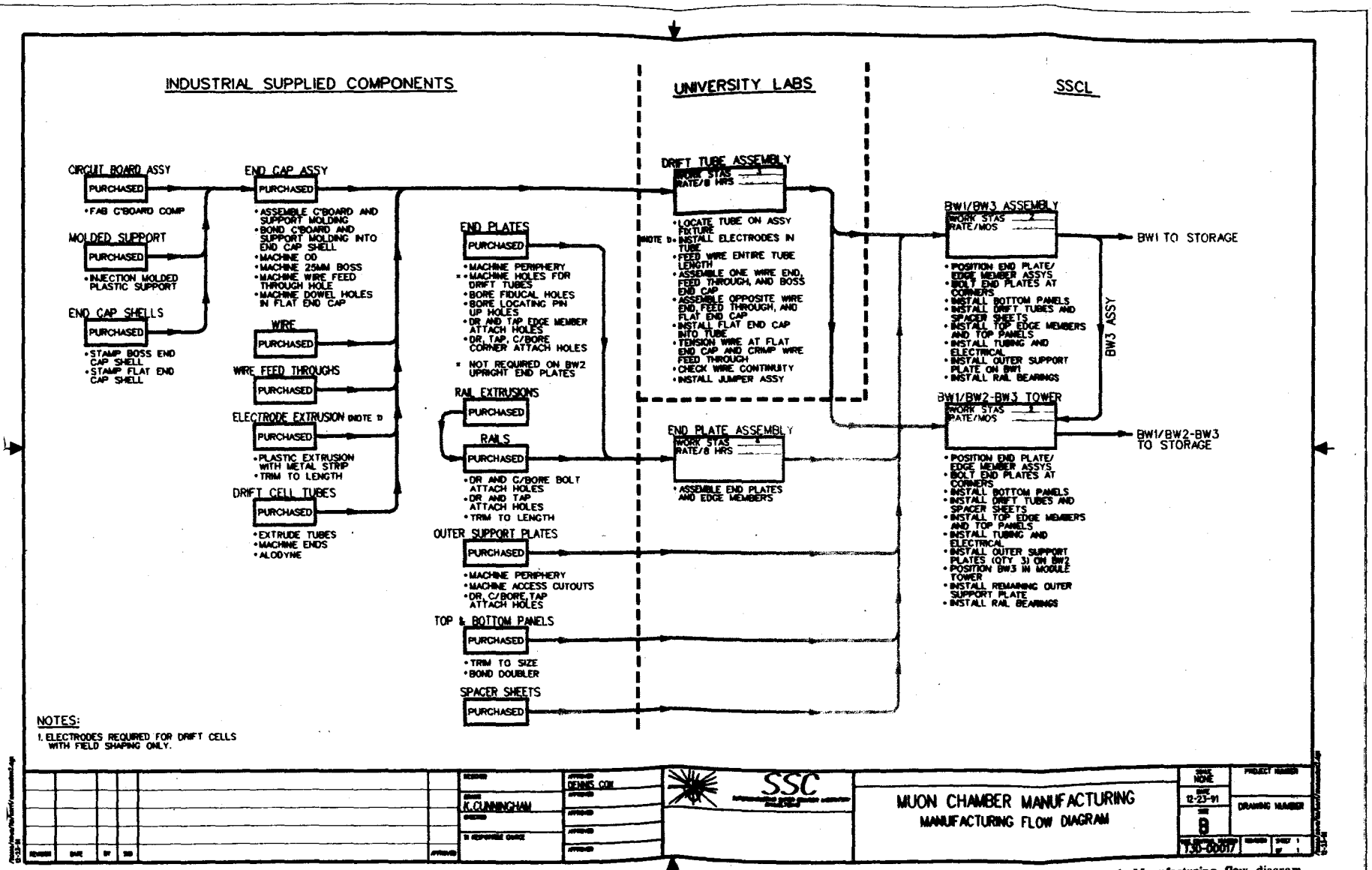

Figure 8.1. Manufacturing flow diagram.

9.0 PROTOTYPE MODULES

We have constructed two 9 m long units, one at the SSCL and one in Seattle, each containing 4 layers of θ tubes and 2 layers of ϕ tubes. The θ tubes are 9 m long and are arranged in four rows containing 8, 7, 8, 7 tubes, respectively. The ϕ tubes are approximately 0.5 m and arranged transverse to the θ tubes. Figure 9.1 shows a corner section of the unit. The SSCL version contains field-shaping electrodes.

We have found that the epoxy seal works very well. The tubes are gas tight. Figure 9.2 shows details of the module end plate before tubes are inserted and the prototype end plate mounted in the CNC mill. Figures 9.3a,b show some close-up views of the "pockets" machined in the end plate. Figure 9.2c,d,e show a tube inserted in the end plate (9.2d shows the backside of the plate with the boss end in place). Measurements of cosmic ray muon tracks are in progress.

We also have constructed a 4×4 ft^2 module with one row each of θ, ϕ and stereo tubes to test assembly procedures.

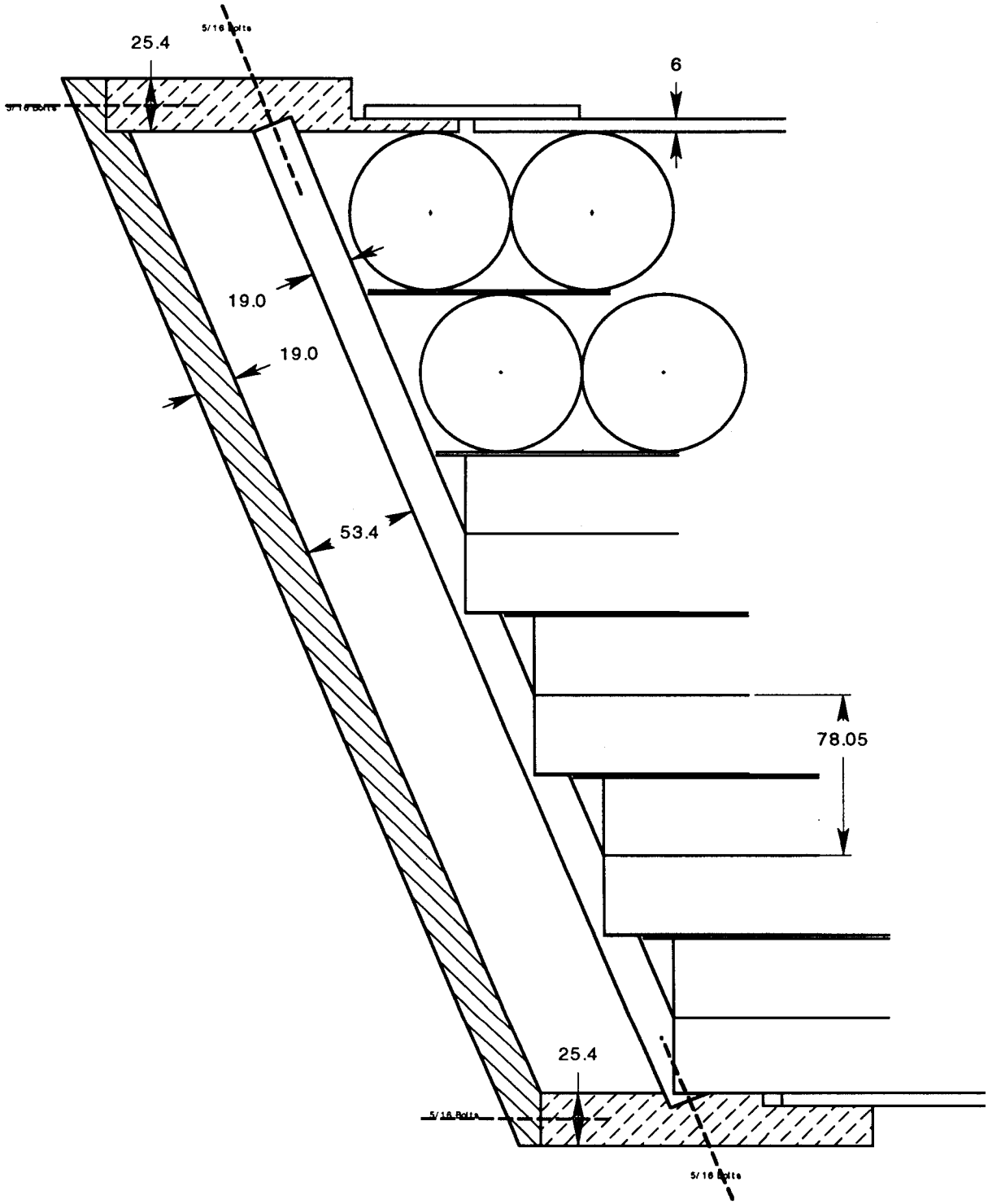

Figure 9.1. Corner cross section of prototype module section.

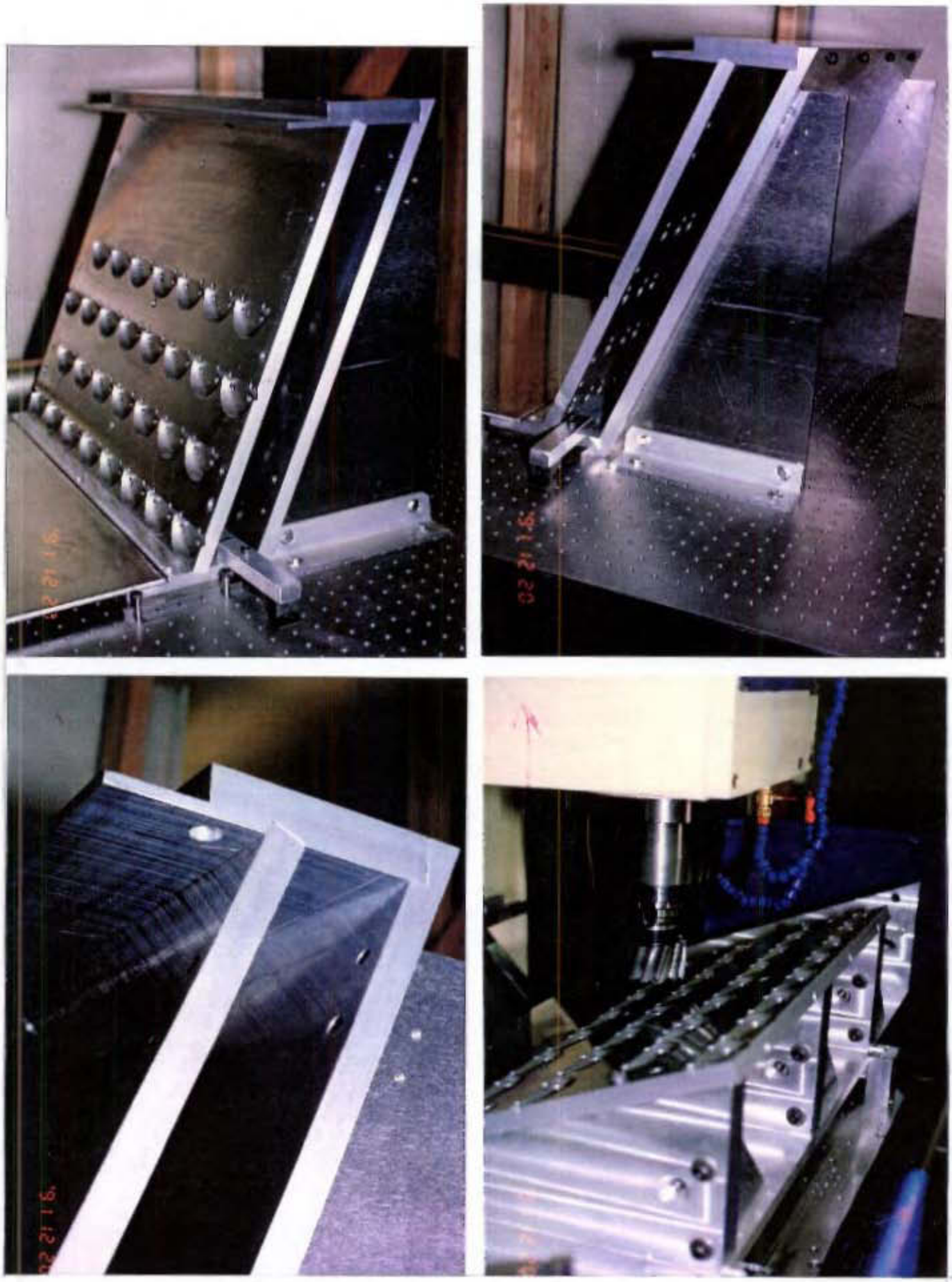

Figure 9.2. Prototype module end plate.

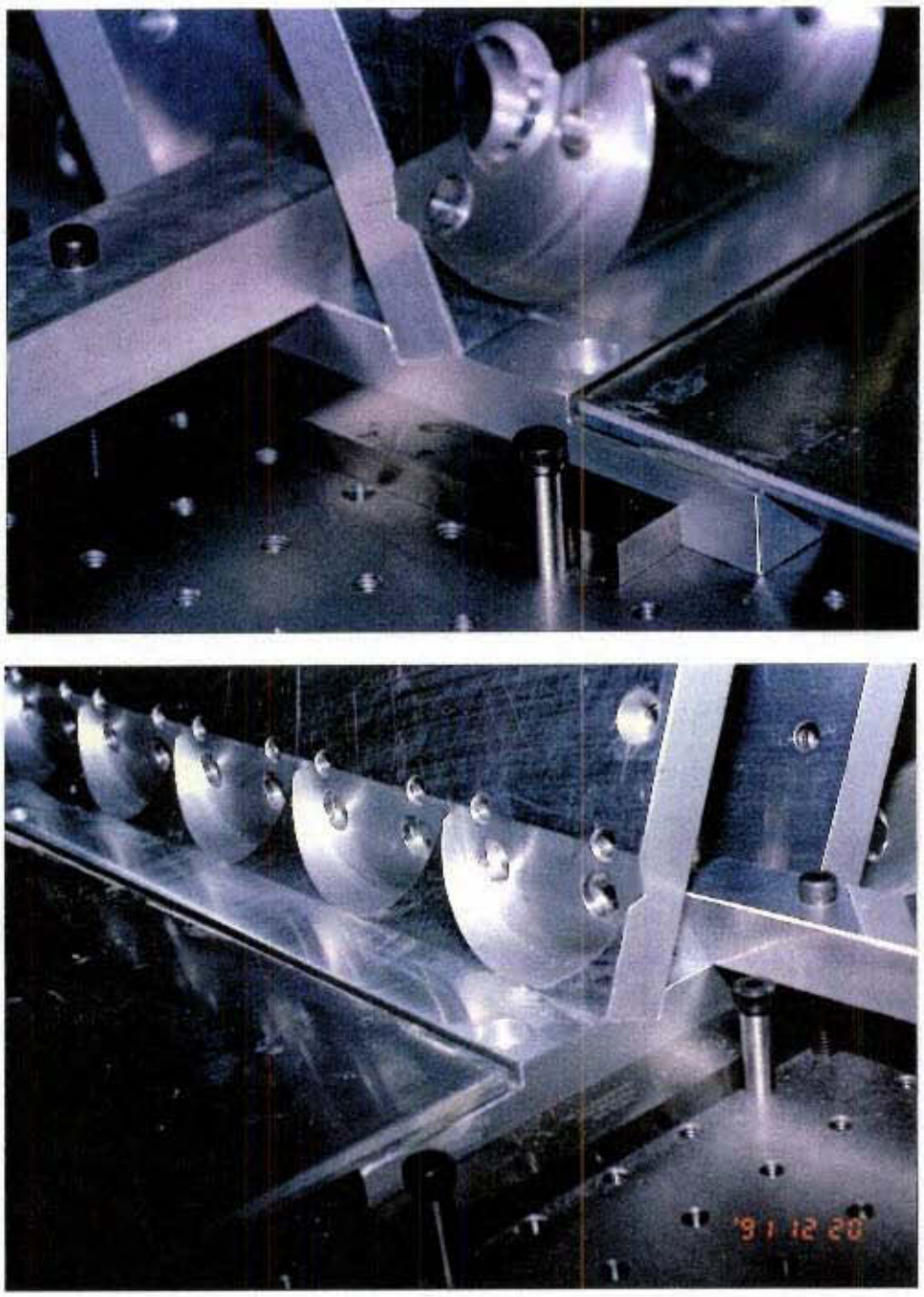

Figure 9.3. End plate details with a tube inserted.

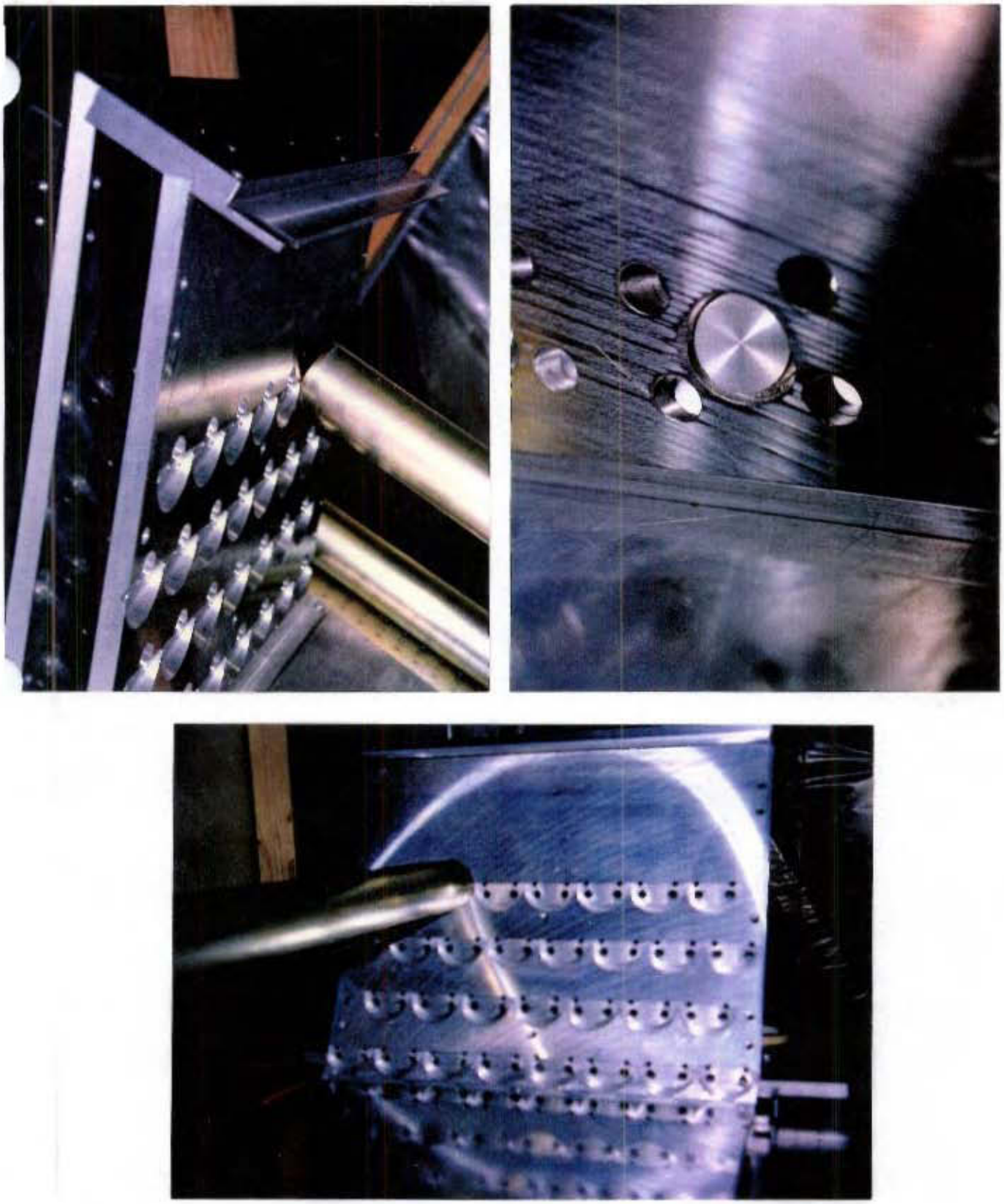

Figure 9.3. (Continued)

10.0 BEAM AND COSMIC RAY TEST

Beam tests will be conducted at Fermilab using short drift cells in the muon beam. Cosmic ray tests will be done both in Seattle and at the SSC Lab. The Washington group, SSC Lab and Texas Arlington group will participate in these tests.

10.1 Fermilab Beam Test

We plan to test the drift cells of the two options (field shaping and non field shaping) discussed in Section 4. A simple drift tube with 150 μm diameter anode and a tube with field shaping electrodes with 50 μm anode will be tested. Lengths of these tubes are approximately 0.5 meters.

In this test, we will use the T816 jet chamber system to measure the muon trajectory. T816 jet chambers have 6 sense wires per cell. The resolution per plane is expected to be <100 μm which is much smaller than the expected resolution of the drift tubes being tested. The resolution of the tubes, therefore, can be determined very precisely. Also, important parameters, such as chamber efficiency, after pulsing and double pulse resolution can be measured.

10.2 Cosmic Ray Test With Short Cells

We are also setting up a modest cosmic ray test station at the SSC Lab. The motivation for this test is to measure position resolution and efficiency for the final design. We will also conduct detailed long term measurements to study the properties of the gas mixture such as the effect of pressure, temperature, mixing ratio and pollutant dependence on the drift velocity.

10.2.1 Tube Setup

The cosmic ray test setup consists of an array of five short drift tubes (500 mm long) which are mounted onto precision machined endplates. These endplates are designed in the same manner as the final design. Three of these tubes are aligned and the other two are staggered by 2 mm. Scintillation counters are mounted on top and bottom of the chamber frame. The size of the counters is 38 mm × 400 mm × 5 mm.

A cosmic ray muon is reconstructed by using two pair of tubes, one pair on the top and another pair on the bottom. The hit position in the middle tube is thus predicted.

10.2.2 DAQ

We plan to use the SDC muon front end electronics board which will be provide by John Oliver. We will also use the D0 muon chamber front end electronics for comparison. LeCroy multihit TDC's (model 2277) will be used for readout. A CAMAC system controlled by an IBM PC will be used for DAQ.

10.3 Cosmic Ray Tests of Round Tube Design

In order to measure the position resolution and other parameters of the round tube design, we are currently assembling a cosmic ray test stand. The module structure to be tested will be assembled on a series of three optical tables in a clean room at the SSCL. The nine meter structure will then be transferred to support stands – one at each end of the structure. The test stand, being constructed jointly by personnel from U. Washington and U. Texas at Arlington, is designed to slide over the module assembly (see Figure 10.1).

The test stand will consist of the following elements:

- **Scintillation trigger and position counters.** We are obtaining the use of two box counters each containing a number of paddle and strip counters which will allow a position measurement of cosmic ray particles with an accuracy of about 1 1/2 × 3 in. This should be sufficient to determine which set of muon tubes in the test stack was hit. The scintillation counters have been checked at U.T. Arlington and are about to be shipped to the SSCL. It is foreseen that the scintillator will be used in either a simple top and bottom coincidence, or in a slightly more complex mode to select more vertical cosmic rays. The bulk of the scintillator elements will simply be latched and decoded offline to give position information.
- **Iron filter/hardener.** We shall harden the energy spectrum of cosmic muons via the use of a stack of iron blocks. Approximately 30 cm of iron will give a minimum energy of 260 MeV.
- **Muon tube array.** An array of muon counters eight tubes wide by six tubes high is being prepared for these tests. The tubes will have the maximum length of 9 meters, and will have layer offsets reflecting the overall round tube assembly design. The tube assembly will be assembled on optical tables to minimize the distortion of tube layers out of their respective planes and thus to give the assembly mechanical characteristics as close as possible to design specifications.
- **Electronics/DAQ.** A standard system of preamps, TDCs, ADCs and discriminators is being put together for the muon and scintillator systems readouts.
- **Mechanical assembly.** A stand is being designed to hold the two scintillator systems above and below the tube assembly respectively. For reasons of safety and convenience the iron block filter will probably be located in the space below the optical tables.

The measurement program during these tests will include the following items:

- pulse shape characteristics
- pulse size as a function of position along the tubes
- position resolution – using three layer trajectories to predict the location in the fourth layer
- muon tube operational stability

We are planning to complete the construction of the test set-up by early January and have results available shortly after that time.

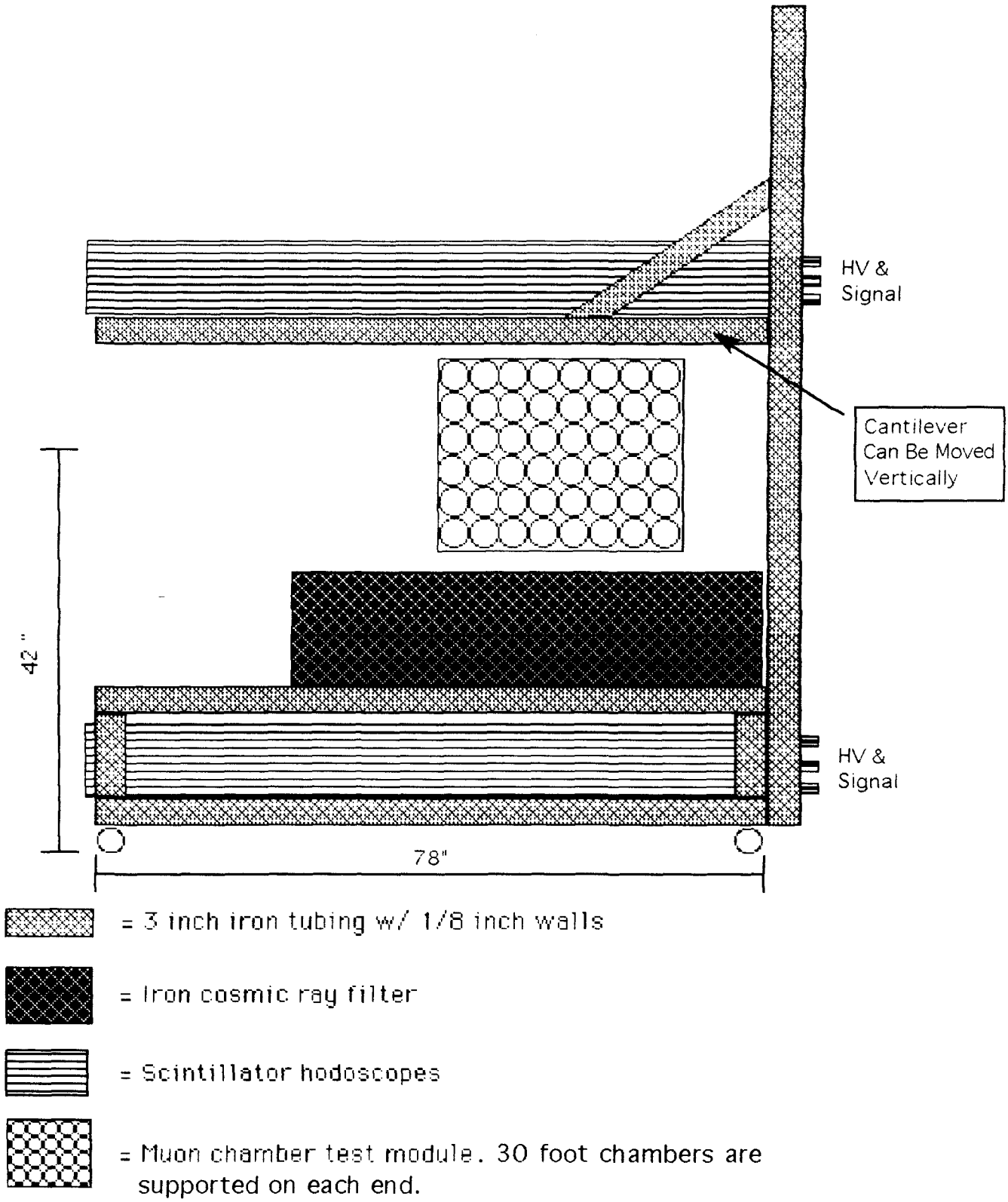

Figure 10.1. Schematic diagram of the cosmic ray test stand to be used at the SSCL, showing the details of the trigger counters, iron absorber and the position of the tubes for testing.

ACKNOWLEDGEMENTS

We want to thank the SSC Lab and the University of Washington Physics Department for their encouragement and support. The machine shops at the University of Washington and the SSCL were crucial to the fabrication of the prototype modules. We appreciate very much the assistance of Roy Cline at SSCL in procuring the necessary material and parts. The production of the document would not have been possible without the able assistance of the Technical Publications staff at the SSCL. In particular we are especially grateful to Dee Dee Kennedy, Sylvia Lee and Sue Weaver who worked long hours to produce this document. A special thanks to Tom Coyne for producing the graphics and Don Johnson and crew for speedy printing.